The Pennsylvania State University

The Graduate School

College of Engineering

FRACTURE PROPERTIES OF FIBER REINFORCED CONCRETE

A Thesis in

Civil Engineering

by

Krishna Chaitanya Amirineni

Submitted in Partial Fulfillment
of the Requirements
for the Degree of

Master of Science

May 2009

The thesis of Krishna Chaitanya Amirineni was reviewed and approved* by the following:

Maria Lopez de Murphy
Will Assistant Professor of Civil Engineering
Thesis Advisor

Andrew Scanlon
Professor of Civil Engineering

Charles Bakis
Distinguished Professor of Engineering Science and Mechanics

Peggy Johnson
Professor of Civil Engineering
Head of the Department of Civil and Environmental Engineering

*Signatures are on file in the Graduate School

Abstract

Fracture properties of four different steel fiber reinforced concrete (SFRC) mixtures are determined in the present study. Two types of hooked end steel fibers having aspect ratios of 80 and 65 respectively were used employing volume fractions of 0.5% and 1.0%. Three point bending tests have been performed conforming to RILEM technical committee TC 162-TDF (RILEM, 2002a). The equivalent, f_{eq}, and residual, f_R, flexural tensile strength parameters, proposed by RILEM TC 162-TDF (RILEM, 2002a), to characterize and simulate the post-cracking behavior of SFRC have been evaluated and compared for the various concrete mixtures. It is observed that the equivalent flexural tensile strengths, f_{eq}, have less variance compared to the residual flexural tensile strengths, f_R.

A step wise optimization algorithm was developed to obtain the stress-crack opening (σ-w) curve of fiber reinforced concrete (FRC) using inverse analysis procedures. The optimization algorithm was developed as a three step process calculating the modulus of elasticity, E, in Step 1 and the tensile strength, f_t, and the slope of the first leg of the bilinear σ-w curve, a_1, in Step 2. Finally the parameters defining the second leg of the bilinear σ-w curve, a_2 and b_2 are calculated in the third and the final step. It was observed that f_t and a_1 can be accurately predicted by restricting the optimization interval in Step 2 to [0, 0.05 mm]. It is concluded that the load- crack mouth opening displacement (P-CMOD) data from three point bending tests should be recorded at least until a CMOD of 5.0 mm is reached. The stress-crack opening curve of FRC can be predicted accurately by following the three step procedure, restricting the end level of CMOD to 0.05 mm in Step II and by performing the optimization in Step 3 at least until an end CMOD of 5.0 mm

Table of Contents

List of Figures v

List of Tables vii

List of Notations ix

Acknowledgements xii

CHAPTER 1 Introduction 1

1.1 Objective and Research Significance 2
1.2 Research Tasks 2
1.3 Layout of the Thesis 3

CHAPTER 2 Literature Review 6

2.1 Background 6
2.2 Fracture Mechanics of Fiber Reinforced Concrete 10
2.3 Stress-Crack opening (σ-w) Curve 10
2.4 Calculation of Residual Strengths per ASTM C 1609 17
2.5 Cracked Hinge Model 19
2.6 Inverse Analysis 26

CHAPTER 3 Experimental Program 36

3.1 Materials 36
3.2 Test Specimens and Test Matrix 36
3.3 Test Setup and Procedure 37
3.4 Analysis of Test Data 43

CHAPTER 4 Inverse Analysis 53

4.1 Introduction 53
4.2 Algorithm for Inverse Analysis 54

CHAPTER 5 Conclusions and Recommendations 77

References 80

Appendix A Experimental Data 85

Appendix B Proposed Matlab Algorithm 91

List of Figures

Figure 2.1: Dugdale's plastic zone model. 6

Figure 2.2: Stress-deformation behavior of a quasi-brittle specimen in tension. 7

Figure 2.3: Definition of cohesive crack model. 9

Figure 2.4: Test specimen under three point load and assumed stress distribution. 12

Figure 2.5: Determination of F_L and equivalent flexural tensile strength. 14

Figure 2.6: Calculation of equivalent flexural strengths. 15

Figure 2.7: Calculation of residual flexural strengths. 16

Figure 2.8: Parameter calculations for first-peak load equal to peak load. 18

Figure 2.9: Parameter calculations for first peak load less than peak load. 18

Figure 2.10: Geometry of test specimen and cracked hinge. 19

Figure 2.11: Material model for precracked and cracked state of concrete. 20

Figure 2.12: Geometry, loading and deformation of cracked hinge. 21

Figure 2.13: Four phases of stress distribution in elastic layer of hinge. 22

Figure 2.14: Geometry of three point bending test specimen 24

Figure 2.15: Softening models and corresponding parameters. 31

Figure 2-16: Effect of weighing function on the P-CMOD curve for SFRC. Inverse analysis was performed in the interval [0.0; 2.0 mm]. 33

Figure 2-17: Effect of weighing function on the σ-*w* curve for SFRC. Inverse analysis was performed in the interval [0.0; 2.0mm]. 34

Figure 2.18: Relationship between $f_{eq,2}$ and $f_{eq,3}$. 35

Figure 2.19: Relationship between $f_{R,1}$ and $f_{R,4}$. 35

Figure 3.1: Geometry of 3PB test specimen. 37

Figure 3.2: Test setup for split cylinder test. 38

Figure 3.3: Test setup for compressive strength test. 39

Figure 3.4: Test setup for three point bending tests. 42

Figure 3.5: Plot showing typical experimental load-deflection curves. 44

Figure 3.6: Plot showing typical experimental load-CMOD curves. 44

Figure 3.7: Peak loads for three point bending tests. 45

Figure 3.8: Trend showing effect of fiber type and volume fraction of fibers on limit of proportionality. 46

Figure 3.9: Trend showing effect of fiber type and volume fraction of fibers on equivalent flexural tensile strength, $f_{eq,2}$. 47

Figure 3.10: Trend showing effect of fibers type and volume fraction of fibers on residual flexural tensile strength, $f_{eq,3}$. 47

Figure 3.11: Plot showing the relationship between $f_{eq,3}$ and $f_{eq,2}$. 48

Figure 3.12: Plot showing the relationship between $f_{R,4}$ and $f_{R,1}$. 49

Figure 3.13: σ-ε diagram for SFRC, according to RILEM TC 162-TDF. 50

Figure 3.14: Residual strengths calculated according to ASTM C1609. 52

Figure 4.1: Typical load-CMOD curve showing the phases of crack propagation and the corresponding stress distribution. 56

Figure 4.2: Flowchart of the proposed optimization algorithm. 57

Figure 4.3: Comparison of experimental and analytically predicted *P*-CMOD curves for elastic modulus. 58

Figure 4.4: Variation of normalized moment, μ, as a function of normalized curvature, θ, for varying E and constant f_t and a_1 60

Figure 4.5: Variation of normalized moment, μ, as a function of normalized curvature, θ, for varying f_t and constant E and a_1 60

Figure 4.6: Variation of normalized moment, μ, as a function of normalized curvature, θ, for varying a_1 and constant f_t and E 61

Figure 4.7: Typical experimental load-CMOD curves. 61

Figure 4.8: Plot showing the initial portion of the *P*-CMOD curves for some of the tested specimens. 62

Figure 4.9: Plot showing experimental and predicted P-CMOD curves for concrete mixture 65/35-0.5% for a CMOD range of [0, 0.05 mm] 64

Figure 4.10: Plot showing experimental and predicted P-CMOD curves for concrete mixture 65/35-1.0% for a CMOD range of [0, 0.05 mm]. 64

Figure 4.11: Plot showing experimental and predicted P-CMOD curves for concrete mixture 80/60-0.5% for a CMOD range of [0, 0.05 mm]. 65

Figure 4.12: Plot showing experimental and predicted P-CMOD curves for concrete mixture 80/60-1.0% for a CMOD range of [0, 0.05 mm]. 65
Figure 4.13: Effect of end level of CMOD on a_2 and b_2. 68
Figure 4.14: σ-w curves for concrete mixtures with 0.5% volume fraction of fibers..... 71
Figure 4.15: σ-w curves for concrete mixtures with 1.0% volume fraction of fibers..... 72
Figure 4.16: Plots showing the σ-w curves for a crack hinge opening, w, range of [0, 0.02mm]. 72
Figure 4.17: Plot showing experimental and predicted P-CMOD curves for concrete mixture 65/35-0.5% in a CMOD range of [0, 6.0 mm] 74
Figure 4.18: Plot showing experimental and predicted P-CMOD curves for concrete mixture 65/35-1.0% in a CMOD range of [0, 6.0 mm]. 75
Figure 4.19: Plot showing experimental and predicted P-CMOD curves for concrete mixture 80/60-0.5% in a CMOD range of [0, 6.0 mm]. 75
Figure 4.20: Plot showing experimental and predicted P-CMOD curves for concrete mixture 80/60-1.0% in a CMOD range of [0, 6.0 mm]. 76
Figure A.1: Plot showing the P-δ curves for 65/35-0.5%. 85
Figure A.2: Plot showing the P-δ curves for 65/35-1.0% 85
Figure A.3: Plot showing the P-δ curves for 80/60-0.5% 86
Figure A.4: Plot showing the P-δ curves for 80/60-1.0% 86
Figure A.5: Plot showing the P-CMOD curves for 65/35-0.5% 87
Figure A.6: Plot showing the P-CMOD curves for 65/35-1.0% 87
Figure A.7: Plot showing the P-CMOD curves for 80/60-0.5% 88
Figure A.8: Plot showing the P-CMOD curves for 80/60-1.0% 88
Figure A.9: Plot showing the CMOD-δ curves for 65/35-0.5%..... 89
Figure A.10: Plot showing the CMOD-δ curves for 65/35-1.0%..... 89
Figure A.11: Plot showing the CMOD-δ curves for 80/60-0.5%..... 90
Figure A.12: Plot showing the CMOD-δ curves for 80/60-1.0%..... 90

List of Tables

Table 3.1: Concrete mixture proportions. 36
Table 3.2: Properties of steel fibers. 36
Table 3.3: Test matrix. 37
Table 3.4: Compressive strength and split tensile strengths of all tested specimens. 40
Table 3.5: Test results of all specimens tested. 46
Table 3.6: First-peak and residual strengths per ASTM C1609. 52
Table 4.1: Parameters defining σ-w curve. 68
Table.4.2: Comparison of experimental and predicted material properties 70

List of Notations

σ	stress at any point in a material, N/mm^2
$\sigma_w(w)$	stress along a crack as a function of crack width, w, N/mm^2
ε	strain in the specimen
w	crack opening, mm
w_c	critical crack depth, mm
δ	deflection at the center of the beam, mm
δ_L, δ_u	deflection at limit of proportionality, mm
δ_2, δ_3	deflection at the center of the beam corresponding to serviceablitiy limit and ultimate limit state, mm
φ	angular deformation
β_1, β_2	normalized slopes corresponding to a_1 and a_2
μ	normalized moment
θ	normalized curvature
α	normalized crack depth
a_0	notch depth, mm
a_1, a_2	slope of the first and second legs of the bilinear stress-crack opening curve
b	width of the specimen, mm
b_1, b_2	ordinates on the normalized stress-crack opening curve
d_1	depth of knife edges, mm
d_f	diameter of the fiber, mm
f'_c	compressive strength of concrete, MPa
f_{st}	splitting tensile strength, MPa
f_1	first-peak strength, MPa
$f_{fct,L}$	limit of proportionality, N/mm^2

$f_{eq,i}$	equivalent flexural tensile strength, N/mm^2
$f_{R,i}$	residual flexural tensile strength, N/mm^2
f_{150}, f_{600}	residual stresses corresponding to P_{150} and P_{600} respectively, MPa
f_t	tensile strength of concrete, N/mm^2
$g(w)$	normalized stress-crack opening curve
h_{sp}, h	unnotced depth of the specimen, mm
s	hinge width, mm
l_f, l	length of the fiber, mm
n	number of variables in an optimization problem
$CMOD_i$	CMOD at different points on load-CMOD curve, mm
$CMOD_{exp}$, $CMOD_{pre}$	experimental and predicted CMOD, mm
$D_{BZ,i}$	energy absorption capacity corresponding to δ_2 and δ_3
$F_{L,}$ F_u	load at limit of proportionality, N
F_i	mean forces corresponding to δ_2 and δ_3, kN
$F_{R,I}$	load corresponding to $CMOD_i$, kN
G_F	fracture energy
P	load acting on the specimen in a three point bending test, kN
$P_{150,}$ P_{600}	loads corresponding to a midspan deflection of L/150 and L/600 respectively, kN
D	diameter of the cylinder specimen, mm
L	span of the specimen, mm
H, d	total depth of the specimen, mm
$P_{exp,}$	load obtained experimentally in the P-CMOD curve, kN
P_{pre}, P_{calc}	load predicted analytically, kN
N^0_{max}	last number of observation made in Phase 0 P-CMOD curve
N_{max}	maximum number of observations made in P-CMOD curve

V_F	volume fraction of fibers

Acknowledgements

First and foremost, I would like to thank Dr. Maria Lopez for her guidance and support throughout my thesis research and graduate career. I would also like to thank Dr. Scanlon and Dr. Bakis for serving as members on my thesis committee and providing assistance with my thesis. I would like to acknowledge all those who assisted me in the preparation and testing of specimens during my thesis research, notably Jae Ha Lee, Rosemary Chako, Travis Hockenberry, Sameer Damle, Anusha Gullapalli and Dan Fura.

At a personal level, I want to thank my parents without whose help and constant support I would not have had an opportunity to pursue master's studies in the United States. My sister Neelima was also very supportive. Ramya Subramanian helped me throughout my master's study and gave me excellent suggestions and personal support.

Chapter 1 Introduction

Concrete, as a result of its many desirable properties, can be used in a variety of innovative designs. It not only possesses high compressive strength, stiffness, low thermal and electrical conductivity and low combustibility and toxicity, but it can also be cast in diverse shapes. But two material characteristics, which limit the use of concrete are brittleness and low strength in tension. However, the addition of fibers, to the otherwise brittle matrix, creates resistance to crack formation and progression, which increases the ductility of the materials structural response (Lim and Oh, 1999). Fibers have been used widely in non structural applications, like slabs on grade, industrial floors, pavements and overlays. (Meda et al, 2005 and ACI Committee 544, 2002). Fiber reinforced concrete has recently been added to the ACI 318 code as a viable alternative of minimum shear reinforcement for beam elements (ACI 318, 2008).

The concrete property most influenced by the addition of fibers to concrete is the capacity of energy absorption. Due to the relevance of the energy absorption capacity of fiber reinforced concrete (FRC), several entities have been proposed for evaluating this property, namely, toughness indices, equivalent flexural strength, and fracture energy. Fracture energy is the most widely used property in constitutive models for characterizing the fracture toughness and the post crack tensile capacity of concrete. In the case of FRC, the concept of critical crack width, w_c, is not relevant and therefore, fracture energy, G_F, loses its significance. So the stress-crack opening (σ-w) curve which influences the structural behavior becomes more important compared to fracture energy. (RILEM, 2002b)

The structural behavior of concrete during cracking can be described by nonlinear fracture mechanics models such as the fictitious crack model (FCM) proposed by Hillerborg et al. (1976). The application of Hillerborg's approach requires the knowledge of the characteristic σ-w curve of the concrete. Under ideal conditions, this relation should be obtained from uniaxial tension tests of the concrete. Such tests are "expensive and time consuming and the problem of strain gradients in the ligament due to non-uniform cracking causes additional problems. Therefore, uniaxial tension tests are not an appropriate method for practical materials testing" (Slowik 2006). A practical alternative is the use of the experimentally obtained response of a notched beam to determine the σ-w curve of the corresponding material through inverse analysis.

1.1 Objective and Research Significance

The objective of this research is to develop a methodology to accurately model the stress-crack opening (σ-w) behavior of steel fiber reinforced concrete (SFRC) from the load-crack mouth opening displacement (P-CMOD) response of the material. Many techniques have already been proposed to model the stress-crack opening behavior of concrete (Roelfstra and Wittman (1986), Kitsutaka (1997), Ostergaard (2003) and Sousa and Gettu (2006)). These existing techniques either require an initial approximation of the results, which are very close to the actual results (Roelfstra and Wittman, 1986), or in some cases require the optimization to be run several times to achieve convergence in the results (Ostergaard, 2003). In some cases, they can only predict one portion of the curve accurately (Sousa and Gettu, 2006).

In this study, an optimization algorithm was developed to accurately model the entire softening behavior which can overcome the above mentioned drawbacks of the existing algorithms. A bilinear σ-w curve is used in the current algorithm, since for many SFRC materials it has been proven that a bilinear relationship provides a reasonable representation of the measured behavior (RILEM, 2002b)

1.2 Research Tasks

In order to achieve this objective the following research program was concluded:

1. Fabrication and testing of beam specimens under three point loading conforming to the RILEM TC 162-TDF (RILEM, 2002a).
2. Recording displacement, load data and the crack mouth displacement (CMOD) for obtaining the σ-w response of the beams.
3. Performing splitting-tensile strength and compressive strength tests on cylindrical specimens of concrete.
4. Analysis and compilation of the load-deflection (P-δ) and load-crack mouth opening displacement (P-CMOD) data for the beams to evaluate the tensile behavior of the FRC in terms of: limit of proportionality ($f_{fct,L}$), equivalent flexural strengths ($f_{eq,i}$) and residual flexural strengths ($f_{R,i}$).
5. Development of an optimization algorithm to back calculate the stress-crack (σ-w) relationship from the load-crack mouth opening displacement (P-CMOD) response of the beams using inverse analysis.
6. Incorporation of the algorithm into a commercial software (Mathematica, Matlab) capable of performing optimizations and calculations.
7. Obtain the σ-w response from the inverse analysis.

1.3 Layout of the Thesis

The thesis is structured around four main chapters. Chapter 2 gives an overview of the cohesive crack model and fracture mechanics of fiber reinforced concrete (FRC) and the importance of the σ-w curve in characterizing the fracture properties of FRC. The direct (uniaxial tension test) and the indirect (using P-CMOD curves and inverse analysis) methods of obtaining the σ-w curves are then explained in detail. Properties like limit of proportionality, $f_{fct,L,}$ equivalent flexural strengths, $f_{eq,i,}$ and residual flexural strengths, $f_{R,i,}$ which are used to characterize the energy absorption capacity of FRC, and the experimental procedure to obtain them are also explained. The cracked hinge model, which forms the basis for obtaining the σ-w curve using inverse analysis, is also explained in detail and a brief overview of the process of inverse analysis is presented. Finally, an outline of the previous research results pertaining to the calculation of σ-w curves and the parameters used to characterize the energy absorption capacity of FRC is also presented.

The experimental program is explained in Chapter 3. The concrete mixture design and the specimen type used for different finding different properties are also outlined in this chapter. The experimental setup and the data collection process is also presented in detail. Chapter 3 also discusses the analysis of the test data obtained from the three point bending tests (3PB test) and the splitting tensile and compressive strength tests.

Chapter 4 explains the proposed algorithm to perform the inverse analysis process. It explains in detail various steps in the optimization algorithm and also explains the theoretical reason for each step performed. A comparison is made with the

existing methods and an outline of the advantages of the proposed algorithm over the existing methods is also presented. A detailed analysis of the σ-w curves obtained is presented and guidelines are proposed for obtaining the P-CMOD curves from 3PB tests and for performing the inverse analysis.

Finally, Chapter 5 presents general and specific conclusions. This is followed by an extensive list of references. Appendix A and B give the results of the tests outlined in Chapter 3 and the Matlab code used for the inverse analysis in Chapter 4, respectively.

Chapter 2 Literature Review

2.1 Background

The concept of using a cohesive zone to model stress behavior near the crack tip was pioneered by Dugdale (1960) and Barenblatt (1962). Dugdale's model assumes that a stress, equal to the yield stress of the material, acts uniformly across the cohesive zone, as seen in Figure 2.1. Barenblatt (1962) assumes a varying stress across the cohesive zone as a function of the cohesive crack width, as opposed to the constant stress in case of Dugdale's model.

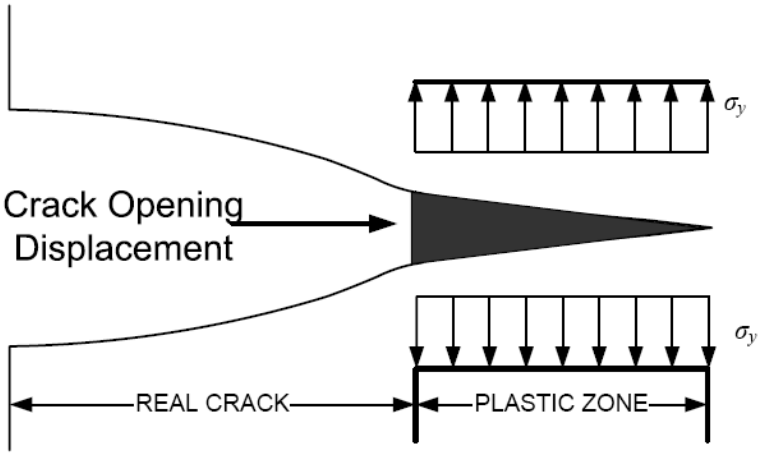

Figure 2.1: Dugdale's plastic zone model.

Scanlon and Murray (1979) introduced the concept of tensile stress softening to model the contribution of concrete to the stiffness of cracked reinforced concrete zones for use in "smeared" cracking in finite element models. Hillerborg and his co-workers were the first to explore the idea of application of cohesive zones to study the fracture and crack propagation in concrete and proposed the "fictitious" crack model (Hillerborg et al., 1976; Petersson, 1981). Due to the close similarity with the cohesive crack model proposed by Barenblatt (1962), many researchers use the former terminology of "cohesive crack model". The cohesive crack model

can capture the behavior of a structure from crack initiation to failure, unlike LEFM models which can be applied only to initially cracked structures.

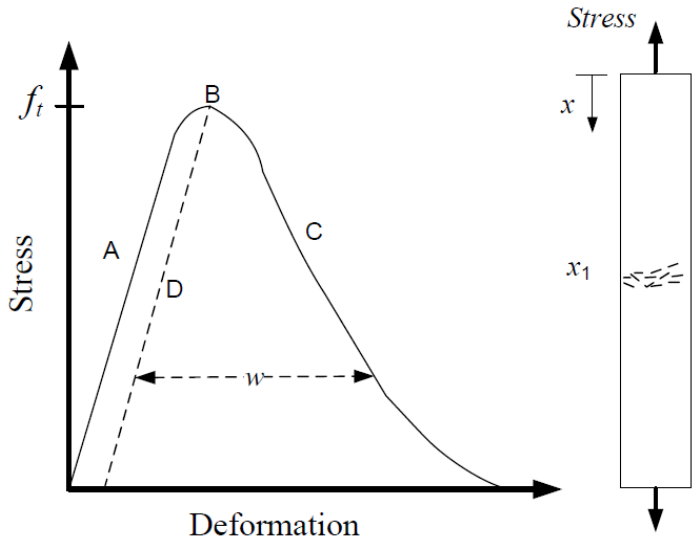

Figure 2.2: Stress-deformation behavior of a quasi-brittle specimen in tension

The idea of the cohesive crack model is best explained by the study of the stress-deformation diagram obtained from a simple tension test, see Figure 2.2. The two curves ABD and ABC represent stress-deformation behavior at two different locations of the test specimen. ABC describes the behavior at location x_1 where a localized fracture zone develops. On the other hand, ABD is a representative behavior of the material at a location outside the fracture process zone. Prior to the attainment of the tensile strength, f_t, the whole specimen is subjected to the same stress and deformation. Therefore a stress-strain (σ-ε) law can be used to describe the material behavior at this stage. After the tensile strength is reached a fracture zone starts forming at some discrete position (at x_1) on the test specimen. With a further increase in the deformation, there would be a decrease in the stress due to formation of microcracks in the fracture zone. As the stress decreases all parts outside the fracture zone acquire a decreasing elongation, corresponding to the

unloading curve of the stress-strain diagram. As a result we obtain an increase in deformation within the fracture zone and a decrease in deformation outside the fracture zone at the same time as the stress decreases. The complete relation between stress and deformation can be described by means of two curves, viz the stress–strain (σ-ε) curve and the stress–crack opening (σ-w) curve. The σ-ε curve is valid for the entire length of the specimen, outside the fracture zone. The σ-w curve is valid for the fracture zone only, and it shows the displacement that has to be added to the deformation according to the σ-ε curve in order to obtain the total deformation.

The σ-w curve can be determined from a tension test if the conditions are stable during the whole test and if the unloading branch from the maximum stress in the stress-deformation curve is known, see Figure 2.2. The original length of the fracture zone is assumed to be zero and the fracture zone is considered to open up as a crack which opens up to width of w, although it still takes stress according to the σ-w curve. This is the fictitious crack model, FCM. In this model it is assumed that stresses within the fictitious crack are related to the displacement, w, but that the stresses outside the fictitious crack are related to the strain ε. At the fictitious crack tip, the stress is assumed to be equal to the tensile strength, f_t. The distribution of tensile stress varies nonlinearly along the length of the fracture process zone, as seen in Figure 2.3.

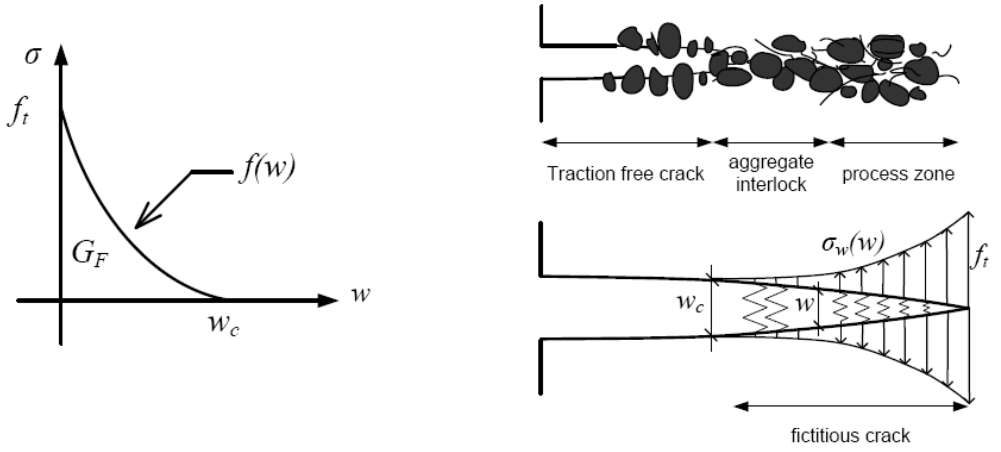

Figure 2.3: Definition of cohesive crack model.

The length of the fictitious crack increases as the stresses in front of the crack tip increases. At the same time the displacement, w, at the tip of the real crack increases and when a critical crack width, w_c, is reached the real crack starts propagating. The stresses in the fracture zone can be analytically expressed as a function of the crack width by using a softening law, as shown in Figure 2.3. An important property of the softening law is the fracture energy, G_F, which is a measure of the energy absorbed to create and fully separate a unit surface area of cohesive crack. It can be evaluated as the area under the softening curve, shown in Figure 2.3, and given by the expression:

$$G_F = \int_0^{w_c} f(w).dw \qquad \text{Eq. 2.1}$$

As the main advantage of fiber reinforced concrete compared to plain concrete lies with the fracture properties, it is essential to be able to make a theoretical analysis of the fracture of fiber concrete.

2.2 Fracture Mechanics of Fiber Reinforced Concrete

Hillerborg (1980) introduced the cohesive crack approach for fiber reinforced concrete, where the softening curve or the stress-cracking relationship describes the stresses carried by fibers across a fictitious crack as a function of the crack width. The fictitious crack in fiber reinforced concrete (FRC) materials represents the process zone, aggregate interlock as well as fiber bridging. The fictitious crack approach for crack initiation, propagation and opening in FRC differs significantly from the fictitious approach to concrete fracture. The fiber bridging in case of FRC is closely related to the fibers debonding and pulling out, and since the length of fibers generally used is large compared to crack openings accepted in real structures the critical crack width, w_c is not relevant and the fracture energy, G_F, as shown in Figure 2.3, loses its significance (Stang, 2002). Further, the stress-crack opening curve shape depends on the type and amount of fiber used and the shape of the curve influences the structural behavior. Thus the actual variation of the stress function with a changing crack opening (σ-w) curve is more important than G_F.

2.3 Stress-Crack opening (σ–w) Curve

The most direct way to obtain the softening curve is by means of a stable uniaxial tensile test (Petersson, 1981). However, experimental results have shown that such an approach is extremely difficult because of some major drawbacks (Bui, 2007), specifically:

a. The location of the cohesive crack is not known a priori, and in most occasions multiple cracking occurs due to the material heterogeneity (Guo and Zhang, 1987: Philips and Binsheng, 1993; Planas and Elices, 1986).

b. For materials where the process zone is very small, uncracked specimens undergo large amounts of yielding before the cohesive crack forms, which increases the specimen compliance and instability. The strain energy stored in the specimen makes the test unstable even under crack opening displacement control (Gomez et al., 2000).

c. When a small crack is introduced to initiate fracture and a single cohesive crack is produced, the specimen tends to asymmetric modes of fracture, and the crack opening is not uniform across the specimen. Stiffer testing machines do not solve the problem due to the elastic internal rotations in the specimen itself. Moreover, when the rotations are avoided using very short specimens and a very stiff machine, or by means of special servo-controlled systems, the two cracks formed on each side of the specimen tend to move away from each other when they approach, and hence never constitute a true single crack (Carpinteri and Ferro, 1994: van Mier and Vervuurt, 1995).

2.3.1 Parameters Needed to Determine the σ–w Curve:

To evaluate the tensile behavior of fiber reinforced concrete, RILEM TC 162-TDF (RILEM, 2002a) proposes the calculation of three parameters: the limit of proportionality ($f_{fct,L}$), the equivalent flexural tensile strengths ($f_{eq,2}$ *and* $f_{eq,3}$) and the residual flexural tensile strengths ($f_{R,1}$ *and* $f_{R,2}$). RILEM TC 162-TDF (RILEM, 2002a) adopted these parameters from *Deutschen Beton Vereins,* DBV (1995). A brief overview of the importance and the calculation of the above mentioned parameters is presented here.

Limit of Proportionality

The load at the limit of proportionality, F_L or $F_{u,}$ is defined as the highest value of load in the interval, δ or CMOD, of 0.05 mm. Once the value of F_L is known, the moment at the mid span of the test beam can be calculated as:

$$M_L = \frac{F_L}{2} \cdot \frac{L}{2} \qquad \text{Eq. 2.2}$$

where L is the span of the specimen (mm).

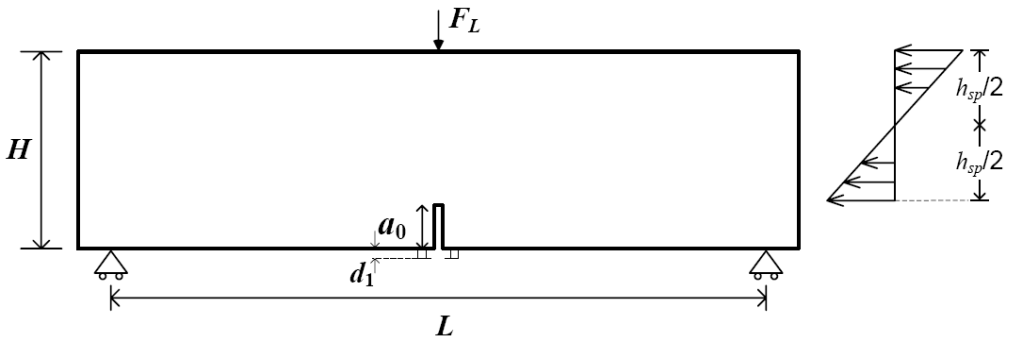

Figure 2.4: Test Specimen under three point load and assumed stress distribution.

Assuming a linear stress distribution over the cross section of the specimen, as shown in Figure 2.4, the limit of proportionality $f_{fct,L}$ can be calculated using the following expression:

$$f_{fct,L} = \frac{3F_L L}{2bh_{sp}^2} \text{ (N/mm}^2\text{)} \qquad \text{Eq. 2.3}$$

where: b = width of the specimen

h_{sp} = distance between the tip of the notch and the top of the cross section (mm).

Equivalent Flexural Strengths ($f_{eq,2}$ and $f_{eq,3}$)

A brief overview of the parameters as proposed by DBV (1995), which is explained by Tlemat et al., (2006), is presented here. The energy absorption

capacities $D_{BZ,2}$ and $D_{BZ,3}$ are equal to the areas ABCD and ABEF under the load deflection curve up to deflections δ_2 and δ_3, respectively, as shown in Figure 2.5. RILEM TC 162-TDF (RILEM, 2002a) suggests a span length of L = 500 mm, and therefore the deflections translate to

$$\delta_2 = \delta_u + \frac{L}{4000} + \frac{L}{1200} = \delta_u + 0.54 \text{ mm.} \quad \text{Eq. 2.4}$$

$$\delta_3 = \delta_u + \frac{L}{4000} + \frac{L}{200} = \delta_u + 2.625 \text{ mm.} \quad \text{Eq. 2.5}$$

Similarly the mean forces F_2 and F_3, which are defined as the ratio of the energy absorption capacities and the mean deflection, can be expressed as:

$$F_2 = \frac{D_{BZ,2}}{L/1200} = \frac{D_{BZ,2}}{0.42} \text{ (N)} \quad \text{Eq. 2.6}$$

$$F_3 = \frac{D_{BZ,3}}{L/200} = \frac{D_{BZ,3}}{2.5} \text{ (N)} \quad \text{Eq. 2.7}$$

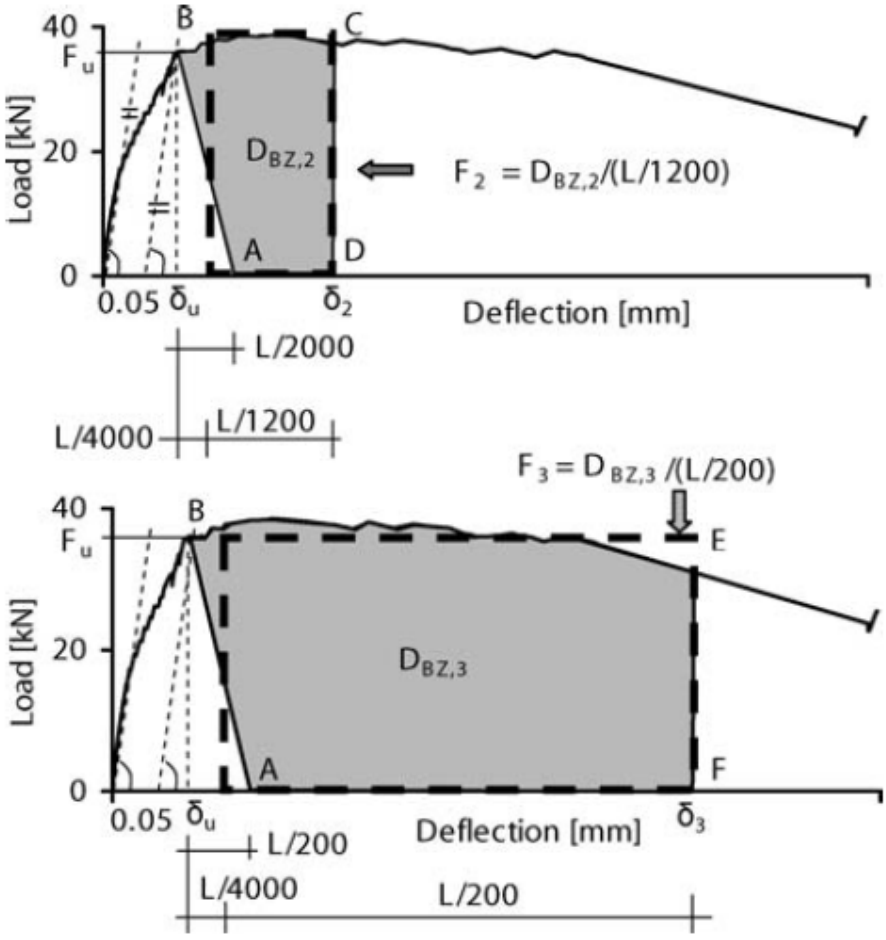

Figure 2.5: Determination of F_L and equivalent flexural tensile strength. (Tlemat et al., 2006).

RILEM (2002a), which is adopted in the existing work, uses a slightly different approach in calculating these parameters. Figure 2.6 shows the definitions of the load at limit of proportionality F_L, and energy absorption capacities $D_{BZ,2}$ and $D_{BZ,3}$.

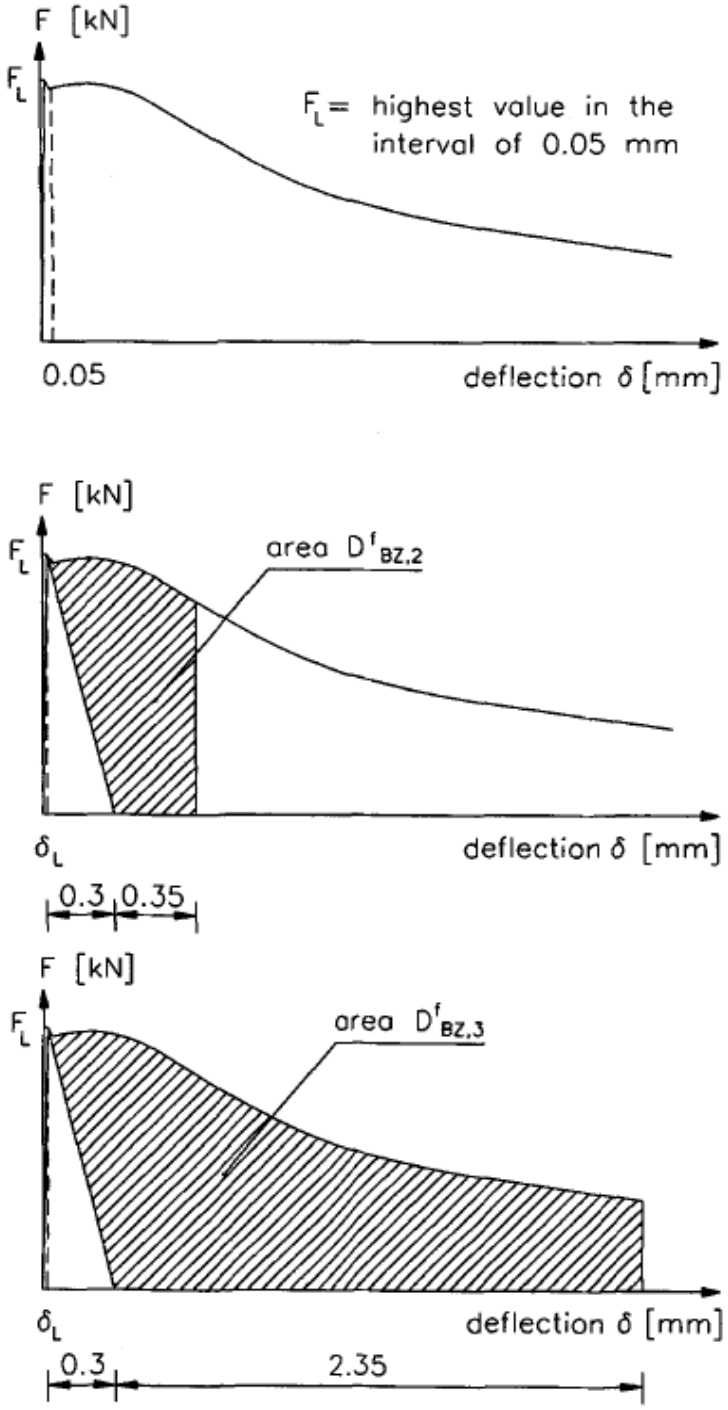

Figure 2.6: Calculation of equivalent flexural strengths. (RILEM, 2002a)

With the energy absorption capacities as defined in Figure 2.6, the mean deflections δ_2 and δ_3 can then be defined as given in Eq 2.8.

$$\delta_2 = \delta_L + 0.65\,\text{mm} \quad (\text{mm})$$
$$\delta_3 = \delta_L + 2.65\,\text{mm} \quad (\text{mm})$$

Eq. 2.8

The mean forces F_2 and F_3 are defined as the ratio of the energy absorption capacities and the mean deflections. The equivalent flexural tensile strengths, $f_{eq,2}$ and $f_{eq,3}$ can then be calculated as given in Eq. 2.4.

$$f_{eq,2} = \frac{3F_2 L}{2bh_{sp}^2}$$
$$f_{eq,3} = \frac{3F_3 L}{2bh_{sp}^2}$$

Eq. 2.9

Residual Flexural Strengths ($f_{R,1} - f_{R,4}$)

In addition to the equivalent flexural tensile strengths, residual flexural tensile strengths $f_{R,i}$ are defined using the Load-CMOD curve at crack mouth opening displacement, CMOD equal to 0.5 mm, 1.5 mm, 2.5 mm and 3.5 mm, as shown in Figure 2.10.

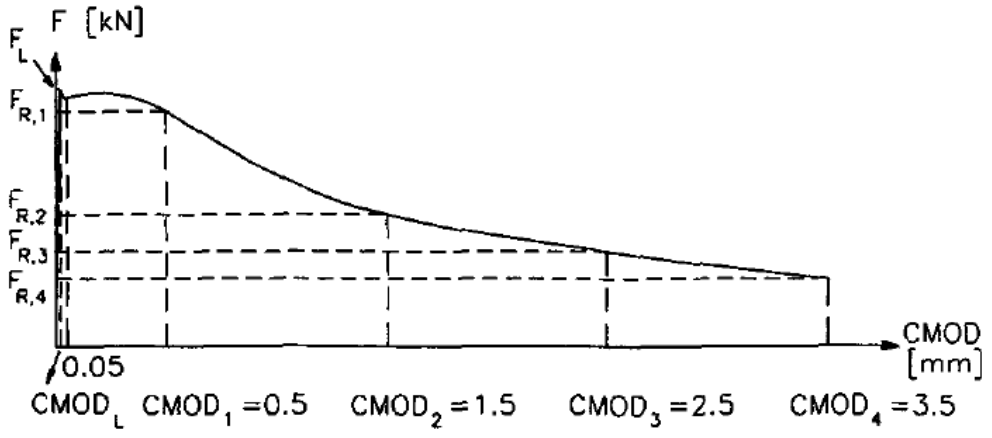

Figure 2.7: Calculation of residual flexural tensile strengths. (RILEM, 2002a)

The residual flexural strength $f_{R,i}$ is defined as in Eq. 2.10

$$f_{R,i} = \frac{3F_{R,i} L}{2bh_{sp}^2}$$

Eq. 2.10

where $F_{R,i}$ is the load corresponding to CMOD_i, as shown in Figure 2.7.

$f_{eq,2}, f_{R,1}$ are used in the verification of the serviceability limits and $f_{eq,3}, f_{R,4}$ are considered at the ultimate limit state.

2.4 Calculation of Residual Strengths per ASTM C1609

ASTM C1609 evaluates the flexural parameters of fiber reinforced concrete using residual strengths derived from the load-deflection curve obtained by testing a simply supported beam under third-point loading. ASTM C1609 uses the following terminology:

2.4.1 Calculated Parameters

First-peak strength, f_1:

The first-peak load, P_1 is the load value at the first point on the load-deflection curve where the slope is zero. The deflection at this point is the first-peak deflection, δ_1. First peak strength, f_1, is the stress at the first-peak load obtained using Eq. 2.11.

$$f_1 = \frac{P_1 L}{bd^2} \qquad \text{Eq. 2.11}$$

where:

f_1 = first-peak strength, MPa

P_1 = first- peak load, N

b = the average width of the specimen at the fracture, as oriented for testing, mm, and

d = the average depth of the specimen at the fracture, as oriented for testing, mm.

Residual Strengths, f_{600} and f_{150}

The residual loads, P_{600} and P_{150}, are the load values corresponding to a net deflection of $L/600$ and $L/150$ respectively. The flexural stresses at these loads are

called the residual stresses, f_{600} and f_{150} respectively and can be obtained using Eq. 2.12 and 2.13.

$$f_{600} = \frac{P_{600}L}{bd^2} \qquad \text{Eq. 2.12}$$

$$f_{150} = \frac{P_{150}L}{bd^2} \qquad \text{Eq. 2.13}$$

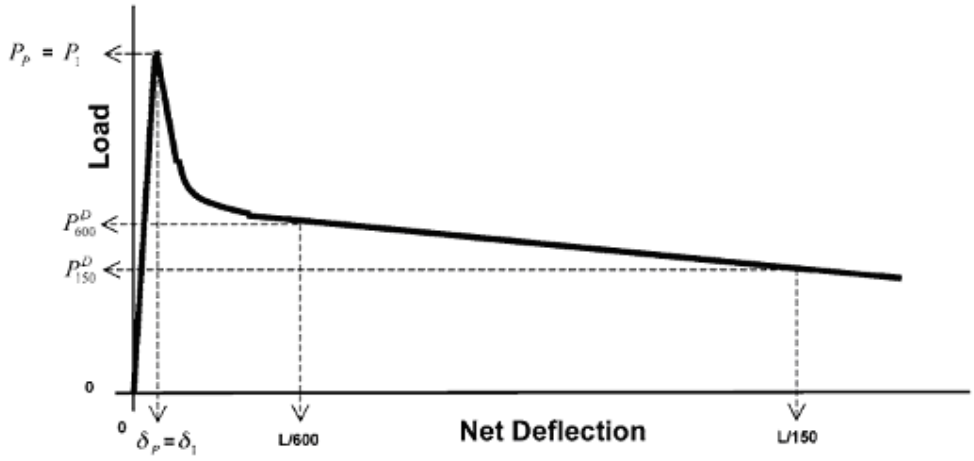

Figure 2.8: Parameter calculations for first-peak load equal to peak Load. (ASTM C 1609 - 07)

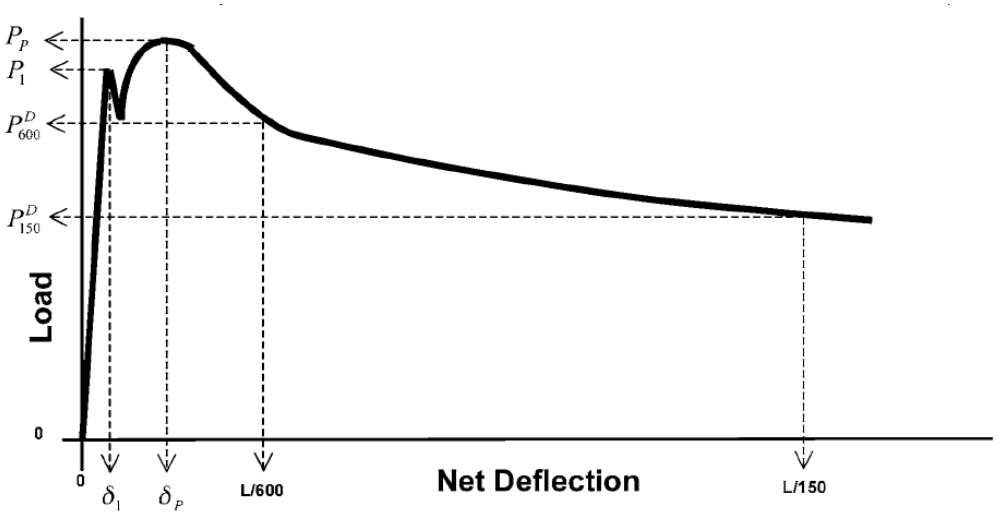

Figure 2.9: Parameter calculations for first-peak load less than peak Load. (ASTM C 1069 – 07)

2.5 Cracked Hinge model

The cracked hinge model was first proposed by Ulfkjaer et al. (1995) and then further developed by Pedersen (1996), Stang and Olesen (1998, 2000) and Olesen (2001). The advantage of the hinge model is that it presents closed-form analytical solutions for the entire stress-crack opening (σ-w) curve.

The cracked hinge model describes the crack as a local discontinuity. The hinge can be modeled as incremental horizontal strips of spring elements attached at each end to a rigid boundary. The discontinuity (hinge) is confined to a certain region of width s. Outside these rigid boundaries the uncracked element can be modeled using classical beam theory or appropriate elastic theory. The hinge may be used in modeling three point bending beams in which the springs can be modeled using the fictitious crack method assuming the springs to be linear elastic in the pre-crack state and by using a bilinear σ-w curve in the cracked state, as seen in Figure 2.11 and Eq. 2.11.

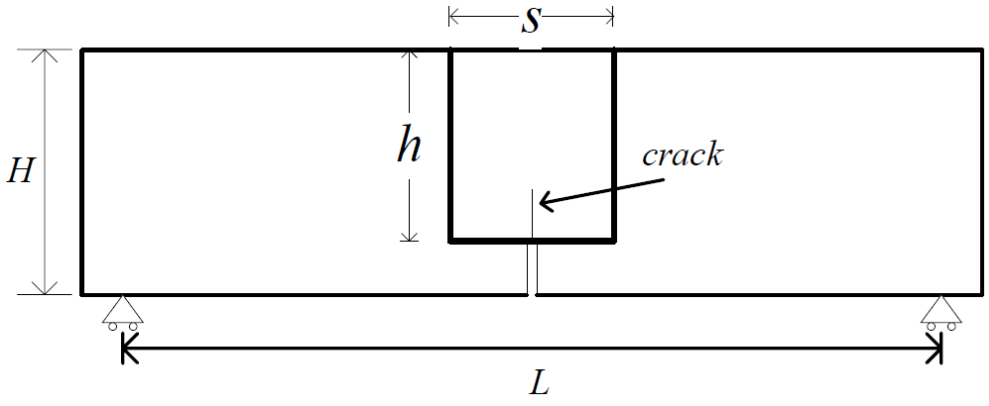

Figure 2.10: Geometry of test specimen and cracked hinge.

$$\sigma = \begin{cases} E\varepsilon & pre-crack\ state \\ \sigma_w(w) = g(w) f_t & cracked\ state \end{cases} \qquad \text{Eq. 2.11}$$

where E = elastic modulus; ε = elastic strain; $\sigma_w(w)$ denotes the stress crack opening relationship with w = crack opening; and f_t = uniaxial tensile strength . The function $g(w)$ is defined as:

$$g(w) = b_i - a_i w = \begin{cases} b_1 - a_1 w & 0 \le w < w_1 \\ b_2 - a_2 w & w_1 \le w \le w_2 \end{cases} \qquad \text{Eq. 2.12}$$

where $b_1 = 1$; and w_1 and w_2 are the limits given by the intersection of the two line segments, and the intersection of the second line segment and the abscissa respectively.

$$w_1 = \frac{1 - b_2}{a_1 - a_2};\ w_2 = \frac{b_2}{a_2} \qquad \text{Eq. 2.13}$$

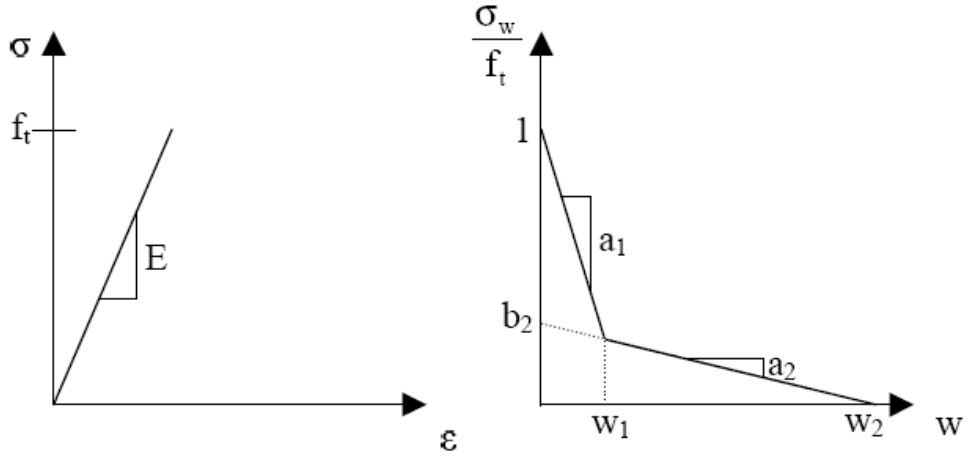

Figure 2.11: Material model for precrack and cracked state of concrete.

As already mentioned, the boundaries of the hinge are rigid. It is assumed that these rigid boundaries may rotate, as shown in Figure 2.12. The deformation of the hinge can be expressed in terms of the angular deformation, φ and the depth to the neutral axis, y_0. Olesen (2001) proposed analytical solutions to obtain the

external moment and the axial force, by the analyzing the hinge element, for any angular deformation φ. The solution is presented in terms of normalized properties, using the following the normalizations:

$$\beta_1 = \frac{f_t a_1 s}{E}, \beta_2 = \frac{f_t a_2 s}{E} \qquad \text{Eq. 2.14 (a,b)}$$

$$c = \frac{(1-b_2)(1-\beta_1)}{(\beta_2 - \beta_1)} \qquad \text{Eq. 2.15}$$

$$\mu = \frac{6}{f_t h^2 t} M, \rho = \frac{1}{f_t h t} N, \theta = \frac{hE}{s f_t} \varphi \text{ and } \alpha = \frac{d}{h} \qquad \text{Eq. 2.16 (a – d)}$$

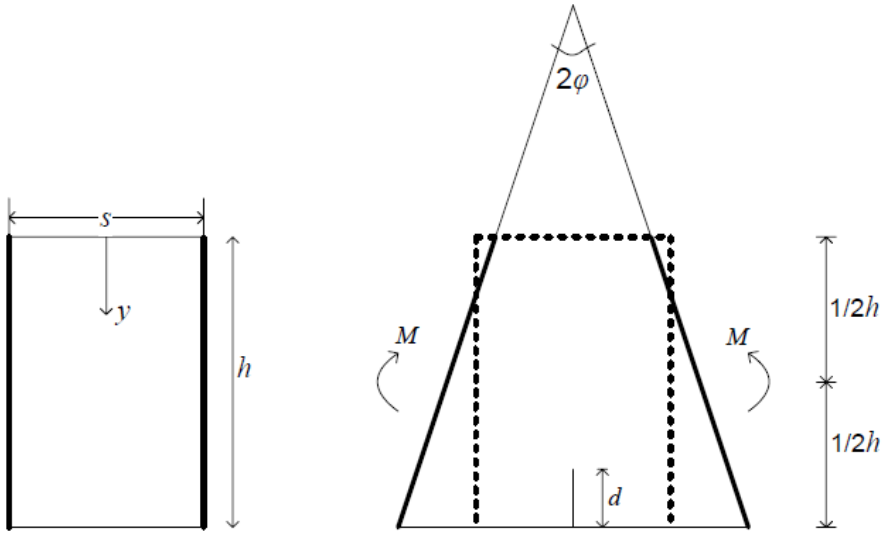

Figure 2.12: Geometry, loading and deformation of cracked hinge.

The solution is presented for four different phases of stress distribution. The first phase or Phase 0 represents the elastic state and Phases I, II and III represent the different phases of crack propagation, as shown in Figure 2.13.

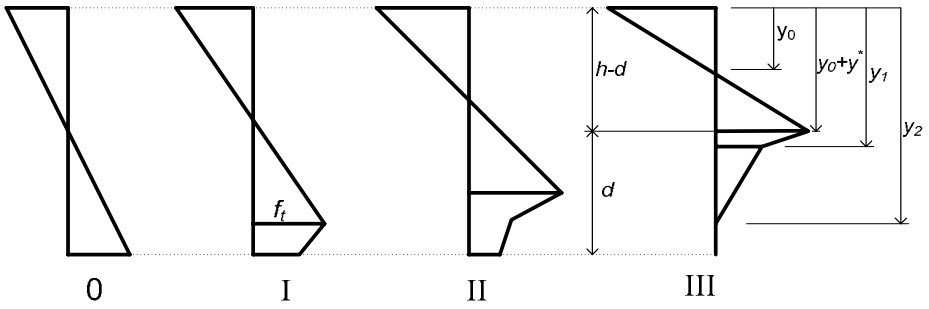

Figure 2.13: Four phases of stress distribution in elastic layer of hinge.

The analytical solutions express the normalized moment μ and the normalized crack depth α as functions of the normalized hinge deformation θ and normalized axial force ρ.

Phase 0 (Elastic Phase): $0 \le \theta \le \theta_{0\text{-I}}$

$$\alpha = 0 \qquad \text{Eq. 2.17a}$$

$$\mu = \theta \qquad \text{Eq. 2.17b}$$

Phase I: 1 - $\theta_{0\text{-I}} \le \theta \le \theta_{\text{I-II}}$:

$$\alpha = 1 - \beta_1 - \sqrt{(1-\beta_1)\left(\frac{1-\rho}{\theta} - \beta_1\right)} \qquad \text{Eq. 2.18a}$$

$$\mu = 4\left(1 - 3\alpha + 3\alpha^2 - \frac{\alpha^3}{1-\beta_1}\right)\theta + (6\alpha - 3)(1-\rho) \qquad \text{Eq. 2.18b}$$

Phase II: $\theta_{\text{I-II}} \le \theta \le \theta_{\text{II-III}}$:

$$\alpha = 1 - \beta_2 - \frac{1-b_2}{2\theta} - \sqrt{(1-\beta_2)\left(\frac{(1-b_2)^2}{4\theta^2(\beta_1-\beta_2)} - \beta_2 + \frac{b_2-\rho}{\theta}\right)} \qquad \text{Eq. 2.19a}$$

$$\mu = 4\left(1 - 3\alpha + 3\alpha^2 - \frac{\alpha^3}{1-\beta_2}\right)\theta + (6\alpha - 3)(1-\rho) - \frac{(1-b_2)\left(3\alpha^2 - \left(\frac{c}{2\theta}\right)^2\right)}{1-\beta_2} \qquad \text{Eq. 2.19b}$$

Phase III: $\theta_{\text{II-III}} < \theta$:

$$\alpha = 1 - \frac{1}{2\theta}\left(1 + \sqrt{\frac{(1-b_2)^2}{\beta_1 - \beta_2} + \frac{b_2^2}{\beta_2^2} - 4\rho\theta}\right) \qquad \text{Eq. 2.20a}$$

$$\mu = 4\left(1 - 3\alpha + 3\alpha^2 - \alpha^3\right)\theta + (6\alpha - 3)(1-\rho) - 3\alpha^2 + \frac{1}{4\theta^2}\left(1 - \frac{b_2}{\beta_2}\right)\left(1 - \frac{b_2}{\beta_2} + c\right)\left(1 + \frac{\beta_1 c}{1-\beta_1}\right) + \left(\frac{c}{2\theta}\right)^2 \qquad \text{Eq. 2.20b}$$

The transition points $\theta_{0\text{-I}}$, $\theta_{\text{I-II}}$, and $\theta_{\text{II-III}}$ are given by:

$$\theta_{0-\text{I}} = 1 - \rho \qquad \text{Eq. 2.21a}$$

$$\theta_{\text{I-II}} = \frac{1}{2}\left(1 - \rho - c + \sqrt{(1-\rho-c)^2 + \frac{c^2}{\beta_1 - 1}}\right) \qquad \text{Eq.2.21b}$$

$$\theta_{\text{II-III}} = \frac{1}{2}\left(\begin{array}{l}\rho(\beta_2 - 1) + \dfrac{b_2}{\beta_2} \\ + \sqrt{\rho^2(\beta_2-1)^2 + 2\rho(\beta_2-1)\dfrac{b_2}{\beta_2} + \dfrac{(1-b_2)^2}{\beta_1 - \beta_2} + \dfrac{{b_2}^2}{{\beta_2}^2}}\end{array}\right). \qquad \text{Eq. 2.21c}$$

The crack mouth opening displacement (CMOD) due to the opening of the crack is given by:

$$\text{CMOD}_{\text{COD}} = \frac{sf_t}{E}\frac{1 - b_i + 2\theta}{1 - \beta_i} \qquad \text{Eq. 2.22}$$

where

$$(b_i, \beta_i) = \begin{cases} (1, \beta_1) & \text{in Phase I} \\ (b_2, \beta_2) & \text{in Phase II} \\ (0,\ 0) & \text{in Phase III} \end{cases} \qquad \text{Eq. 2.23}$$

In the case of a notched beam, since the CMOD is measured at the bottom of the notch, the elastic deformation of the beam also contributes to the CMOD. Tada et al. (1985) proposed an analytical expression to calculate the CMOD due to elastic deformation as a function of the beam and the notch dimensions, as seen in Eq. 2.23.

$$\mathrm{CMOD}_e = \frac{6PLa_0}{EtH^2} v_1(x) \qquad \text{Eq. 2.24}$$

where

$$v_1(x) = 0.76 - 2.28x + 3.87x^2 - 2.04x^3 + \frac{0.66}{(1-x)^2},\ x = \frac{a_0}{H} \qquad \text{Eq. 2.25}$$

and, P = load applied at the midspan of the beam; L = span of the beam; a_0 = notch depth; E = elastic modulus; t = thickness of the beam; H = full depth of the beam.

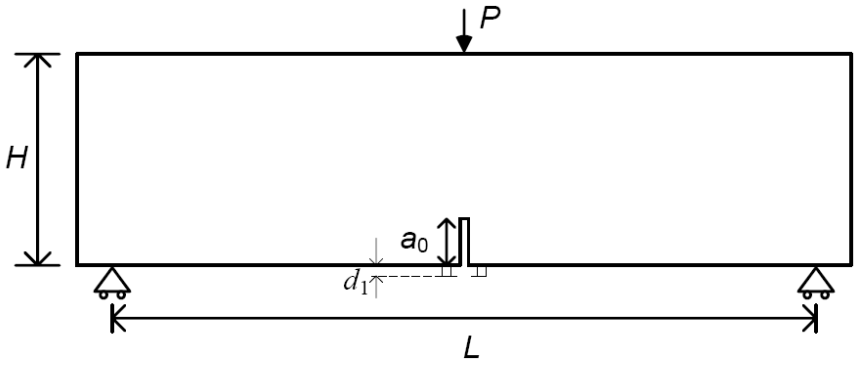

Figure 2.14: Geometry of a three point bending test specimen.

Karihaloo & Nallathambi (1991) proved that the contribution of the depth of the knife edges d_1, used to measure the CMOD, is significant in the measurement of the CMOD and must be taken in to account, by simply assuming that beam thickness is $H+d_1$ and the initial notch length is a_0+d_1, thus modifying the variable in Eq. 2.24 to:

$$x = \frac{a_0 + d_1}{H + d_1} \qquad \text{Eq. 2.26}$$

However, Stang (2000), assuming that the crack sides are straight, proposed a simple geometric correction of Eq. 2.26:

$$\upsilon_1' = \frac{a_0 + d_1}{a_0}\upsilon_1 \qquad \text{Eq. 2.27}$$

In the present study the correction proposed by Stang (2000) is adopted.

Since the CMOD is measured at a distance from the notch tip, this contributes to the geometrical opening, $CMOD_g$, which can be calculated as given by Stang (2000):

$$CMOD_g = 2a_0 \frac{sf_t}{hE}(\theta - 1) \qquad \text{Eq. 2.28}$$

Combining all the different contributions, the final CMOD can be calculated as:

$$CMOD = CMOD_e + CMOD_{COD} + CMOD_g \qquad \text{Eq. 2.29}$$

It can be seen from Eqs 2.17-2.20 and Eq. 2.29 that the normalized moment μ and CMOD depend on the normalized hinge deformation θ. By increasing θ incrementally, μ and CMOD can be obtained in all the four phases of crack propagation. The load at midspan, P, can then be obtained using Eq. 2.30.

$$P = \frac{4M}{L} = \frac{2}{3}\frac{f_t h^2 t}{L}\mu \qquad \text{Eq. 2.30}$$

Therefore, the complete P-CMOD curve can be obtained, if the σ-w curve (softening curve) and the elastic modulus of concrete, E, are known.

2.6 Inverse Analysis

An inverse problem or inverse analysis can be defined as the task of obtaining the model parameters from observed data. In the present case the inverse problem is to obtain the parameters defining the σ-*w* curve (model) when the *P*-CMOD curve is known (observed data).

Similarly if the *P*-CMOD curve is obtained experimentally then the *σ*-*w* curve can be obtained by comparing the experimentally obtained *P*-CMOD curve and the *P*-CMOD curve analytically obtained from an initially assumed *σ*-*w* curve. The parameters defining the *σ*-*w* curve can then be changed such that the predicted *P*-CMOD closely matches the experimental curve. The process of changing the variables would be really tedious if done by hand and therefore optimization algorithms are used (Ostergaard, 2003; Sousa and Gettu 2006; Kitsutaka 1997). This process can be implemented by the use of computer programs such as Matlab.

In these optimization algorithms, the main goal is to minimize the error between the predicted and the experimental *P*-CMOD curve. An error function is formulated, which can be defined as the normalized difference between the areas of the predicted and experimental *P*-CMOD curve, A_{exp} and A_{pre} over a given CMOD range, as in Eq. 2.30, or the summation of squares of the difference of the predicted and experimental loads, P_{exp} and P_{num} respectively for a particular CMOD over the whole range of CMOD, as in Eq. 2.31

$$\text{Error} = \frac{\left| A_{\exp} - A_{pre} \right|}{A_{\exp}} \qquad \text{Eq. 2.30}$$

$$\text{Error} = \int_0^{w_{\max}} \left(P_{\exp}(w) - P_{num}(w)\right)^2 dw \qquad \text{Eq. 2.31}$$

where P_{exp} is the experimental load and P_{num} is the numerically predicted load.

The objective of the optimization algorithms is to minimize the error function by changing the independent variables which in this particular case are the parameters defining the σ-w curve, thereby obtaining the σ-w curve corresponding to the experimental P-CMOD curve. This process of obtaining the model parameters by back calculating the σ-w curve from the P-CMOD curve is referred to as inverse analysis.

Roelfstra and Wittmann (1986) were the first to propose inverse analysis to determine the tension softening diagram for concrete. The algorithm developed could only be used for bilinear-type softening diagrams and required the first guess of the input parameters to be close to the iteration results. In this method finite element analysis is applied to calculate the predicted response for a given set of parameters and optimization problem is setup for the entire curve. A possible problem with such an approach is that the correlation between the modulus of elasticity, E, tensile strength, f_t and a_1 and the error function for the entire curve weak. This five dimensional problem is also more likely to find local minima rather than the global minima.

Stang and Olesen (1998) developed the cracked hinge model, based on the work done by Ulfkjaer (1995). Ostergaard (2003) developed an algorithm for inverse analysis based on the cracked hinge model and incorporated it into a Matlab program. In this program a step wise (multi-step) inverse analysis was performed to obtain the complete σ-w curve. Although a step wise analysis was performed,

the values obtained in this program require an initial guess and optimization should be run more than once to obtain at the exact result.

2.6.1 Ostergaard (2003)

Ostergaard (2003) proposed an inverse analysis algorithm based on the hinge model explained in Section 2.5. In this algorithm the optimization problem is solved in steps corresponding to the different phases of crack propagation. This is possible since the hinge model proposes an analytical solution which clearly distinguishes between the different phases of crack propagation.

In the algorithm proposed by Ostergaard (2003), Step 1 is the determination of the modulus of elasticity by conducting the optimization in the elastic phase. This is done by considering the modulus of elasticity as the only variable and including the data points belonging only to the elastic phase. So, the optimization problem reads:

Step 1: Determination of Elastic Modulus:

$$\min_{E} \frac{1}{N^0_{\max}} \sum_{0}^{N^0_{\max}} \left(P_{\exp} - P_{calc}\right)^2 \qquad \text{Eq. 2.32}$$

subject to $E > 0$, where $N^0_{\max}$ represents the last observation made belonging to Phase 0 and P_{exp} and P_{calc} represent the experimentally and analytically obtained load values respectively at a particular CMOD.

After determining the modulus of elasticity, the factors representing the bilinear stress-crack opening curve – f_t, a_1, a_2 and b_2 are then determined in a two step procedure. This procedure again takes advantage of the analytical solutions

proposed for the different phases of crack propagation. Step 2 is the determination of f_t and a_1, and in contrast to Step 1; all observations are included in the optimization process. After determining f_t and a_1, Step 3 is the final step in which a_2 and b_2 are then found to obtain the stress-crack opening curve. Step 2 and 3 can be expressed as:

Step 2: Determination of f_t and a_1:

$$\min_{(f_t,a_1)} \frac{1}{N_{\max}} \sum_{0}^{N_{\max}} \left(P_{\exp} - P_{calc}\right)^2 \qquad \text{Eq. 2.33}$$

subject to $f_t > 0$.

Step 3: Determination of a_2 and b_2:

$$\min_{(a_2,b_2)} \frac{1}{N_{\max}} \sum_{0}^{N_{\max}} \left(P_{\exp} - P_{calc}\right)^2 \qquad \text{Eq. 2.34}$$

where N_{max} represents the total number of observations.

In this algorithm, to obtain the last observation made belonging to Phase 0, $N^0_{\max}$, Ostergaard uses a corresponding CMOD of:

$$CMOD^0 = 4a_0 \frac{f_t}{E}\left(\frac{h}{H}\right)^2 \upsilon_1 \qquad \text{Eq. 2.35}$$

where f_t represents the tensile strength of concrete, a_0 represents the notch depth, h and H represent the un notched and the full depth of the beam, as shown in Figure 2.10. From Eq.2.35 it can be seen that an initial guess of the tensile strength, f_t, should be made to determine the number of observations to be included in the optimization process to calculate the modulus of elasticity. If the initial guess of the tensile strength, f_t, in Step 1 differs from the f_t, determined in Step 2, the optimization has be to rerun using the new f_t in Eq. 2.35. Therefore, in this

particular algorithm, several runs would be required by changing the initial guess for f_t to evaluate the modulus of elasticity.

To determine (f_t, a_1) and (a_2, b_2), in Steps 2 and 3 respectively, Ostergaard (2003) includes all the observations in the test in the optimization process, as shown in Eqs. 2.33 and 2.34.

2.6.2 Sousa and Gettu (2006)

Sousa and Gettu (2006) proposed another optimization algorithm, which was implemented in a software program called FIT3PB, for the determination of the σ-w relation using the load versus crack mouth opening displacement (P-CMOD) curves obtained from notched beam tests. In this program the user can choose the shape of the σ-w curve from:

1. The Hordjik's model (Hordjik 1991) with two parameters, f_t and G_f (see Figure 2.15a)

$$\frac{\sigma(w)}{f_t} = \left[1 + \left(c_1 \frac{w}{w_{ult}}\right)^3\right] e^{(-c_2 w / w_{ult})} - \frac{w}{w_{ult}}\left(1 + c_1^3\right) e^{-c_2} \qquad \text{Eq. 2.36}$$

   where $c_1 = 3.0$; $c_2 = 6.93$; and $w_{ult} = 5.136\ G_f/f_t$.

2. A sloped-constant model with three parameters, f_t, a_1, and b_2 (see Figure 2.15b)

$$\frac{\sigma(w)}{f_t} = \begin{cases} 1 - a_1 w & \text{if } w < w_1 \\ b_2 & \text{if } w \geq w_1 \end{cases} \qquad \text{Eq. 2.37}$$

3. A bilinear model, with four parameters f_t, a_1, a_2 and b_2 (see Figure 2.15c)

$$\frac{\sigma(w)}{f_t} = \begin{cases} 1 - a_1 w & \text{if } w < w_1 \\ b_2 - a_2 w & \text{if } w \geq w_1 \end{cases} \qquad \text{Eq. 2.38}$$

4. A trilinear model with six parameters, f_t, a_1, a_2, b_2, a_3 and b_3 (see Figure 2.15d)

$$\frac{\sigma(w)}{f_t} = \begin{cases} 1 - a_1 w & \text{if } w < w_1 \\ b_2 - a_2 w & \text{if } w_1 \le w \le w_2 \\ b_3 - a_3 w & \text{if } w \ge w_2 \end{cases} \qquad \text{Eq. 2.39}$$

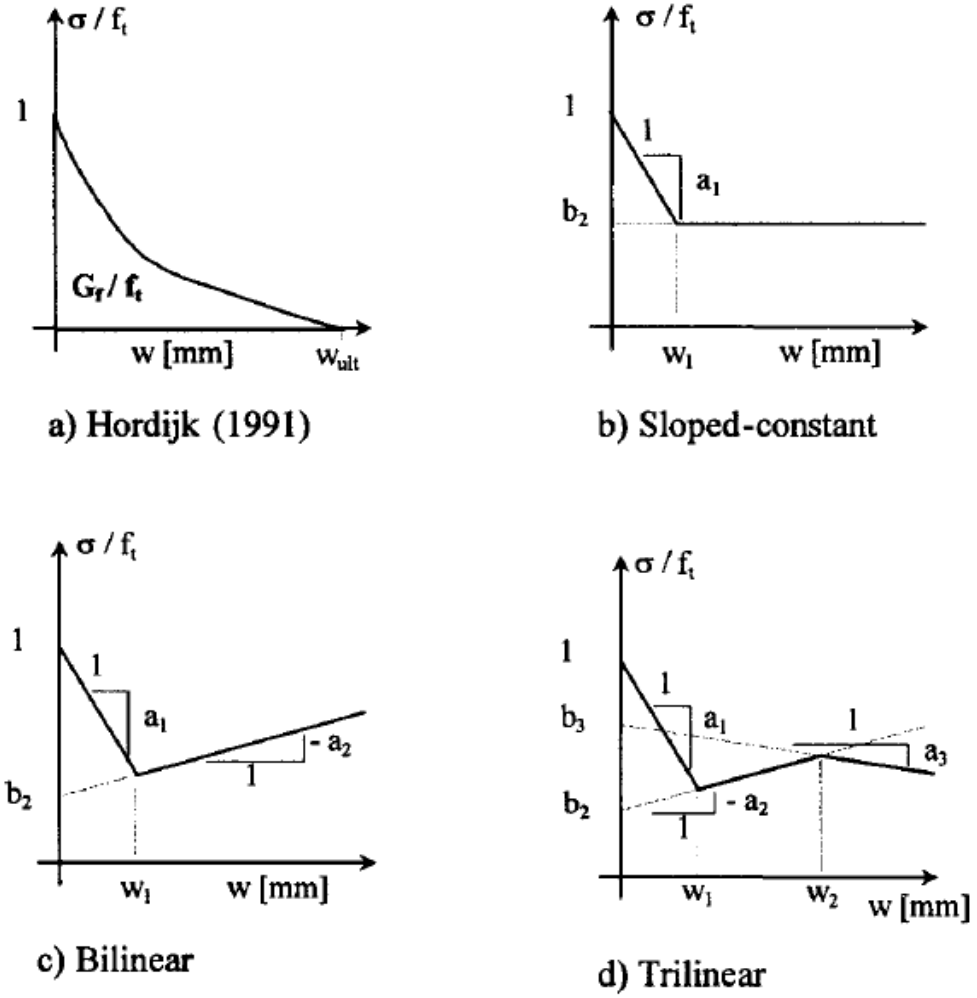

Figure 2.15: Softening models and corresponding parameters. (Sousa and Gettu, 2006).

The fitting error function used in this process is defined as

$$\text{Error} = \int_0^{N_{max}} \left[P_{\exp} - P_{num} \right]^2 \psi dw \qquad \text{Eq. 2.40}$$

where N_{max} = total number of observations in the target experimental curve; ψ = weighting function introduced to permit unequal importance of different portions of the fitting interval, according to the desired application; P_{exp} and P_{num} =

respectively, the experimental and numerical values of the load corresponding to the same abscissa.

In this algorithm the minimization of the objective function or the fitting error function in Eq. 2.40 is performed through optimization techniques in n-dimensional space, where n = number of parameters that are free to vary. Therefore, all the parameters (E, f_t, a_1, a_2 and b_2) required to define the bilinear softening curve (σ-w curve) in this particular algorithm (Sousa and Gettu, 2006), can be obtained in a single step optimization. Sousa and Gettu (2006) also propose the use of a weighing function ψ to assign unequal weights to different regimes of the P-CMOD curve. It is stated that weighting becomes important in the case of behavior that needs more complex models, as in inverse analysis of notched SFRC beam with a trilinear model where the importance of weighting function is related to the fitting interval of CMOD.

Sousa and Gettu (2006) suggest that, in case of a large fitting interval (the interval in which the inverse analysis is performed), say [0.0–2.0 mm], the fits of P-CMOD curve vary significantly, especially around the peak, when the predictions are made with inverse analyses performed with and without weighting.

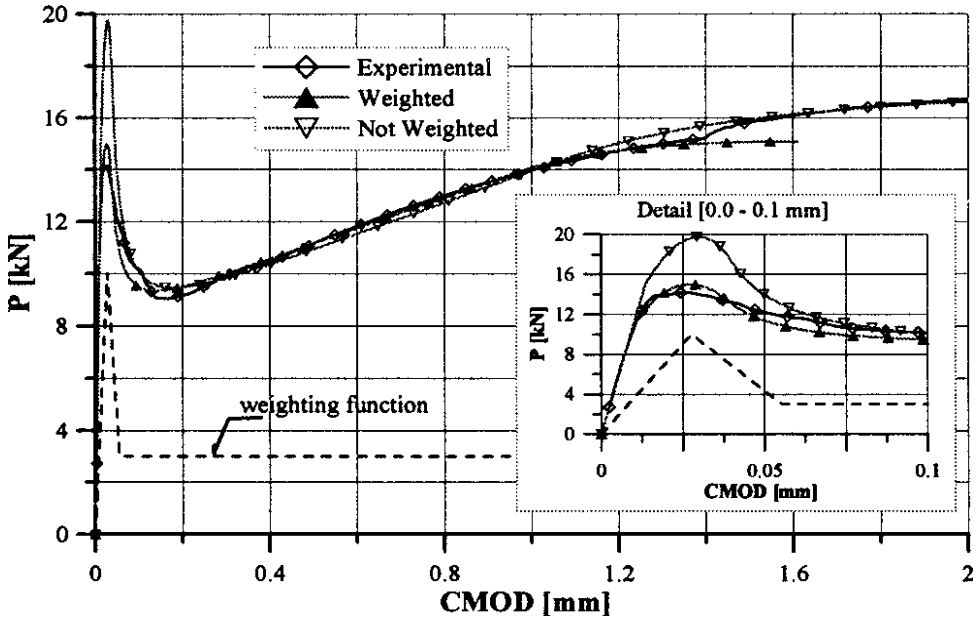

Figure 2.16: Effect of a weighing function on the *P*-CMOD curve for SFRC. Inverse analysis was performed in the interval [0.0 - 2.0 mm] (Sousa and Gettu, 2006)

Fig 2.16 shows the effect of the weighting interval in which there is a relatively higher weight (i.e., 10) for the peak and a linear increase in the prepeak regime and a symmetric decrease in the postpeak regime, followed by a constant value 1. It is concluded by Sousa and Gettu (2006) that with a higher weight for the initial part of the *P*-CMOD curve, a better fit of the peak load is obtained, while equal weighing of all the regimes leads to a better fit of the later regimes. It is also concluded that equal weighting tends to give higher tensile strength leading to an overestimation of the peak load, as shown in Fig 2.17.

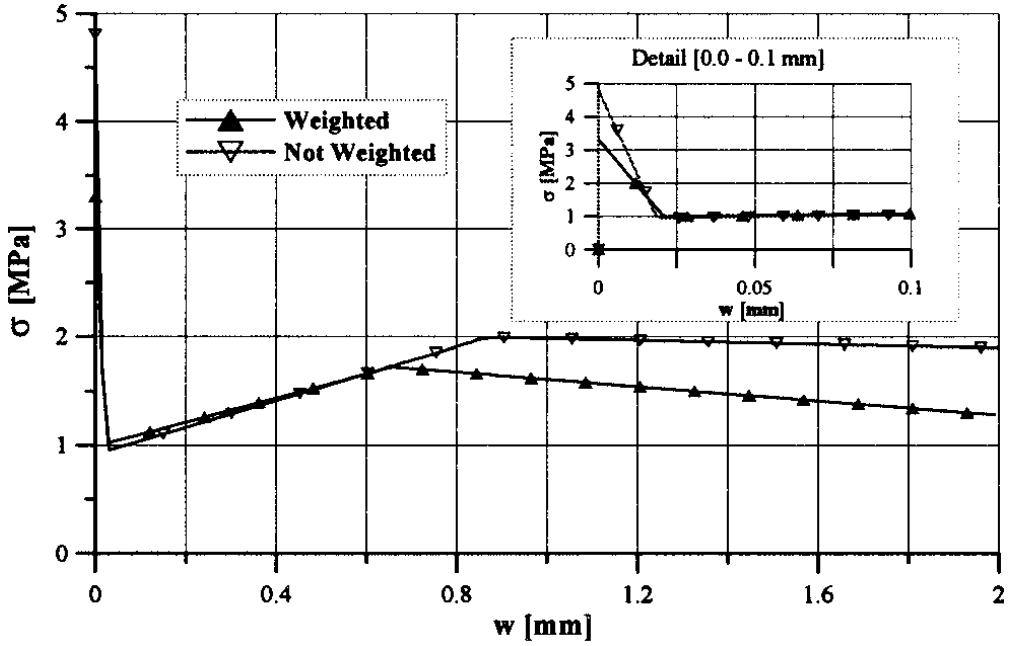

Figure 2.17: Effect of weighing function on the σ-w curve for SFRC performing inverse analysis in the interval [0.0; 2.0mm] (Sousa and Gettu, 2006)

2.6.3 Barros et al. (2005)

Barros et al. (2005) conducted more than two hundred flexural tests following RILEM TC 162-TDF (RILEM, 2002a) recommendations and evaluated the corresponding values of f_{eq} and f_R. Two types of hooked end DRAMIX steel fibers, RC 80/60 BN with a length (l_f) of 60 mm, a diameter (d_f) of 0.75 mm and an aspect ratio (l_f/d_f) of 80 and RC 65/60 BN with l_f = 60 mm, d_f = 0.92 mm and l_f/d_f = 65 were used in the study.

Barros et al. (2005) reported a linear trend between $f_{eq,2}$ and $f_{eq,3}$. They also found that $f_{eq,3}$ was slightly lower than $f_{eq,2}$ indicating that up to a deflection of δ_3 (= δ_L + 2.65 mm, where δ_L is the deflection at the limit of proportionality), the energy absorption capacity of the designed SFRC was maintained. A similar linear trend

between $f_{R,1}$ and $f_{R,4}$ was also reported, with $f_{R,4}$ being at about 93% of $f_{R,1}$, as shown in Figure 2.19.

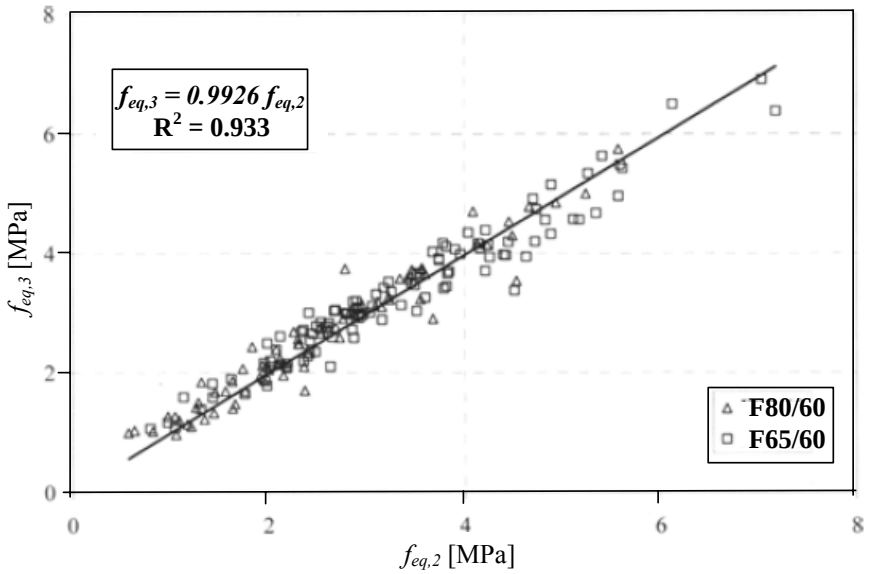

Figure 2.18: Relationship between $f_{eq,2}$ and $f_{eq,3}$.(Barros et al., 2005)

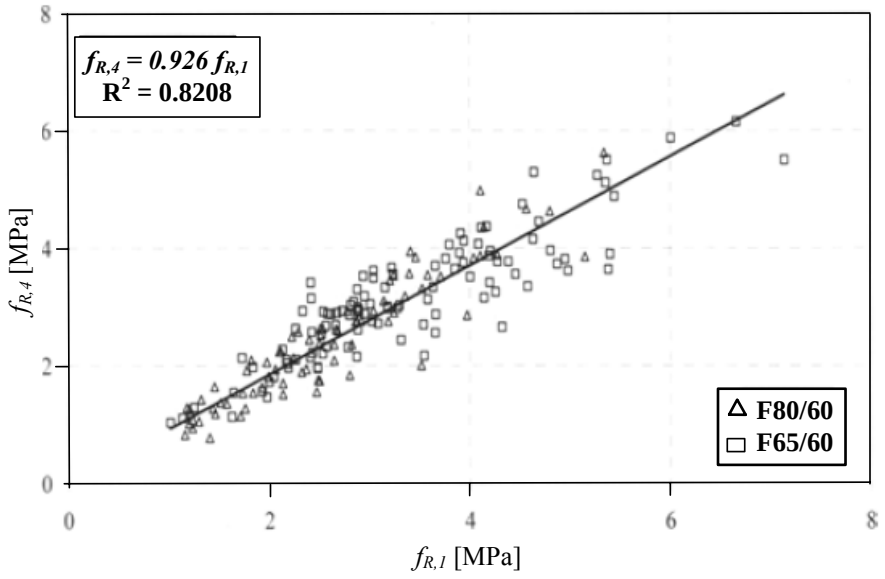

Figure 2.19: Relationship between $f_{R,1}$ and $f_{R,4}$. (Barros et al., 2005)

Chapter 3 Experimental Program:

3.1 Materials

The concrete specimens used in this study were prepared as part of a previous study, in which a total of four different fiber reinforced concrete mixtures were prepared (Hockenberry, 2007). The varied parameters being volume fraction of fibers, V_f, and fiber geometry (see Table 3.1 for mixture compositions). Two types of hooked-end Dramix® steel fibers; RC 80/60-BN and RC 65/35-BN, provided by Baekert were used (see Table 3.2). For each type of the steel fibers used two concrete mixtures with fiber volume fractions of 0.5% and 1.0% were prepared.

Table 3.1: Concrete mixture proportions. (3 cu yd = 2.3 m^3 per batch)

Batch	**Water** kg	**Cement** kg	**Coarse** kg	**Fine** kg	**Fiber** kg	**Fiber** %	**Desc.**
1	417	921	2223	1969	90	0.5	80/60 - 0.5%
2	389	862	2204	1978	181	1.0	80/60 - 1.0%
3	394	860	2232	1987	90	0.5	65/35 - 0.5%
4	400	896	2223	1923	181	1.0	65/35 - 1.0%

Table 3.2: Properties of steel fibers

Properties	**RC 65/35**	**RC 80/60**
Length (mm)	35	60
Aspect ratio, (length/diameter)	65	80
Tensile strength, N/mm^2	1100	1050

3.2 Test specimens and test matrix

As part of this study, beam specimens (dimensions 150 mm x 150 mm x 550 mm conforming to the recommendation of RILEM TC 162-TDF (RILEM, 2002a) were prepared and tested for three point bending tests to obtain load-deflection (P-δ) and load-crack mouth opening displacement (P-CMOD) data. The tested specimens had a span length of 500 mm and a midspan notch depth of 25 mm, as

shown in Figure 3.1. Cylinders (dimensions 100 mm x 200 mm) were also tested in this study for split tensile strength, compressive strength and modulus of elasticity. Table 3.2 shows the test matrix used in the experimental program.

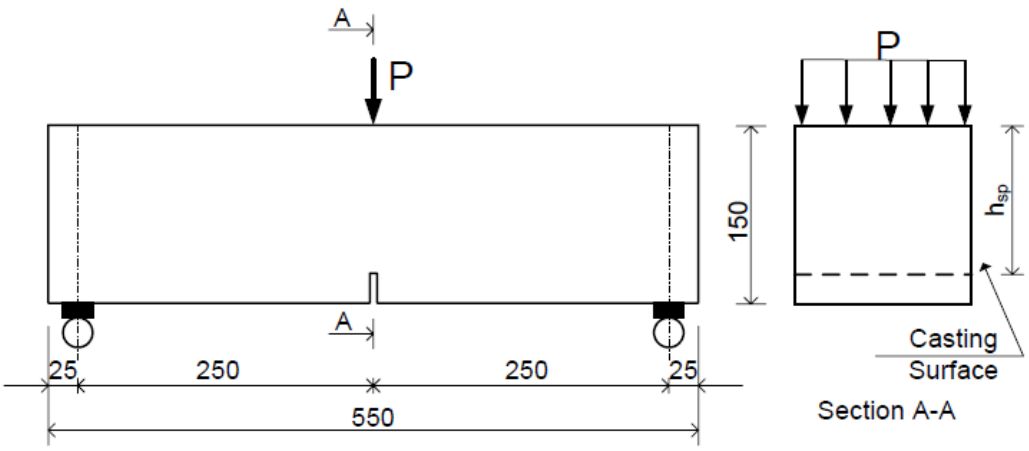

Figure 3.1: Geometry of 3PB test specimen.

Table 3.2 Test matrix

Test	Specimen Type	Specimen dimensions	# of specimens
Bending test	Beam	150 mm x 150 mm x 550 mm	5
Split cylinder test	Cylinder	100 mm x 200 mm	3
Compression strength test	Cylinder	100 mm x 200 mm	3

3.3 Test Setup and Procedure

3.3.1 Tensile strength

One of the unknown quantities during inverse analysis is the tensile strength of concrete. The splitting tensile test is widely used for determining the tensile strength of concrete and other cementitous materials (ASTM C496). The splitting tensile strength f_{st}, is calculated according to Eq 3.1, where D and L are the diameter and the length of the specimen and P_u is the failure load, as shown in Figure 3.2.

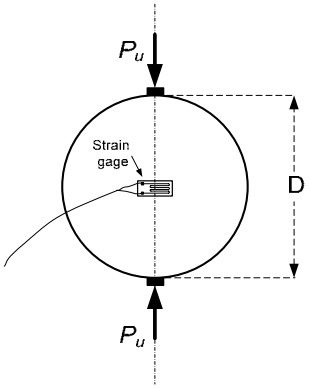

Figure 3.2: Test setup for split cylinder test.

$$f_{st} = \frac{2P_u}{\pi LD} \qquad \text{Eq. 3.1}$$

Strain gages (CEA-06-125UN-120, gage length = 0.125 in/3.18 mm) were also installed on the front face of the cylinder and the gages were installed perpendicular to the line of application of force. This was done to capture any crack initiation in this region or any change in phase from linear (elastic) to non-linear stress-strain distribution. The strain gage data was measured using a data acquisition system. The testing was done using a Tinius Olsen compression testing machine which can run only under load control. This machine displays load at any particular time, so load was measured at regular intervals and the strain gage data observed at corresponding load levels. For the split tensile tests the narrower the load-bearing strip the maximum tensile strength will approach the theoretical limit for the tensile strength of concrete (Timoshenko and Goodier, 1970). In a recent study Rocco et al., (1999) found that the results of this type of test are sensitive to the ratio $\frac{b}{D}$ (b =width of the strip), loading rate, geometry, and specimen size (D). The same study also mentions that for a ratio $\frac{b}{D}$ equal to 0.04, the splitting tensile strength of plain concrete, f_{st}, becomes independent of the specimen size. Another study by Coronado (2006) shows that the tensile strength values become less

sensitive to $\frac{b}{D}$ ratio for values less than 0.08 and in such case the split tensile strengths obtained are also equal to the strengths obtained from prisms. Therefore, assuming the same would be true for fiber reinforced concrete, load bearing plate of width of 0.6 mm ($\frac{b}{D}$=0.03 < 0.08) was used for all the split tensile tests.

3.3.2 Compression Tests and Elastic Modulus

Elastic modulus is one of the unknown quantities in the inverse analysis approach and is also one of the most important properties used to model the behavior of concrete. To obtain the elastic modulus, compression tests were done on concrete cylinders using a Tinius Olsen machine. Strain gages (Type - FLA-30-11, gauge length = 30 mm) were installed on the concrete cylinders, shown in Figure 3.3, along the line of application of load to measure the longitudinal strain during the test. Strain data was recorded using a data acquisition system and the load displayed by the testing machine was recorded at regular intervals during the test. The test was performed conforming to ASTM C 469.

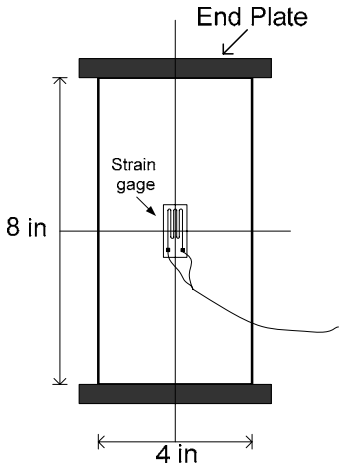

Figure 3.3: Test setup for compressive strength test.

Table 3.3: Compressive strength and split tensile strengths for all the specimens tested.

Concrete Type	Compressive Strength, f'_c (MPa)	Elastic Modulus, E (GPa)	Tensile Strength, f_t (MPa)
65/35 - 0.5%	28	20	3.0
	27	21	3.2
	28	-	-
80/60 - 0.5%	31	24	2.4
	29	24	3.2
	27	-	2.8
65/35 - 1%	36	30	3.7
	36	30	3.7
	34	-	-
80/60 - 1%	30	18	5.1
	27	19	4.0

3.3.3 Three Point Bending (3PB) Test

The bending tests were performed using a hydraulic actuator, with a capacity of 98 kN. The actuator is attached to a self contained load frame, which also houses the reaction beam. Testing was accomplished using an MTS Flextest computer controller, which controls the load and displacement actuator. Another computer served as the data acquisition system, which is run by LabVIEW. The LabVIEW software allows for multiple measurement systems to be monitored and recorded simultaneously, at high speed.

Reference Frame

A reference frame, shown in Figure 3.4, was used to measure the load point displacement. The load point displacement is determined relative to the point of application of load and is measured directly below the loading points,on either side of notch. This is done to avoid measuring the inelastic deformations at the supports. Two LVDTs which are attached to the reference frame one on each side of the specimen measure the deflection of two aluminum plates which are attached

to the base of the specimen. These aluminum plates which are tightly screwed to the base of the specimen on either side of the notch are also used to mount the knife edges used for measuring the crack mouth opening displacement.

Test Setup

1. The loading head is cylindrical with a circular boundary of a radius of 50 mm and a length greater than the thickness of the specimen. The loading block is suspended to the machine head and is free to rotate in all the directions to accommodate small specimen imperfections without introducing torsion.
2. As required by the RILEM TC 162-TDF (RILEM, 2002a) two hardened steel rollers are used as supports for the beam.
3. Ground hardened steel plates having a width of 50 mm and depth 25 mm were placed between the specimen and the rollers.

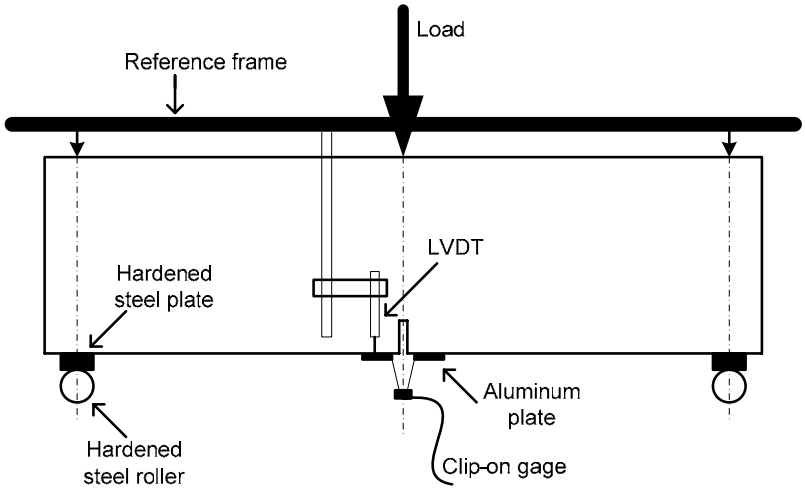

(a)

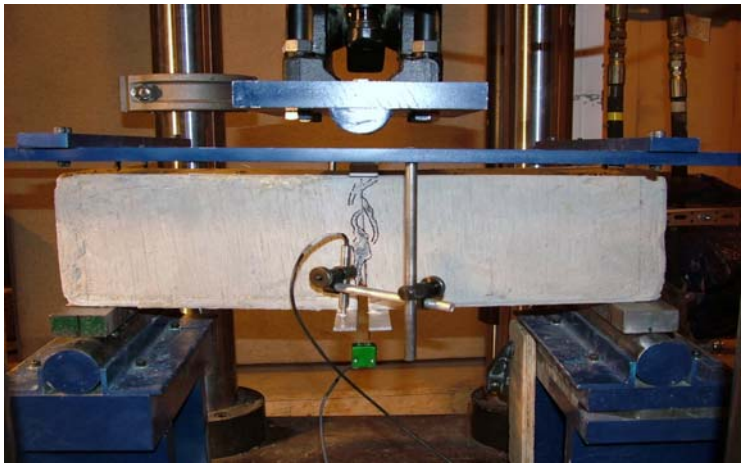

(b)

Figure 3.4: Test setup for three point bending tests.

Test procedure and data collection

All the bending tests were performed as per the recommendations of RILEM TC 162-TDF (RILEM, 2002a). The bending tests were carried out using a three point loading setup, applying the load at the midspan of the beam. For fiber reinforced concrete the bending tests were executed by means of displacement control. To accommodate for the settling of the beam and the loading head during the initial part of the loading, the load at the midspan of the beam was applied at a constant

rate of 2 kN/min until the applied load reached 2 kN. The test was then continued using displacement control such that the deflection of the beam at the midspan increases at a constant rate of 0.2 mm/min. During testing the value of load (P), deflection at midspan (δ) and the CMOD were continuously recorded using a data acquisition system at a frequency of 10 Hz or 10 observations per second, until the end of the test.

A clip-on gage with a gage length of 15 mm was used to measure the CMOD. As suggested by RILEM TC 162-TDF (RILEM, 2002a), the initial spacing between the knife edges was kept less than 5 mm and therefore a maximum CMOD of 10 mm could be recorded by the clip-on gage. The tests were carried until the clip-on gage reached its maximum limit of 15 mm or until a CMOD of 10 mm was reached.

3.4 Analysis of test data

From the data recorded during the bending tests load-deflection (P-δ) and load-CMOD (P-CMOD) plots for the different concrete mixtures were prepared. The typical load-CMOD and load-deflection plots for all the different mixtures can be seen in Figures 3.5 and 3.6.

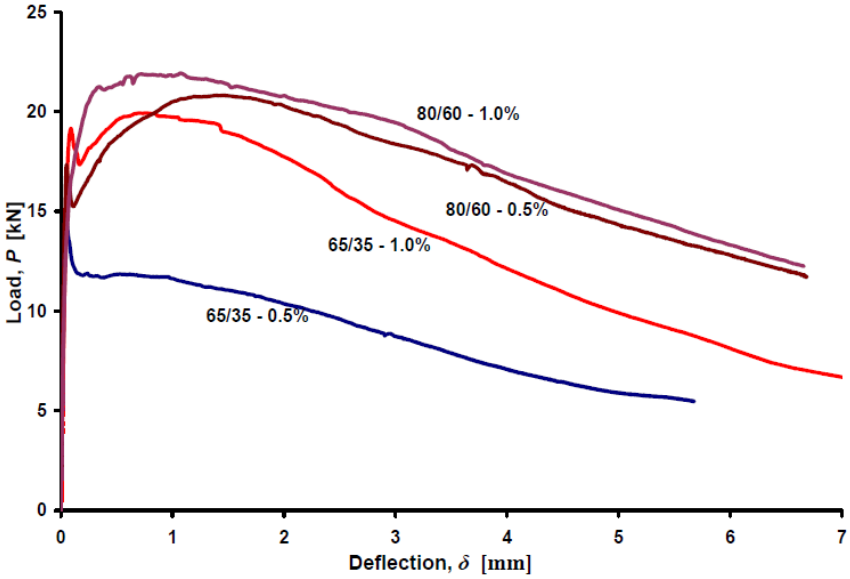

Figure 3.5: Plot showing the typical experimental load-deflection curves.

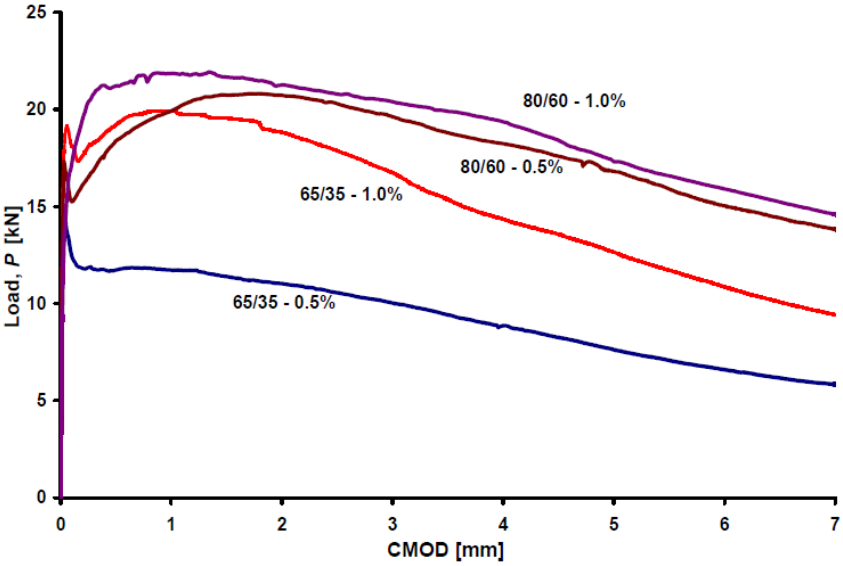

Figure 3.6: Plot showing the typical load-CMOD curves.

3.4.1 Peak Loads

The peak loads for all the specimens tested are shown in Figure 3.7. It can be seen that the peak loads for the 80/60-1.0% mixture are the highest and the peak load increases with increase in volume fraction of fibers and also with increase in the aspect ratio. In case of short fibers, with an increase in volume fraction of fibers from 0.5% to 1.0% the peak load increases by as much as 60%. In case of long

fibers, on an average a 15% increase in peak load can be observed with an increase in the volume fraction of fibers from 0.5% to 1.0%. The peak loads for 65/35-1.0% and 80/60-1.0% mixtures seem to be really close, but it can be seen from Figures 3.5 and 3.7 that the end load at a CMOD of 10mm is almost 75%-100% higher in case of 80/60-1% mixture when compared to the 65/35-1.0% mixture.

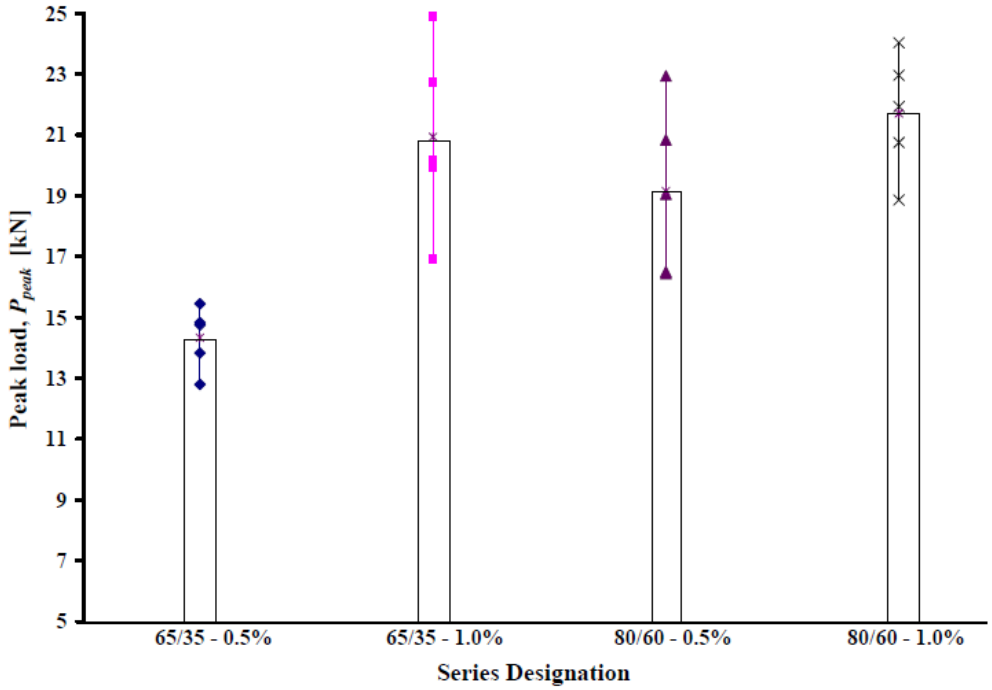

Figure 3.7: Peak loads for three point bending tests.

3.4.2 Parameters for the Determination of Stress-Crack Opening Relationship

Limit of Proportionality, $f_{fct,L}$

Figure 3.8, shows the trend for limit of proportionality, $f_{fct,L}$ for all the specimens tested. It can be clearly seen that in case of short fibers, as the volume fraction of fibers increases from 0.5% to 1.0%, $f_{fct,L}$ increases considerably. Also, there is an increase in $f_{fct,L}$ if long fibers are used instead of short fibers, although this increase in $f_{fct,L,}$ is not as comparable to the increase in case of volume fraction of

fibers for short fibers. Another interesting observation would be that there is no distinct change in $f_{fct,L}$ with the increase in volume fraction of fibers in case of long fibers. So it can be concluded from this plot that long fibers with higher percentages of volume fractions (beyond 0.5%) do not contribute to the peak load.

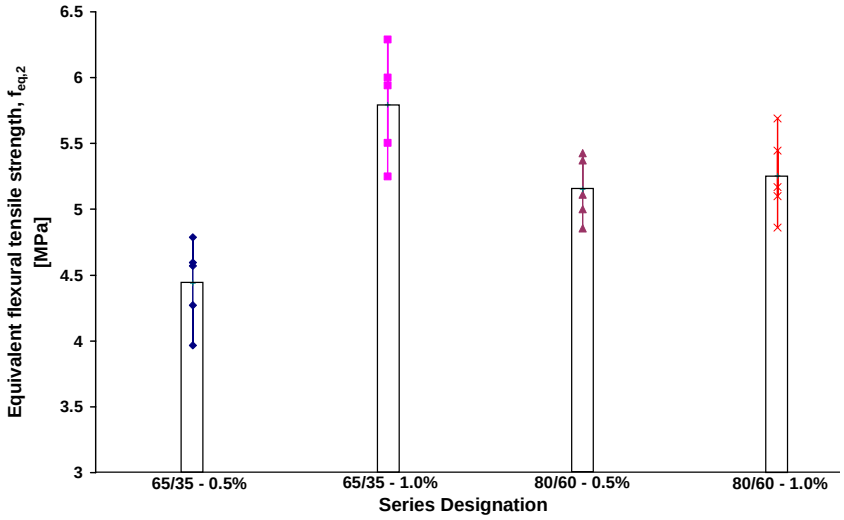

Figure 3.8: Trend showing effect of fiber type and volume fraction of fibers on limit of proportionality.

Table 3.5: Test results for all specimens tested.

Concrete Type	f_c [MPa]	f_t [MPa]	F_L [kN]	P_{peak} [kN]	δ_L [mm]	$f_{fct,L}$ [MPa]	$f_{eq,2}$ [MPa]	$f_{eq,3}$ [MPa]	$f_{R,1}$ [MPa]	$f_{R,4}$ [MPa]
	28.23	3.00	13.78	15.45	0.06	4.27	3.45	3.64	3.59	3.32
	27.68	3.22	12.80	14.75	0.06	3.97	3.02	2.85	3.18	2.42
65/35-0.5%	27.60		14.83	14.83	0.06	4.60	3.21	3.06	3.52	2.57
	-		15.45	13.83	0.07	4.79	4.33	3.93	4.42	3.18
	-		14.75	12.80	0.05	4.57	3.42	3.32		
	30.50	2.42	17.75	24.90	0.04	5.50	6.11	5.70	6.11	4.79
	29.14	3.15	20.29	22.74	0.10	6.29	7.27	6.27	6.97	4.76
65/35-1.0%	27.26	2.78	19.16	20.18	0.09	5.94	5.94	5.69	5.95	4.77
	-		19.35	19.93	0.10	6.00	7.85	7.30	7.34	6.17
	-		16.93	16.93	0.06	5.25	4.77	4.45	4.83	3.58
	36.22	3.65	15.66	22.94	0.07	4.86	4.41	4.86	4.55	4.76
	36.32	3.74	16.13	20.84	0.09	5.00	6.95	6.43	6.42	5.64
80/60-0.5%	34.20		17.33	19.05	0.05	5.37	5.49	6.16	5.70	5.83
	-		17.51	16.44	0.06	5.43	5.70	5.65	5.31	5.33
	-		16.48	16.50	0.06	5.11	4.07	4.28	4.31	3.98
	29.55	5.06	15.68	24.03	0.07	4.86	5.81	5.46	5.65	5.02
	26.55	4.03	16.68	22.96	0.09	5.17	7.10	6.63	6.57	6.17
80/60-1.0%	-		17.57	21.93	0.10	5.45	7.05	7.25	6.95	6.75
	-		16.45	20.75	0.09	5.10	5.49	5.95	6.00	5.65
	-		18.35	18.86	0.12	5.69	7.80	7.06	7.07	6.14

Relationship between $f_{eq,2}$ and $f_{eq,3}$

Figures 3.9 and 3.10 show the trend for $f_{eq,2}$ and $f_{eq,3}$ for all the specimens tested.

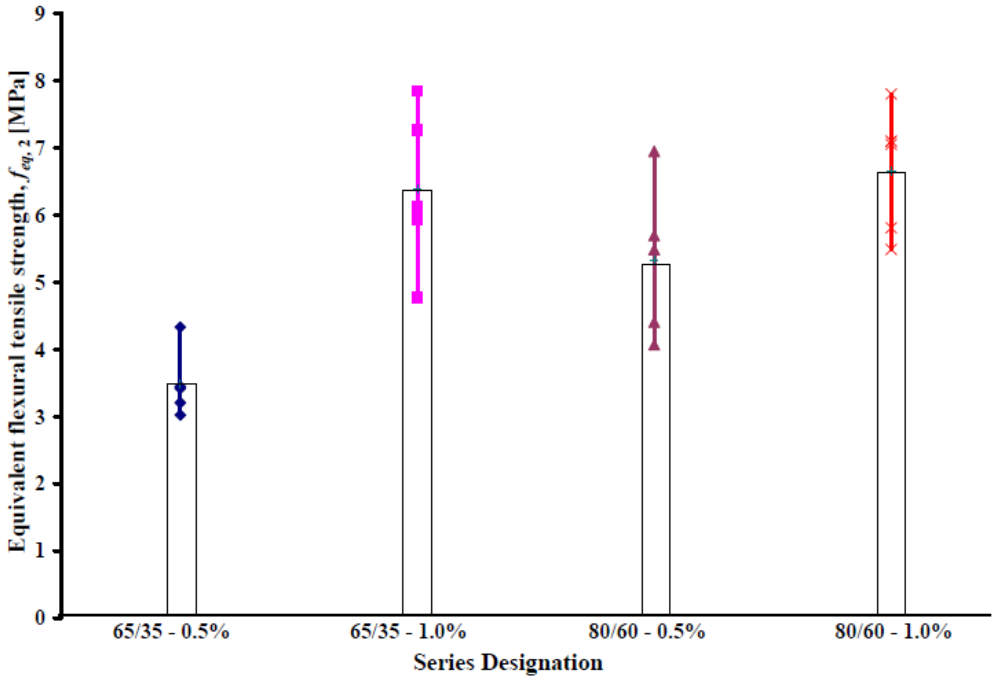

Figure 3.9: Trend showing effect of fiber type and volume fraction of fibers on equivalent flexural tensile strength, $f_{eq,2}$.

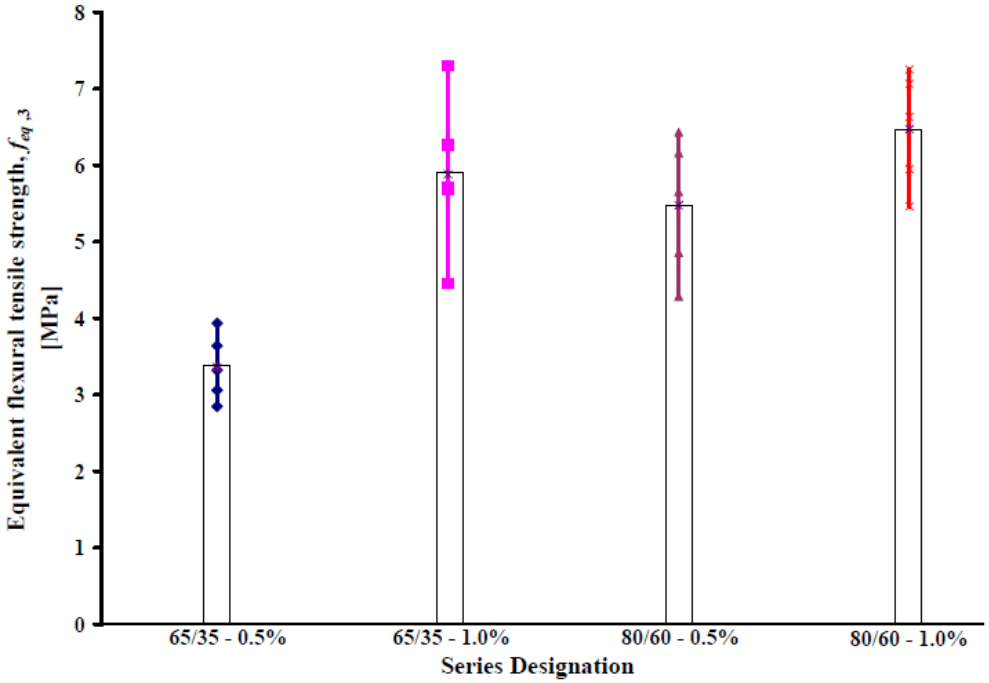

Figure 3.10: Trend showing effect of fiber type and volume fraction of fibers on equivalent flexural tensile strength, $f_{eq,3}$.

From Figures 3.9 and 3.10 it can be clearly seen that there is a considerable increase in the equivalent flexural tensile strength with an increase in the volume fraction of fibers. The percentage of increase is higher in case of short fibers than in the long fibers. In case of short fibers, $f_{eq,2}$ increases by as much as 95% when the volume fraction of fibers is increased from 0.5% to 1.0%. There is also an increase in as much as 100% in f_{eq2} when long fibers are used instead of the short fibers with a volume fraction of 0.5%. When the volume fraction of fibers in case of long fibers is increased from 0.5% to 1.0%, the increase in f_{eq2} is only 10-14%. It can be seen that $f_{eq,3}$ follows the same trend as observed for $f_{eq,2}$.

Figure 3.11 shows the ratio of $f_{eq,3}$ and $f_{eq,2}$ for the different mixtures and it can seen that this ratio almost remains the same for different mixtures and this explains the same trend observed in both the cases.

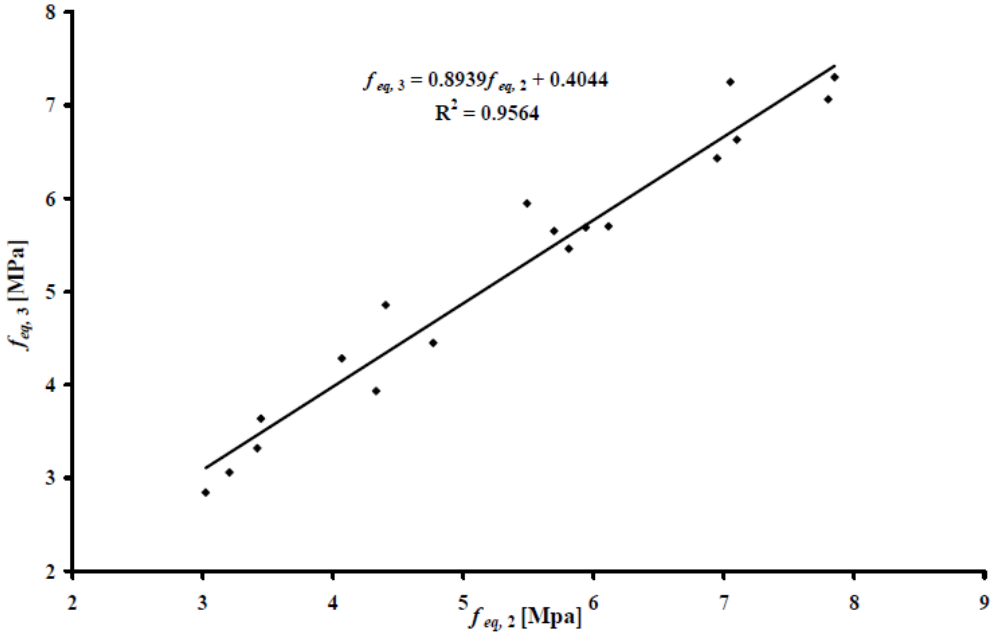

Figure 3.11: Plot showing the relationship between $f_{eq,2}$ and $f_{eq,3}$.

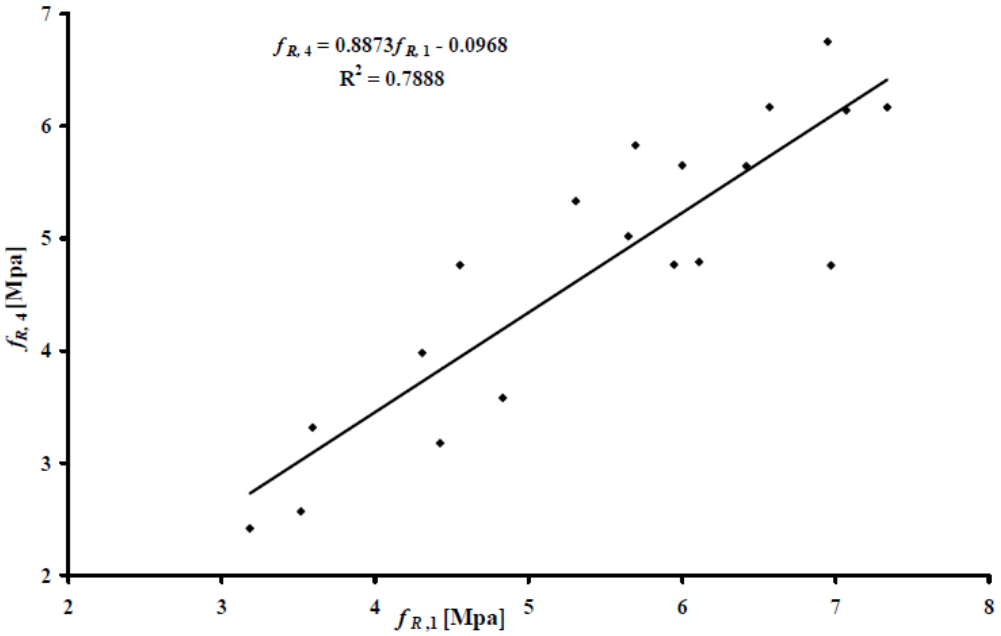

Figure 3.12: Plot showing the relationship between $f_{R,1}$ and $f_{R,4}$.

Figures 3.11 and 3.12, show the relationship between the equivalent flexural strengths $f_{eq,2}$ and $f_{eq,3}$ and between the residual flexural strengths $f_{R,1}$ and $f_{R,4}$. The slope of the lines 0.894 and 0.887 represent the ratio of the stresses at a CMOD/deflection of 0.5 mm/0.7 mm and 3.5 mm/2.70 mm. The high ratios of 0.894 and 0.887 shows that at a CMOD/deflection of 3.5 mm/ 2.70 mm the concrete still retains almost 90 % of the observed capacity at a CMOD/deflection of 0.5 mm/0.7 mm. These relationships show the extent to which the energy absorption capacity of the concrete is retained as the deflection/CMOD increases. It can be seen from these two figures that although the ratio of the strengths is almost the same (0.894 and 0.887), the scatter in the $f_{R,1} - f_{R,4}$ relationship is higher compared to the scatter in $f_{eq,2}$ - $f_{eq,3}$ relationship. This indicates that the f_R parameters are more susceptible to local irregularities of F-δ curve, as also observed by some other researchers (Barros et al, 2005). This could be due to the fact that the equivalent strengths are calculated by dividing the area under the load-deflection curve until a particular deflection with the deflection at that point,

to obtain the equivalent force at that deflection. Therefore, in the calculation of equivalent strengths, even if any irregularities exist at the start of the post peak region, the effect is averaged out due to the inherent procedure involved in calculating these quantities. But in case of the residual strengths, $f_{R,i}$, the load at individual CMOD's are observed and then used to calculate the strengths, which could be the reason for higher variability in the data.

RILEM TC 162-TDF (RILEM, 2002b) proposes analytical formulae, described in Figure 3.10, to model the uniaxial behavior of SFRC. The stresses at various points on the σ-ε shown in Figure 3.13 are expressed as a function of the residual flexural strengths $f_{R,1}$ and $f_{R,4}$. As shown earlier the f_R parameters are more susceptible to local irregularities of the P-δ curve, so it is better to express the stresses as a function of the equivalent flexural tensile strengths, $f_{eq,2}$ and $f_{eq,3}$, which have a less scatter in the calculated values.

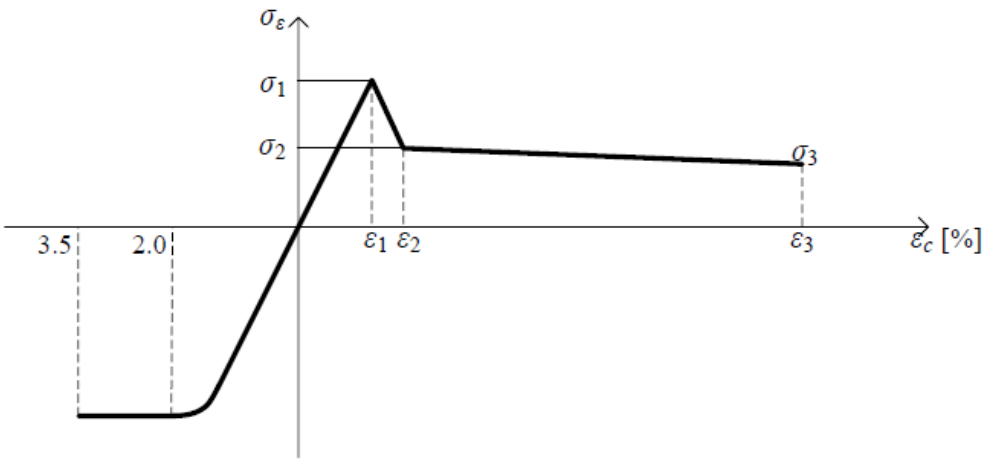

Figure 3.13: σ-ε diagram for SFRC, according to RILEM TC 162-TDF

3.4.3 *Residual Strength per ASTM C1609*

ACI 318 - 08 specifies that steel fiber reinforced concrete shall be acceptable to withstand shear loads in beam elements if conditions (a), (b) and (c) are satisfied:

a) The weight of deformed steel fibers per cubic yard of concrete is greater than or equal to 100 lb (45 kg).
b) The residual strength obtained from flexural testing in accordance with ASTM C1609 at a midspan deflection of 1/300 of the span length (f_{300}) is greater than or equal to 90 % of the measured first peak strength (f_1) obtained from a flexural test; and
c) The residual strength obtained from flexural testing in accordance with ASTM C1609 at a midspan deflection of 1/150 of the span length (f_{150}) is greater than or equal to 75 % of the measured first peak strength (f_1) obtained from a flexural test.

As per the above conditions, only mixtures 80/60 – 1.0% and 65/35 – 1.0% can be considered for shear design, see Table 4.1. The residual strengths f_{300} and f_{150} are calculated, for the above mentioned mixtures, as explained earlier in Section 2.5. In case of the specimens with the P-δ curves containing no first peak loads, the first peak load is considered as the load at a deflection of 0.05 mm. Table 3.6 shows the first peak strength and the residual strengths.

Table 3.6: First-peak and residual strengths per ASTM C1609.

Specimen	P_p	f_p	P_{300}	f_{300}	$0.9*f_p$	P_{150}	f_{150}	$0.75*f_p$
	kN	MPa	kN	MPa	MPa	kN	MPa	MPa
1	17.0	2.44	19.58	2.81	2.19	16.10	2.31	1.83
2	17.8	2.55	18.70	2.68	2.29	13.94	2.00	1.91
3	16.9	2.43	14.41	2.07	2.19	10.57	1.52	1.82
4	17.1	2.45	23.34	3.35	2.21	18.61	2.67	1.84
5	17.5	2.51	18.60	2.67	2.26	13.78	1.98	1.88
1	14.5	2.09	22.34	3.21	1.88	20.36	2.92	1.57
2	15.4	2.21	19.58	2.81	1.99	17.17	2.46	1.65
3	13.9	1.99	23.99	3.44	1.79	21.30	3.06	1.50
4	13.6	1.95	21.13	3.03	1.75	18.63	2.67	1.46
5	14.3	2.06	17.58	2.52	1.85	14.60	2.10	1.54

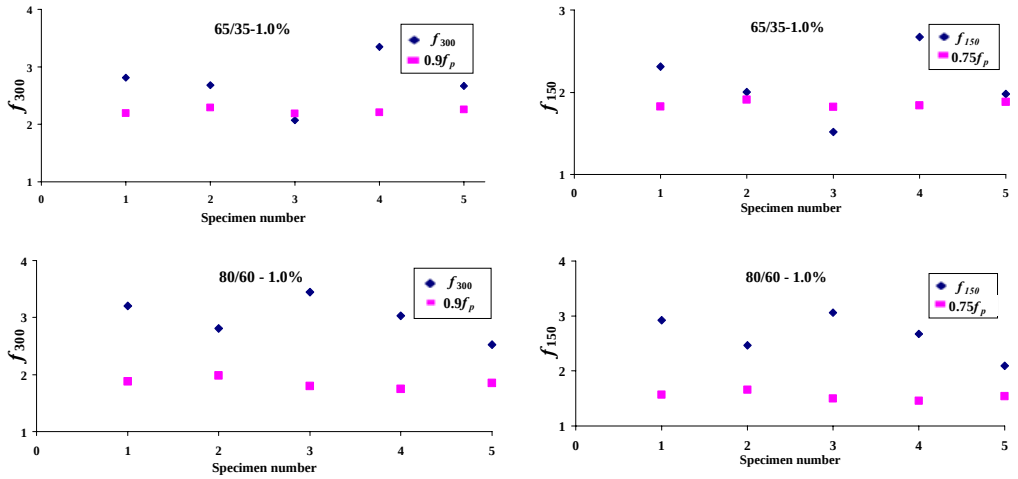

Figure 3.14: Residual strengths per ASTM C1609.

Figure 3.14 shows the residual strengths calculated per ASTM C1609 and also a comparison of these residual strengths with the 90% and 75% of the first-peak strength. Since the residual strengths f_{300} and f_{150} are greater than 90% and 75% of the first-peak strength respectively, the concrete mixtures 80/60 – 1.0% and 65/35 – 1.0% are considered acceptable for shear resistance according to ACI 318-08.

Chapter 4 Inverse Analysis

4.1 Introduction

Roelfstra and Wittmann (1986) were the first to propose inverse analysis to determine the tension softening diagram for concrete. The algorithm developed could only be used for bilinear-type softening diagrams and required the first guess of the input parameters to be close to the iteration results. Stang and Olesen (1998) developed the cracked hinge model, based on the work done by Ulfkjaer (1995). Ostergaard (2003) developed an algorithm for inverse analysis based on the cracked hinge model and incorporated it into a Matlab program. In this program a step wise (multi-step) inverse analysis was performed to obtain the complete σ-w curve. Although a step wise analysis was performed, the values obtained in this program require an initial guess and optimization should be run more than once to obtain at the exact result.

Sousa and Gettu (2006) suggested the use of weighing factors in the optimization process in case of long range of crack widths (0 – 2.0 mm). Even in this case the predicted tensile strength had a lot of variability and was not accurate. The minimum range of CMOD to be recorded in the experiments and the effect of this range on the obtained σ-w curve in the inverse analysis is still unclear from the literature.

As part of this study, an algorithm was developed to obtain the softening curve of FRC, bilinear σ-w curve, which can accurately depict the entire range of the used

P-CMOD curve. A study was also done on the effect of the range of CMOD used in the inverse analysis on the obtained σ-w curves.

4.2 Algorithm for Inverse Analysis

Using the analytical expressions and the cracked hinge model explained in Section 2.5, a step wise inverse analysis algorithm was developed to obtain the σ-w curve given the *P*-CMOD curve for concrete. In this algorithm the normalized hinge deformation, θ, introduced earlier in Eq. 2-16c, was incremented in small intervals to calculate the load, *P*, and crack mouth opening displacement, CMOD using Eqs. 2.29 and 2.30 respectively. The predicted and the experimentally obtained *P*-CMOD curves can be compared by comparing the load, *P* at different CMOD levels. If (P_{exp}, CMOD_{exp}) and (P_{pre}, CMOD_{pre}) denote the set of all points defining the experimental and the predicted curves respectively, P_{exp} and P_{pre} can be compared only at points where $\text{CMOD}_{\text{exp}} = \text{CMOD}_{\text{pre}}$. The accuracy of the comparison of the experimental and the predicted *P*-CMOD curves increases with an increase in the number of points where $\text{CMOD}_{\text{exp}} = \text{CMOD}_{\text{pre}}$. The 3PB tests were conducted under displacement control and the test data was collected at regular intervals of time. The observed test data was recorded at equal intervals of deflection and therefore the load, *P*, need not necessarily be recorded at regular intervals of CMOD. As explained earlier, the accuracy of the comparison of the experimental and predicted *P*-CMOD curves depends on the number of points of comparison. Therefore, to increase the number of comparison points, the experimentally obtained load, P_{exp} was linearly interpolated on the P_{exp}-CMOD_{exp} curve at regular intervals of 0.001 mm of CMOD_{exp} and the predicted load-CMOD curve, P_{pre}-CMOD_{pre}, was obtained such that CMOD_{pre} is equally spaced at 0.001 mm. By linearly interpolating the P_{exp}–CMOD_{exp} curve, the comparison

is a lot simpler since the load, P, can be compared at all points on the interpolated P_{exp} – CMOD_{exp} and the P_{pre} – CMOD_{pre} curve. The equal spacing of CMOD also helps in the optimization process, since in this process the error between the predicted and the experimentally obtained curves is found by finding the difference in the load, P, values at all the CMOD values and by changing the σ–w curve parameters such that the error is minimized.

From Eqs. 2.17 – 2.20, it can be observed that:

1. In the elastic phase (Phase 0) the P –CMOD curve is completely governed by the physical member properties of the specimen and the modulus of elasticity, E of the concrete., see Figure 4.1 and Eq. 2.17
2. The transition from the elastic phase to the fictitious crack phase or Phase I is governed by the modulus of elasticity E and the tensile strength of concrete $f_{t.}$ The shape of the P-CMOD curve in the next phase of crack propagation, Phase I and the first peak of the P-CMOD curve, as shown later in Section 4.2.2, is governed by E, f_t and the slope of the initial part of the softening curve (σ-w curve), $a_{1,}$ see Figure 4.1 and Eq. 2.18

3. The transition between the Phase I and the Phase II of the crack propagation and the shape of the P-CMOD in the Phase II of the crack propagation is governed by the second portion of the softening curve (a_2, b_2), see Figure 4.1 and Eq. 2.19

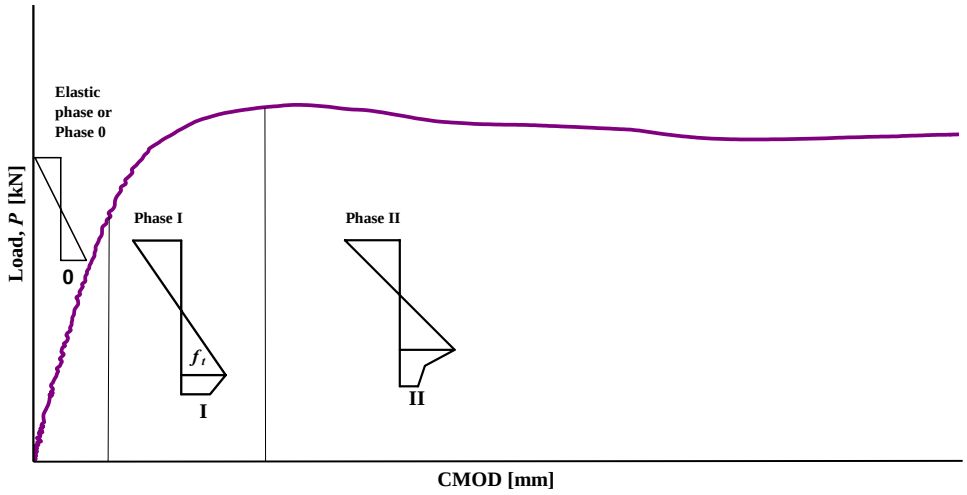

Figure 4.1: Typical load-CMOD curve showing the phases of crack propagation and the corresponding stress distribution.

From the above observations it can be noted that different material properties govern different portions of the *P*-CMOD curve. So as the CMOD increases, the *P*-CMOD curve is first governed exclusively by modulus of elasticity *E*, then by the properties f_t and a_1. As the CMOD further increases, the shape of the curve is then dictated by the properties a_2 and b_2. Therefore, if a similar procedure is followed by calculating for these properties exclusively in the region of their influence then these properties can be determined accurately.

Therefore, the proposed optimization algorithm:

1. Calculates modulus of elasticity, *E,* by performing the optimization only in the elastic portion of the *P*-CMOD curve.
2. Since the initial portion of the curve is governed by *E*, which is already known, the tensile strength of concrete f_t and a_1 are calculated by performing the optimization in the CMOD interval of 0 – 0.05 mm.

3. The parameters a_2 and b_2 are then obtained by performing the optimization process on the whole *P*-CMOD curve since the Phase 0 and Phase I portions of the curve are already established by calculating E, f_t and a_1.

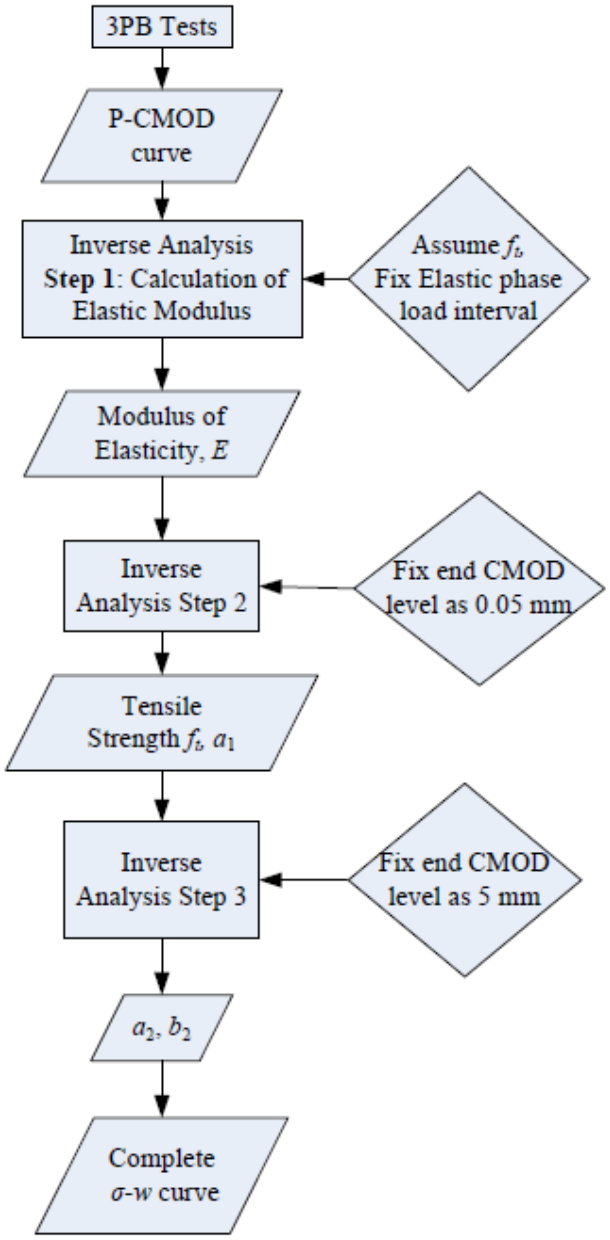

Figure 4.2: Flowchart of the proposed optimization algorithm.

4.2.1 Calculation of the Elastic Modulus

The modulus of elasticity for concrete is found by considering the linear portion of *P*-CMOD curve. For plain concrete, ACI 446 suggests to consider the load range of 15% to 55% of the peak load. In concrete mixtures with high volume fraction of fibers, deflection hardening is observed and the upper bound of 55% of peak load might fall in the non-linear range of *P*-CMOD curve and therefore, the load range suggested by ACI 446 cannot be used. To avoid this problem this study suggests that the user should choose an appropriate linear range of *P*-CMOD curve, by observation, for the determination of elastic modulus. As explained in the algorithm, the modulus of elasticity is calculated by performing a least squares curve fitting on the analytically calculated *P*-CMOD curve in the linear range. In this particular case a range of 2 – 6 kN was found to be in the linear region. Figure 4.3 shows the analytically calculated and the experimentally recorded *P*-CMOD curves for a randomly chosen specimen. Figure 4.3 shows a close match between the analytical curve and the experimental data. Plots showing a comparison of the experimental and the analytical *P*-CMOD curves in the linear range for all the specimens are presented in Appendix B.

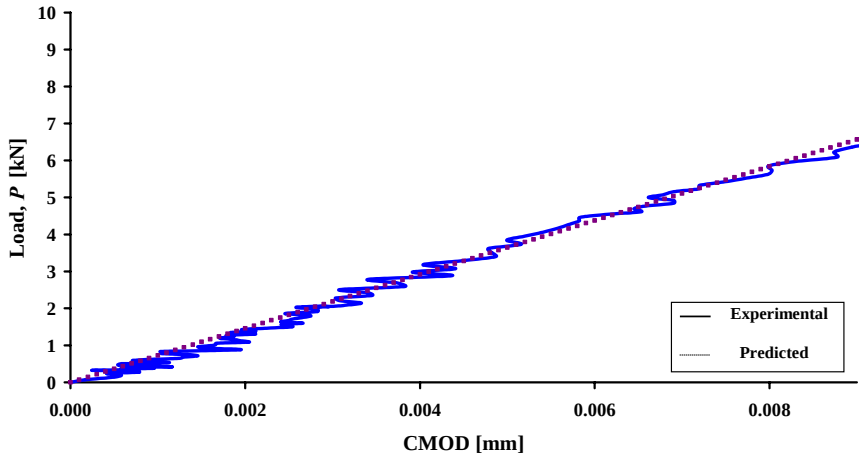

Figure 4.3: Comparison of experimental and analytical *P*-CMOD curves for elastic modulus.

In the developed algorithm, both the load, P, and the CMOD are linearly dependant on the tensile strength f_t in the elastic phase (Phase 0), as shown in Eqs 2.29 and 2.30 and so, the slope of the P-CMOD curve is independent of f_t. Therefore, the determination of modulus of elasticity, E, although requires an initial guess of the tensile strength f_t, does not depend on the initial estimate of the tensile strength, f_t. This avoids the need to run multiple optimizations to find the modulus of elasticity, E.

4.2.2 Calculation of Tensile Strength (f_t) and a_1

The terms f_t and a_1 are calculated considering only the part which is most influenced by these terms. Eqs 2.18 and 2.19 show that a_1 contributes to the P-CMOD only during Phase I and (a_2, b_2) govern Phase II and III. f_t and a_1 also affect the point of transition from Phase I to Phase II, as shown in Eq. 2.21b.

Figures 4.4 – 4.6 show the plots of normalized moment, μ vs. normalized curvature, θ. These plots are shown for a θ value of 0 – 10. θ, from Eq. 2.15, is the normalized curvature of the concrete section and has a value of 1 when the concrete section starts to crack. Therefore, a θ value of 10 would imply that the concrete section is experiencing 10 times the curvature at the point of crack initiation and by which point the crack propagation would already be in Phase II. Normalized moment, μ, is defined in Eq. 2.16a and has a value of 1 when the crack propagation starts and is equal to normalized curvature, θ, in the elastic phase, see Eq. 2.17b. From Eq. 2.29, for a fixed value of E, f_t and a_1, CMOD is directly proportional to θ and vice versa. Therefore, an increase in θ can be interchangeably represented as an increase in CMOD and the following conclusions are true for an increase in θ or CMOD. The following plots are drawn by varying E, f_t and a_1 respectively. Some of the observations from these plots are:

- $\mu(\theta)$ increases with CMOD till a certain peak value is reached and then starts to decrease and this decrease in $\mu(\theta)$ continues as the CMOD further increases.
- The curve remains convex for the entire range of θ.

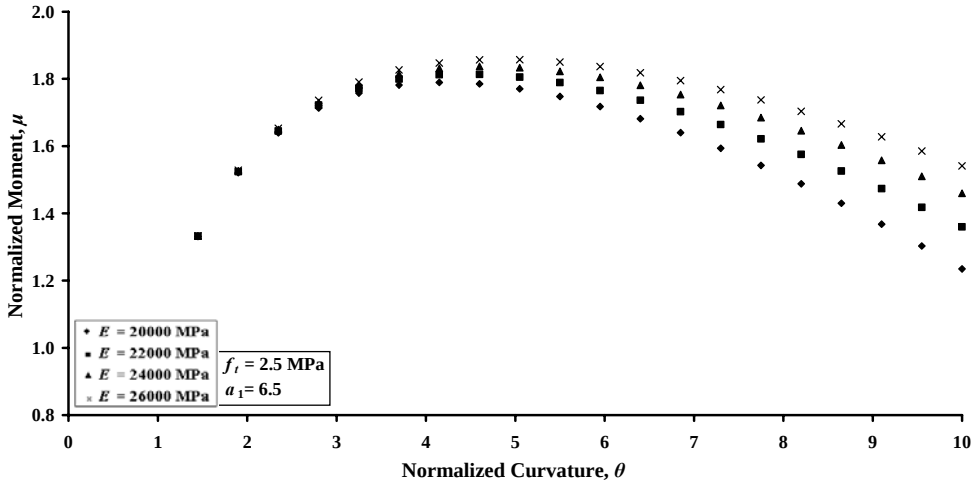

Figure 4.4: Variation of normalized moment, μ, as a function of normalized curvature, θ, for different E.

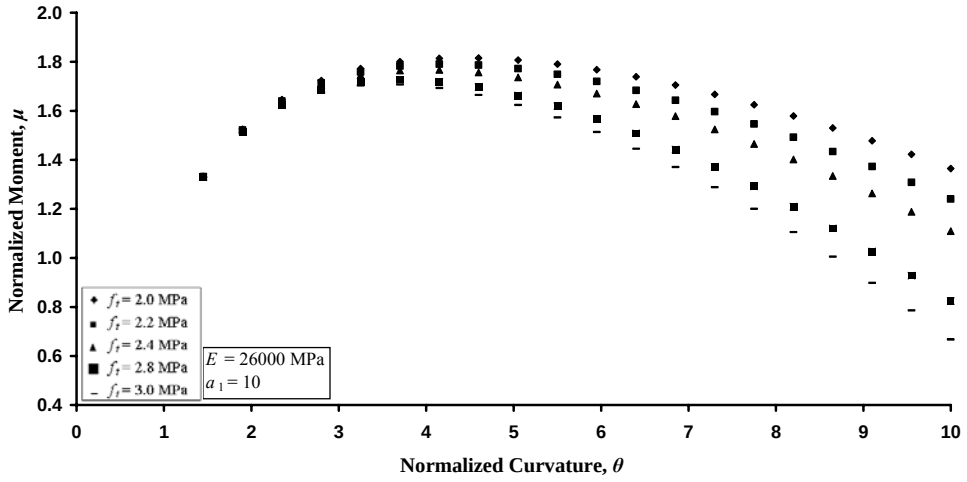

Figure 4.5: Variation of normalized moment, μ, as a function of normalized curvature, θ, for different f_t

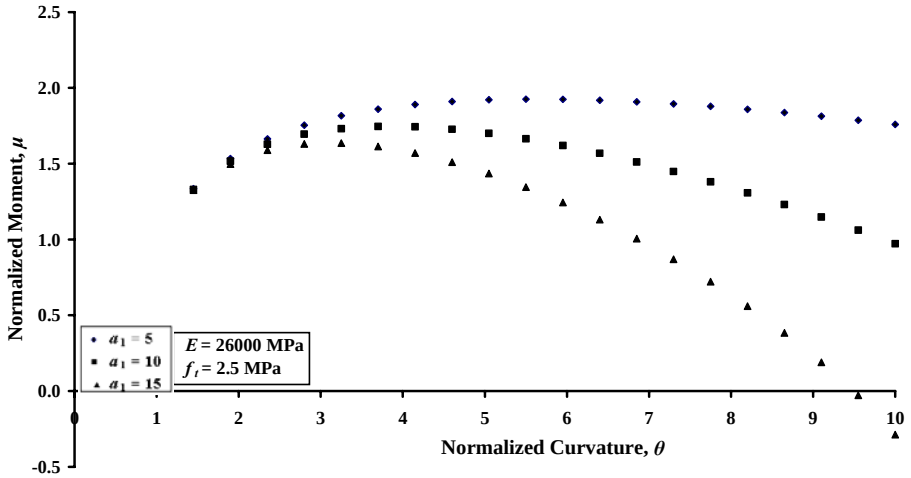

Figure 4.6: Variation of normalized moment, μ, as a function of normalized curvature, θ, for different a_1

In contrast to these plots, the *P*-CMOD curves, shown in Fig 4.7, exhibit concave behavior after reaching the first peak. After the first peak, depending on the volume and the type of fibers, the *P*-CMOD curve either continues to decrease or increases to form another peak. In either of the above situations the curve changes its initial convex nature after the initial peak. Therefore it can be guessed that the *P*-CMOD curve enters Phase II after the first peak.

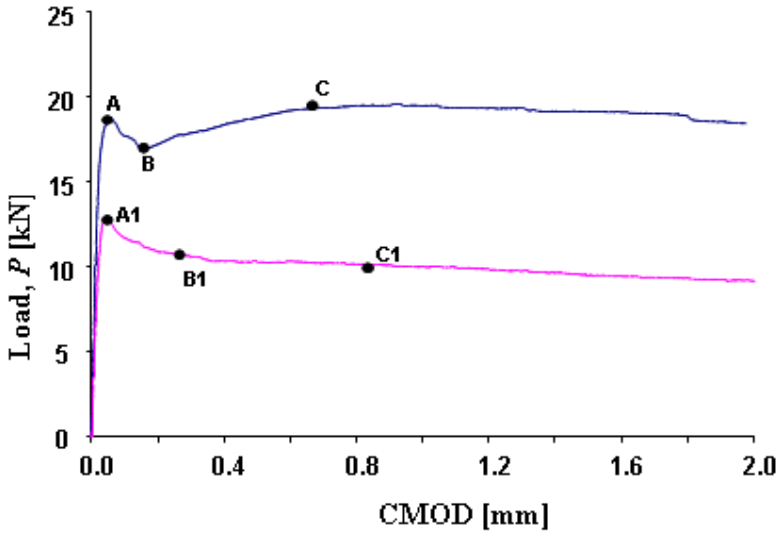

Figure 4.7: Typical experimental *P* – CMOD curves.

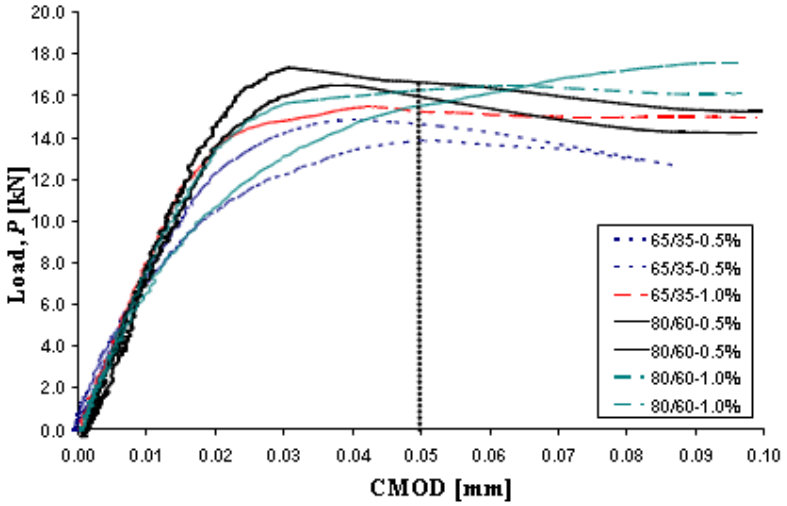

Figure 4.8: Plot showing the initial portion of the *P*-CMOD curves for some of tested specimens.

Figure 4.8 shows the *P*–CMOD curves for different fiber geometries and fiber volumes. It is clear that the first peak occurs at a CMOD ≤ 0.05 mm except in curves where the load, *P*, continues to increase with out any initial drop, which occurs in concrete with high fiber concentrations. From preliminary optimization runs it was observed that Phase I ends around a CMOD of 0.05 mm and this observation is also later confirmed after obtaining the final σ-w curves. If the optimization is performed on the whole range of CMOD, say 0 – 5 mm, then the number of data points that lie outside the actual range of interest is far higher than the number of data points in the Phase I region. Assuming a CMOD spacing of 0.001mm, there would be a mere 50 points lying in a CMOD range of 0 – 0.05 mm compared to the 4950 points lying in the CMOD range 0.05 – 5.0 mm range which lie outside Phase I. This results in spurious results for the parameters f_t and a_1.

Sousa and Gettu (2006) used a weighting factor, to give more importance to a particular range of CMOD when compared to others, in the optimization process.

It was also concluded by Sousa and Gettu (2006) that, when a higher weight is used for the initial part (near the first peak) of the P – CMOD curve a better fit of the peak load is obtained while equal weighting of all the regimes leads to a better fit of the latter regimes.

To calculate f_t and a_1, the current study proposes an optimization interval of 0 – 0.05 mm. By restricting the optimization interval to 0 – 0.05 mm, the existing algorithm is having the same effect as giving a higher weighting factor to initial part of the P – CMOD curve as done by Sousa and Gettu (2006).

Therefore in the existing algorithm f_t and a_1 are obtained by performing the optimization process in the interval 0 – 0.05 mm and the algorithm reads as:

$$\min_{(f_t, a_1)} \sum_{0}^{0.05} \left(P_{\exp} - P_{pre} \right)^2 \qquad \text{Eq. 4.1}$$

subject to $\beta_1 < 1$.

In the current step, the optimization is performed in a CMOD interval of [0, 0.05 mm], but since Phase I lies around the region of first peak a higher weight should be given to these values of load. Therefore, the objective function shown in Eq. 4.1, which gives more weight to higher values of P is chosen for the optimization.

The proposed optimization procedure includes the step wise algorithm (Ostergaard, 2003) and also the merits of weighting (Sousa and Gettu, 2006), by performing the optimization for the σ – w curve parameters in their corresponding phases. Due to this advantage the proposed algorithm obtains a good fit of the curve for the whole range of CMOD. Figures 4.9 to 4.12 show the plots of the

experimental and the predicted *P*-CMOD curves near the peak load region. The thick lines represent the experimental data and thin lines represent the *P*-CMOD predicted using the proposed algorithm.

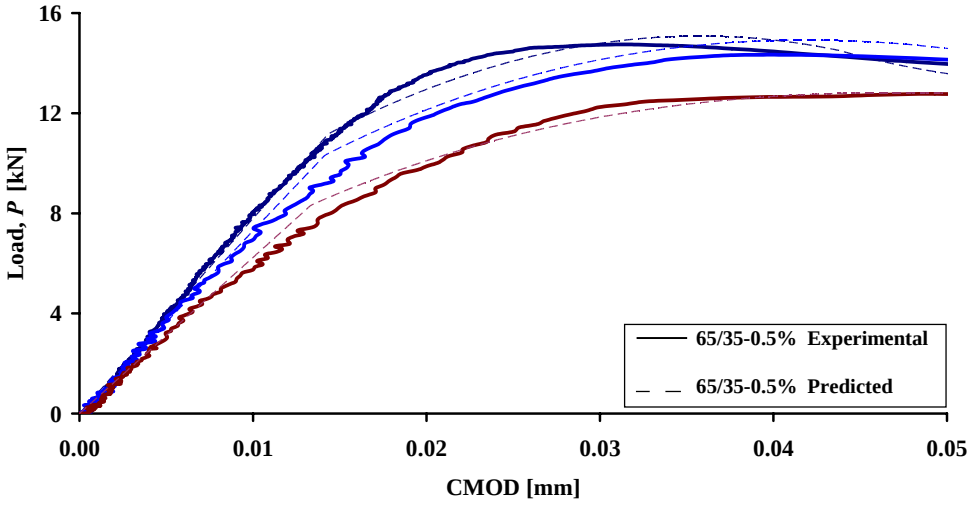

Figure 4.9: Plot showing experimental and predicted *P* – CMOD curve for 65/35 – 0.5% for a CMOD range of [0, 0.05 mm].

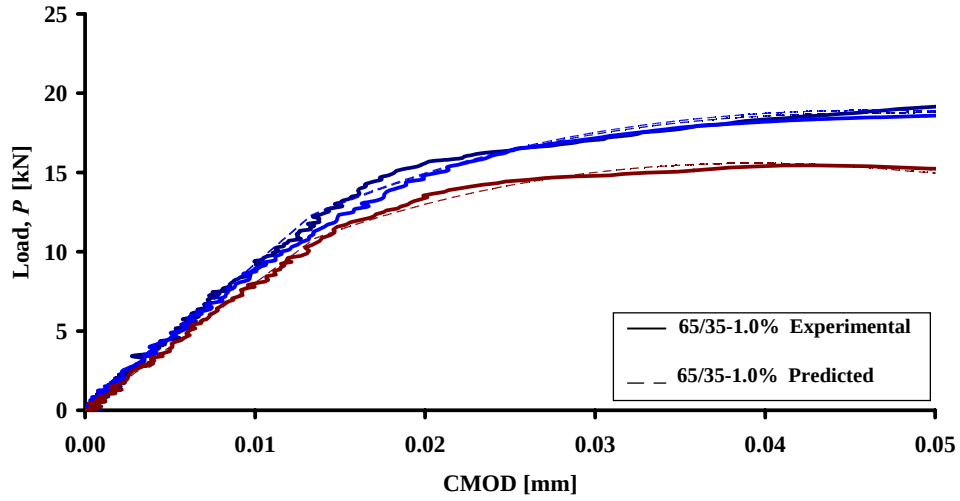

Figure 4.10: Plot showing experimental and predicted *P*-CMOD curve for 65/35 – 1.0% for a CMOD range of [0, 0.05 mm]..

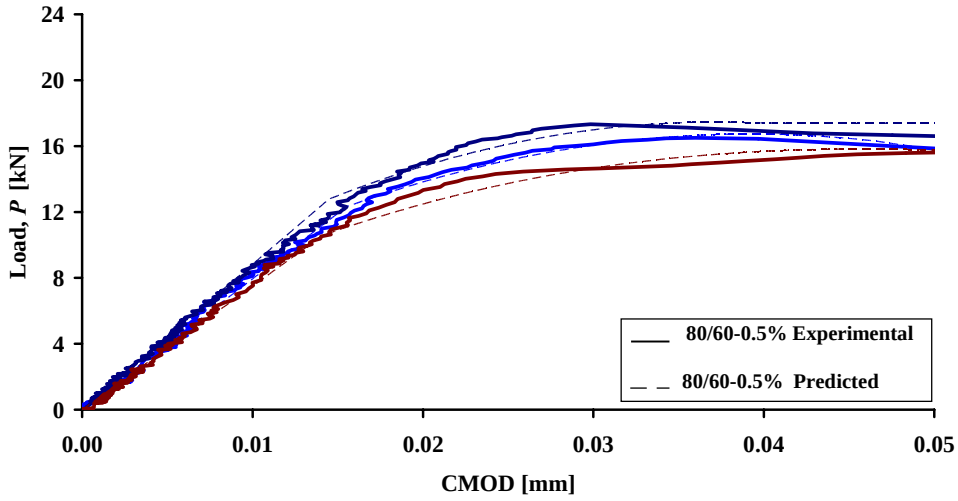

Figure 4.11: Plot showing experimental and predicted *P*-CMOD for 80/60 – 0.5% for a CMOD range of [0, 0.05 mm].

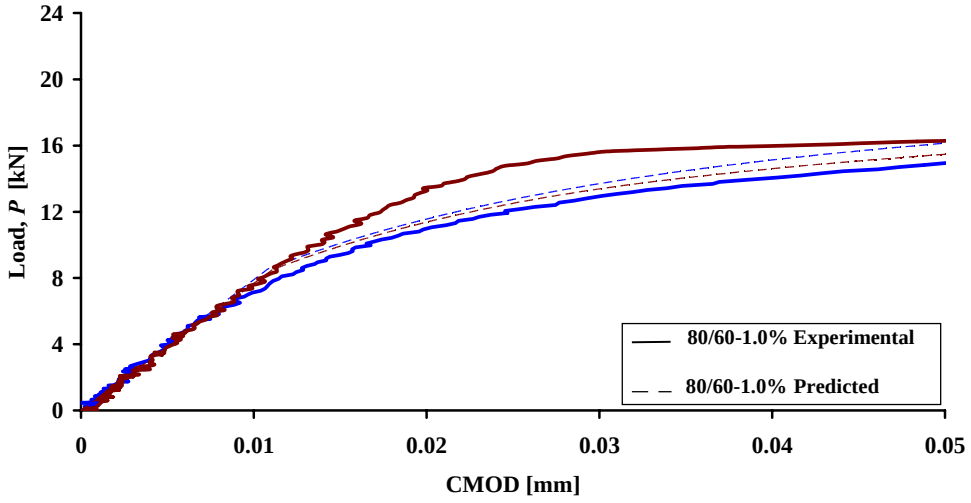

Figure 4.12: Plot showing experimental and predicted *P*-CMOD for 80/60 – 1.0% for a CMOD range of [0, 0.05 mm].

From the above discussion and also from the observed close fit in the experimental and analytically obtained curves it can be concluded that to calculate f_t and a_1 the optimization process should be restricted to a CMOD interval of 0 – 0.05 mm.

4.2.3 Calculation of a_2 and b_2

In Steps 1 and 2 the modulus of elasticity E, tensile strength f_t and a_1 are calculated. Step 3 involves calculation of a_2 and b_2 which characterizes the post peak portion of the curve. As already explained in Section 4.2, (a_2, b_2) govern the Phase II and Phase III part of the P-CMOD curve. But from preliminary optimization runs it was observed that value of $\theta_{I\text{-}II}$, the normalized moment at which the P-CMOD curve changes from Phase II to Phase III is always greater than 1000. Since $\theta = 1$ at the initiation of cracking, a value of $\theta = 1000$ would imply that the specimen should experience 1000 times the curvature that experienced at the point of crack initiation, which need not be considered for practical purposes. Therefore, for all practical purposes, the crack propagation can be assumed to remain in Phase II. To calculate a_2 and b_2 the assumed σ-w curve can be optimized over the whole P-CMOD curve obtained experimentally. The optimization can be run on the whole curve, instead of running it on the interval which excludes the 0 - 0.05 range. This can be done since E, f_t and a_1 are already known and therefore the linear phase (Phase 0) and Phase I are already fixed and are not influenced by the assumed or the calculated values of a_2 and b_2.

As in case of Step 2 an end level of CMOD has to be defined to specify the optimization interval. The end level for optimization interval can be taken as the maximum CMOD recorded experimentally. It has also been a point of interest of many researchers to identify an end level of CMOD until which the experiment has to be conducted and the P-CMOD data collected so that the $\sigma - w$ curve can be obtained without any loss of accuracy. It can be seen from any P-CMOD plot that the curve remains approximately a straight line at higher CMODs (> 2 mm).

Therefore, to predict the straight portion of the *P*-CMOD curve it would be enough to predict the exact slope of the end portion of the curve. To observe the effect of the end level of optimization interval on the predicted σ–w curve, the optimization was run over a range of CMOD intervals for all the different types of concrete mixtures and the variation in a_2 and b_2 studied.

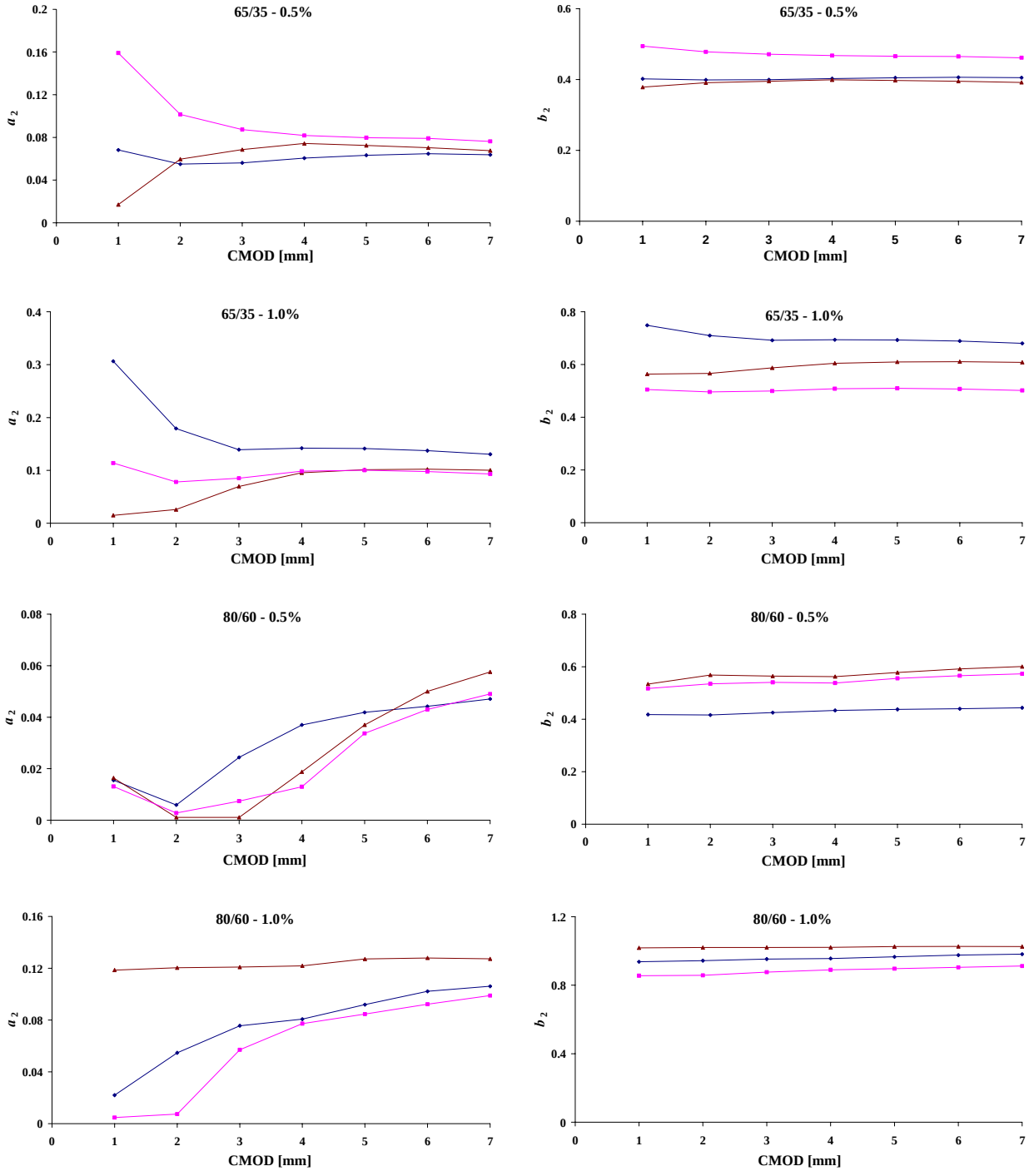

Figure 4.13: Effect of end level of CMOD on a_2 and b_2.

Fig. 4.13 shows the effect of fitting interval on the calculated material properties for the concrete mixtures used in this study. It can be seen that the calculated material properties change rapidly with a change in the optimization interval until the optimization interval is changed to 5 mm and then the material properties remain almost constant. The effect of fitting interval is more seen in case of higher fiber percentages. In these cases as the σ-w curve enters the second phase, the P-CMOD curve first suddenly drops, then increases and finally starts decreasing or in some cases as seen in case of 80/60 – 1.0% the P-CMOD curve continues to increase as it enters the second phase in the σ-w curve and then starts finally decreasing after reaching a peak load. The initial drop and then increase in the load (in some cases) and the subsequent decrease in the load after reaching the peak occurs in the CMOD range of 0.05 – 5 mm. Therefore if the optimization is run with the peak CMOD in this range then the error function is minimized only in this local region and the obtained material properties depict the local behavior but fail to depict the overall behavior of the material. It can also be explained by saying that when the end level of CMOD is less than 5 mm, the parameters are obtained by finding the local minima and not the global minima of the error function.

It can also be observed in Figure 4.13 that as the end level of CMOD changes the variation in a_2 is higher compared to the variation in b_2. Parameter b_2, which determines the tensile stress at the beginning of the second phase, remains almost unaffected as the end level of the CMOD changes. Parameter a_2, which defines the slope of Phase 2 of $\sigma - w$ curve, varies with the end level of CMOD and remains constant after an end level CMOD of 5 mm.

As in case of plain concrete and also as done by Sousa and Gettu (2006), if the CMOD is recorded only until 2 mm, from Figure. 4.13, the slope of Phase 2 of the $\sigma - w$ curve changes considerably.

Therefore, the range over which the optimization is run affects the material properties calculated and therefore it is proposed that the *P*-CMOD data should be experimentally captured at least until a CMOD of 5 mm. In the current optimization algorithm, the value of b_2, for the concrete mixture 80/60-1.0% is close to 1.0 and in some cases was higher than 1, when a least squares fitting was performed. A value of b_2 would imply that the material has strength higher than the tensile strength of the concrete. In the case of 80/60-1.0%, it could also be seen from the *P*-CMOD curves, the concrete mixture exhibits deflection hardening behavior and therefore there is no initial drop in the load. The initial descending branch of the σ-w curve would therefore be negligible and the curve would directly go into the second branch. Therefore, the value of b_2 would be really close to 1, but always less than 1. If a least square curve fitting is performed without any constraint on the value of b_2, the result would be a mathematically true, but not physically true. Therefore a constrained optimization is performed to obtain the values of a_2 and b_2 with a constraint of $b_2 \leq 1$.

Therefore in the existing algorithm a_2 and b_2 are obtained by performing the optimization process in the interval 0 – 5 mm and the algorithm reads as:

$$\min_{(a_2,b_2)} \sum_{0}^{0.05} \left(P_{\exp} - P_{pre}\right)^2 \qquad \text{Eq. 4.2}$$

subject to $b_2 \leq 1$.

Table 4.1: Parameters defining σ-w curve.

Concrete Type	E GPa	f_t MPa	a_1	a_2	b_2	w_1 mm
	23.95	3.41	29.69	0.064	0.4	0.0201
65/35 - 0.5%	22.43	3.15	21.31	0.068	0.39	0.0286
	19.18	2.54	16.06	0.076	0.46	0.0337
Average	**21.85**	**3.03**	**22.35**	**0.07**	**0.42**	**0.03**
	28.36	3.74	16.87	0.141	0.69	0.0183
65/35 - 1.0%	28.47	3.76	16.3	0.102	0.61	0.024
	24.69	3.31	22.96	0.098	0.51	0.0216
Average	**27.17**	**3.6**	**18.71**	**0.11**	**0.6**	**0.02**
	24.43	3.76	26.65	0.047	0.44	0.0209
80/60 - 0.5%	27.14	3.9	27.77	0.058	0.6	0.0144
	23.06	3.23	17.79	0.053	0.58	0.0237
Average	**24.88**	**3.63**	**24.07**	**0.05**	**0.54**	**0.02**
	24.29	2.61	6.51	0.102	0.98	0.0037
80/60 - 1.0%	25.78	2.63	8.12	0.126	1	0
	23.6	2.6	6.55	0.105	0.92	0.0122
Average	**24.56**	**2.61**	**7.06**	**0.11**	**0.97**	**0.01**

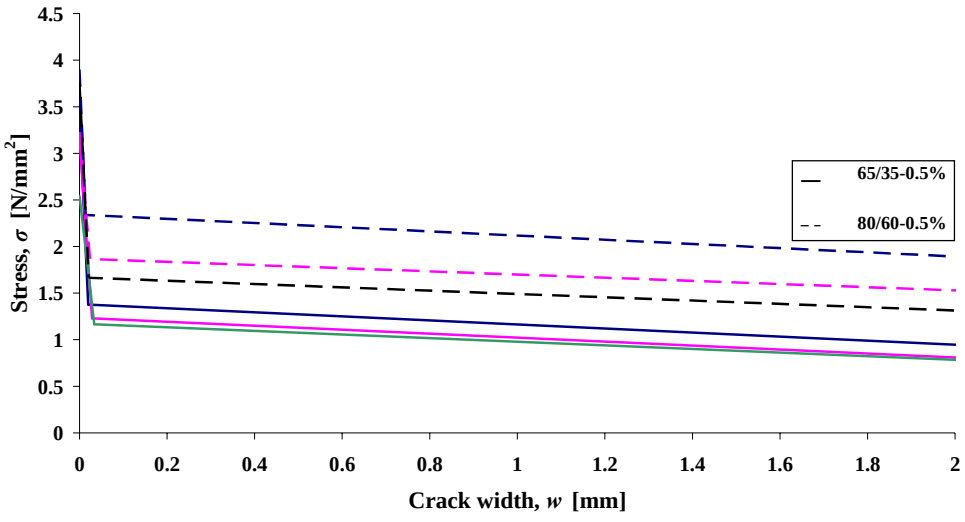

Figure 4.14: σ–w curves for concrete mixtures with 0.5% volume fraction of fibers.

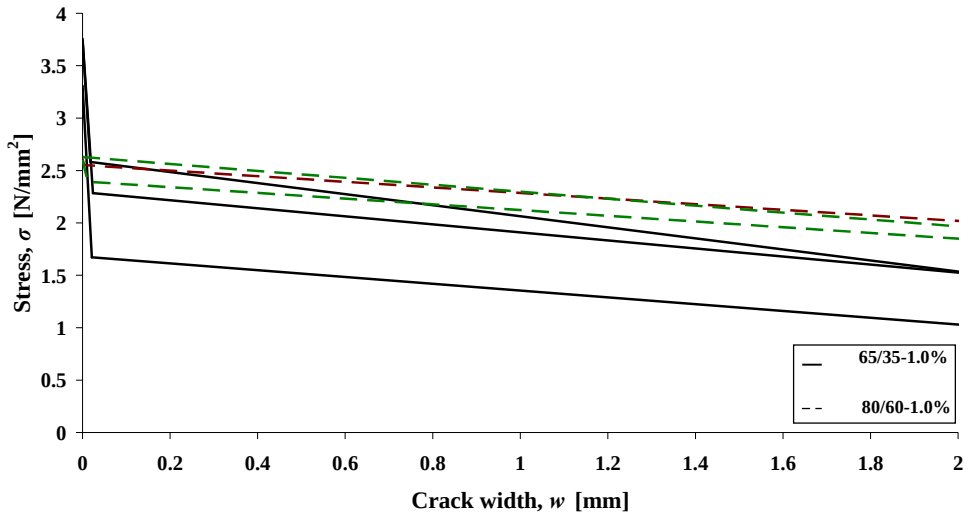

Figure 4.15: σ–w curves for concrete mixtures with 1.0% volume fraction of fibers.

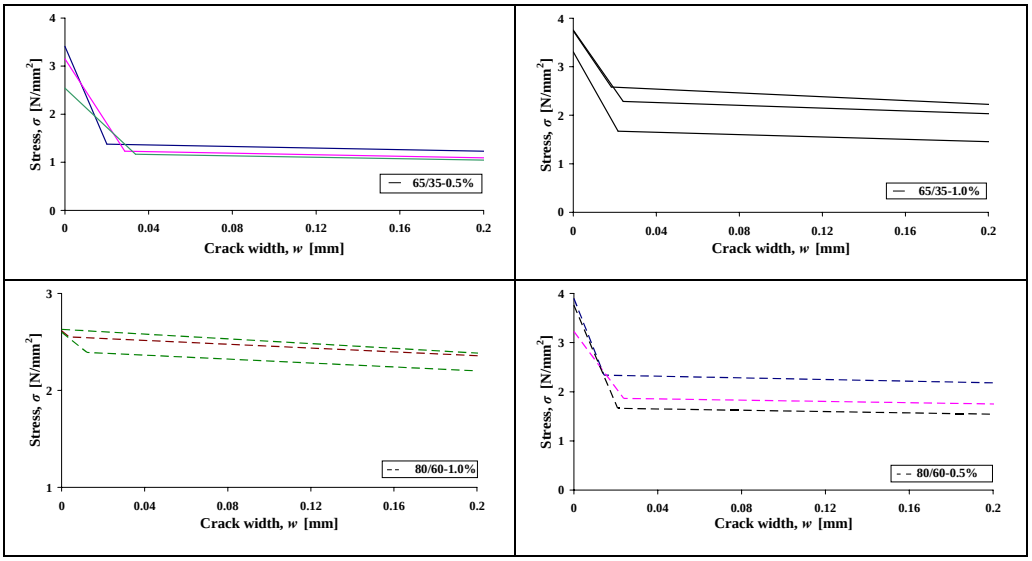

Figure 4.16: Plots showing the σ-w curves for a crack width range, w, of [0, 0.02 mm].

Table 4.1 gives the parameters defining the σ–w curves for all the types of concrete tested. This data can be compared to the σ-w curves currently presented in the literature for similar type of concrete mixtures, but is not done as part of the current study. It can be observed that the parameter a_2 which is the slope of the Phase 2 part of the σ–w curve is of the same order for both the 65/35 and 80/60 type of fibers at equal volume fractions. Figures 4.14 and 4.15 show the tensile strength normalized σ–w curves for both the 65/35 and 80/60 fiber concretes at

volume fractions of 0.5% and 1.0% respectively. It is clear that the Phase 2 curve of both 65/35 and 80/60 fiber concretes at equal volume fractions are parallel to each other. The slope of the Phase 2 curve is the parameter a_2 and therefore it concurs with the earlier observation about a_2 for different types of concrete.

From Table 4.1, the maximum value of w_1, which represents the end level of the crack width opening, is 0.0337 mm with an average value of 0.018 mm which is less than 1/100 of the final crack width opening calculated. Therefore, when the *P*-CMOD or the σ-*w* curve is considered over a long range of CMOD/*w,* then the σ-*w* curve can be simplified to a drop-linear curve as proposed by Olesen (2001) and Sousa and Gettu (2006). This simplification would have a big impact on the shape of the *P*-CMOD curve near the first peak, but can be neglected when the user is interested in the post-peak behavior of the material. This is useful for modeling purposes since fewer variables need to be input to model the softening curve of concrete.

Table 4.2: Comparison of experimental and predicted material properties.

	Predicted		**Experimental**	
Concrete Type	E **GPa**	f_t **MPa**	E **GPa**	f_t **MPa**
	24	3.4	20	3
	22	3.2	21	3.2
65/35 - 0.5%	19	2.5		
Average	**22**	**3**	**21**	**3.1**
	28	3.7	30	3.7
	28	3.8	30	3.7
65/35 - 1.0%	25	3.3		
Average	**27**	**3.6**	**30**	**3.7**
	24	3.8	24	2.4
	27	3.9	24	3.2
80/60 - 0.5%	23	3.2		2.8
Average	**25**	**3.6**	**24**	**2.8**
	24	2.6	18	5.1
	26	2.6	19	4
80/60 - 1.0%	24	2.6		
Average	**25**	**2.6**	**19**	**4.6**

Table 4.2 shows the experimentally obtained and analytically predicted modulus of elasticity, E, and tensile strength, f_t. The average values of the material properties for each concrete mixture are also listed in Table 4.2. It can be seen from this table that, the experimentally obtained and the analytically predicted values are closely matching for the concrete mixtures 65/35-0.5% and 65/35-1.0% but vary significantly in case of the concrete mixtures 80/60-0.5% and 80/60-1.0%. The diameter of the concrete cylinders used to experimentally obtain the elastic modulus, E, and tensile strength, f_t, is 4 in (= 101.2 mm) which is less than even twice the length of the long fibers (2 x 60 mm = 120 mm). A possible reason for the significant difference in the experimental and the predicted results for the 80/60-0.5% and 80/60-1.0% concrete mixtures could be that the specimens used are smaller than the specimens required to avoid the wall effects of the fibers.

Figures 4.17 – 4.20 show the experimentally obtained and analytically predicted *P*-CMOD curves and also the average P-CMOD curve for a CMOD range of [0, 6.0 mm]. The average P-CMOD curves are obtained by predicting the P-CMOD curve using the average σ-w curve parameters shown in Table 4.1.

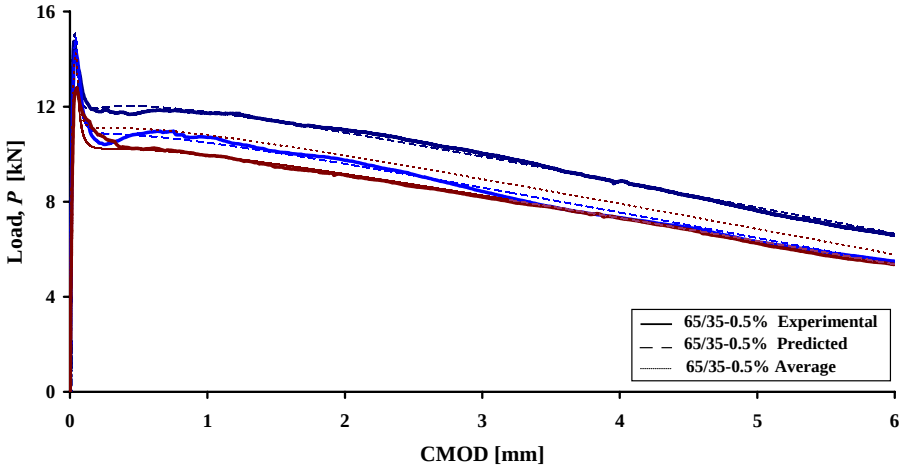

Figure 4.17: Plot showing experimental, predicted and average *P*-CMOD curves for 65/35-0.5% in a CMOD range of [0, 6.0 mm]

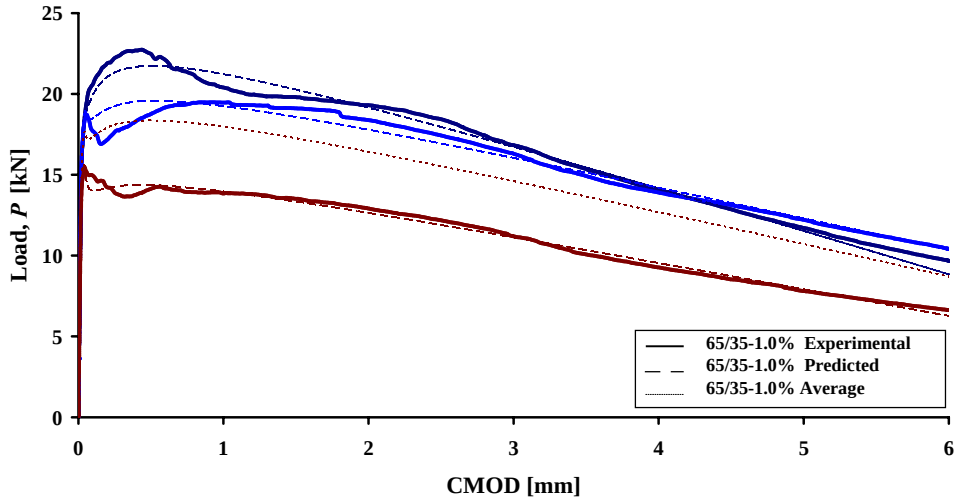

Figure 4.18: Plot showing experimental, predicted and average *P*-CMOD curves for 65/35-1.0% in a CMOD range of [0, 6.0 mm]

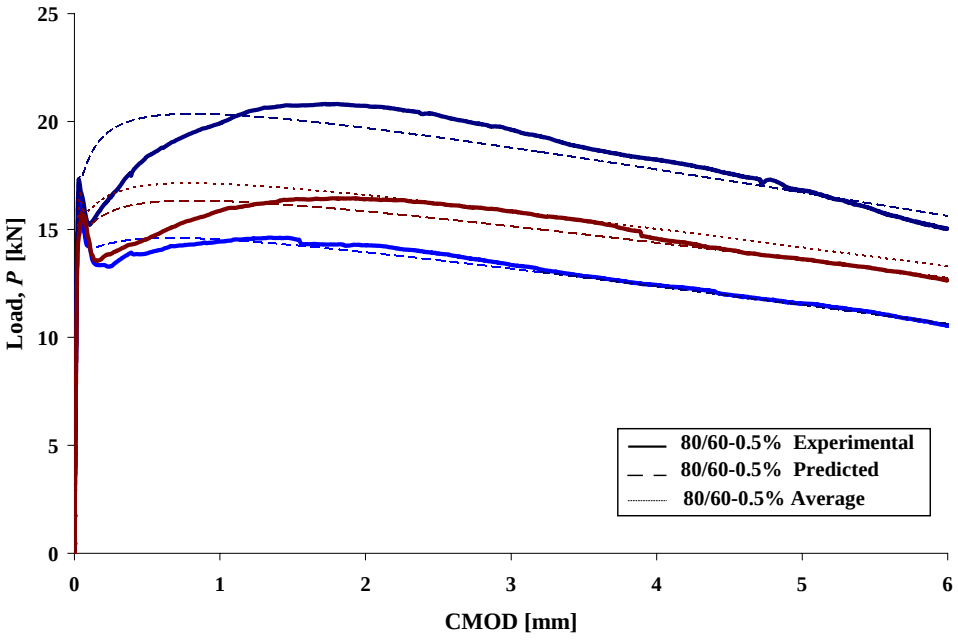

Figure 4.19: Plot showing experimental, predicted and average *P*-CMOD curves for 80/60-0.5% in a CMOD range of [0, 6.0 mm].

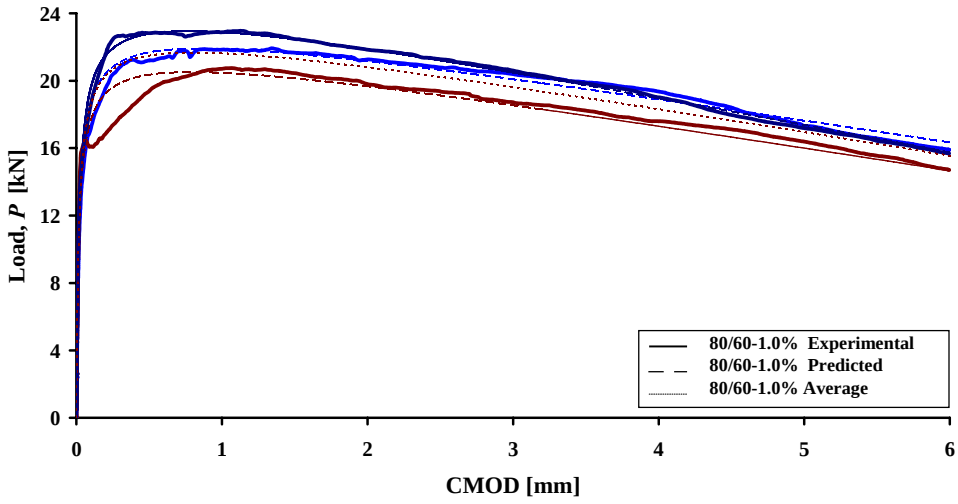

Figure 4.20: Plot showing experimental, predicted and average *P*-CMOD curves for 80/60-1.0% in a CMOD range of [0, 6.0 mm].

Figures 4.17 – 4.20 show a close correlation between the experimental data and the calculated *P*-CMOD curves. The calculated *P*-CMOD curves vary slightly from the experimental data in the region immediately after the first peak. This could be due to the assumption that the $\sigma - w$ curve is a bilinear curve and not a trilinear curve, as assumed by some other researchers (Sousa and Gettu, 2006). However, the overall correlation between the calculated and the experimental data shows that this simplification can be used without compromising the accuracy of the overall behavior.

Chapter 5 Conclusions

The present work focuses on obtaining the fracture properties, σ-w curve, of fiber reinforced concrete, from experimentally obtained P-CMOD curves. An experimental program was carried out to obtain the P-CMOD curves of various types of concrete and a Matlab algorithm was developed to accurately calculate the σ-w curves using inverse analysis procedures. The following conclusions are drawn as part of the present work:

1. There is a high scatter in the residual strengths, $f_{R,i,}$ data compared to the equivalent strength data, $f_{eq,i,}$ which is due to the inherent definition of these terms and the calculation procedure. Therefore, in the analytical formulae proposed by RILEM TC 162-TDF (RILEM, 2001) to model the uniaxial σ-ε behavior of SFRC, the stresses at different strain levels should be expressed as a function of the equivalent strengths rather than the residual strengths. This would lead to a more accurate prediction of the σ-ε behavior .
2. To accurately predict the σ-w curve, the optimization algorithm used to calculate the σ-w curve of concrete should be implemented in three different phases or steps. In the first step (Phase 0), calculate the Modulus of elasticity, E, and tensile strength, f_t, and the slope of the initial phase of the softening curve, a_1, in the second step (Phase I) and the slope of the second phase of the softening curve, a_2, and the initial ordinate, b_2, in the last and third step (Phase II). This three step process leads to an accurate prediction of all the parameters defining the σ-w curve.
3. To calculate the tensile strength, f_t and a_1 in the second step, the CMOD interval should be restricted to 0 – 0.05 mm. Performing the optimization

process on the whole observed CMOD interval would lead to spurious results, since the first phase of the softening curve lies in the interval of 0 – 0.05 mm.

4. RILEM TC 162-TDF (RILEM, 2002a) does not propose any end level of the CMOD for the Bending test of the fiber reinforced concrete specimens. To obtain a $\sigma - w$ curve which can truly depict the complete P – CMOD curve, as proven in this study, the P – CMOD used for the inverse analysis should be captured at least until a CMOD of 5 mm or L/100 is reached. This helps in predicting the correct slope of the second phase of the softening curve, a_2. The calculated value of a_2 varies significantly with the end level of CMOD in the P-CMOD curve until 5 mm.
5. The proposed algorithm does not accurately predict the σ-w curve immediately after the first peak load. However, the modulus of elasticity, E, tensile strength, f_t, are accurately predicted and a good correlation of the experimentally obtained and the analytically predicted load-CMOD curve is observed for a long range of CMOD. This limitation in the prediction of the P-CMOD curve immediately after the first peak could be due to the simplification of the stress-crack opening curve to a bilinear curve as opposed to the more realistic trilinear curve. If the user is interested only in the post peak behavior of the concrete and for a long range of CMOD values, the σ-w curve can be modeled using a drop linear curve instead of using a bilinear curve. This makes the modeling of the σ-w curve simpler by using fewer variables.
6. An interesting observation from the obtained $\sigma - w$ curves is that for concrete mixtures with same volume fraction of fibers, the slopes of the second phase of the softening curve are equal. It would be beneficial to

find the correlation between the slope of the second phase of the softening curve, a_2 and the volume fraction and aspect ratio of fibers. If a_2 can be expressed as a function of the properties of the fibers used, then considering the conclusion that the softening curve can be completely modeled using a drop linear curve using the second phase of the curve, it would be possible to model the softening curve of the concrete analytically. This would avoid the need to perform bending tests on the concrete specimens to capture the *P*-CMOD curves and perform an inverse analysis to obtain the softening curves. Therefore, further research could be done to find the dependency of the parameter a_2 on the volume fraction and aspect ratio of the fibers used.

References

ACI 318, (2008). “Building code requirements for structural concrete and commentary.” *American Concrete Institute*, Reported by ACI Committee 318.

ACI Committee 544, (2002) “State-of-the-Art Report on fiber reinforced concrete.” *American Concrete Institute*, Detroit, MI. 1996 (Reapproved 2002).

Barenblatt, G. I. (1962). “The Mathematical theory of equilibrium cracks in brittle fracture.” *Advances in Applied Mechanics*, Vol. 7, pp. 55 – 129.

Barros, J. A. O., Cunha, V. M. C. F., Ribeiro, A. F., and Antunes, J. A. B. (2005). “Post-cracking behavior of steel fiber reinforced concrete.” *Materials and Structures,* Vol. 38, pp. 47 – 56.

Carpinteri, A., and Ferro, G. (1994). “Size effect on tensile fracture properties – a unified explanation based on disorder and fractality of concrete microstructure. *Materials and Structures,* Vol. 27, pp 563 – 571.

Coronado, C. A. (2006). “Characterization, modeling and size effect of concrete-epoxy interfaces.” *PhD Thesis,* The Pennsylvania State University.

Dugdale, D. S. (1960). “Yielding of steel sheets containing slits.” *Journal of Mechanics and Physics of Solids,* Vol. 8, pp. 100 – 104.

DVB (1995). “Basis for evaluation of steel fiber reinforced concrete for use in industrial floors.” *Deutschen Beton Vereins,* pp. 258 – 272.

Gomez, F. J., Elices, M., and Valiente, A. (2000). “Cracking in PMMA containing U-shaped notches.” *Fatigue and Fracture of Engineering Materials and Structures,* Vol. 29, pp. 795 – 803.

Guo, Z., and Zhang, X. (1987). “Investigation of complete stress-deformation curves for concrete in tension.” *ACI Materials Journal,* Vol. 84, pp. 278 – 285.

Hillerborg, A., Modeer, M., and Petersson, P. E. (1976). "Analysis of crack formation and crack growth in concrete by means of fracture mechanics and finite elements." *Cement and Concrete Research,* Vol. 6, pp. 773 – 782.

Hillerborg, A. (1980). "Analysis of fracture by means of the fictitious crack model particularly for fiber reinforced concrete." *International Journal of Cement Composites,* Vol. 2, pp. 177 – 184.

Hockenberry. T. (2007), "Evaluation of shear capacity of hooked steel fiber reinforced concrete beams with stirrups", *MS Thesis*, The Pennsylvania State University.

Karihaloo, B. L. and Nallathambi, P. (1991). "Notched beam test – Mode I fracture toughness." In Shah, S. and Carpinteri, A., editors, *Fracture Mechanics Test Methods for Concrete,* Chapman and Hall, Chapter I, pp. 1 – 86.

Kitsutaka, Y. (1997), "Fracture parameters by polylinear tension-softening analysis." *Journal of Engineering Mechanics*, Vol. 123, No. 5, pp. 444 - 450.

Lim, D.H. and Oh, B.H. (1999), "Experimental and theoretical investigation on the shear of steel fiber reinforced concrete beams." *Engineering Structures*. Vol. 21, pp. 937-944.

Meda, A., Minelli, F., Plizzari, G.A. and Riva, P. (2005), "Shear behavior of steel fiber reinforced concrete beams." *Materials and Structures*. Vol. 38, pp. 343-351.

Olesen, J. F. (2001). "Fictitious crack propagation in fiber-reinforced concrete beams." *Journal of Engineering Mechanics,* Vol. 127, pp. 272 – 280.

Ostergaard, L. (2003), "Early-age fracture mechanics and cracking of concrete, comparative study of fracture mechanical test methods for concrete." *PhD Thesis*, Technical University of Denmark.

Pedersen, C. (1996). "New production processes, materials and calculation techniques for fiber-reinforced concrete pipes." *PhD Thesis,* Department of Structural Engineering and Materials, Technical University of Denmark, Lyngby, Denmark.

Petersson, P. E. (1981). Report TVBM-1006: "Crack growth and development of fracture zones in plain concrete and similar materials." *Technical Report,* Division of Building Materials, Lund Institute of Technology, Lund, Sweden.

Philips, D. V., and Binsheng, Z. (1993). "Direct tension tests on notched and unnotched plain concrete specimens." *Magazine of Concrete Research,* Vol. 45, pp. 25 – 35.

Planas, J., and Elices, M. (1986). "Towards a measure of G_F: an analysis of experimental results." In Wittmann, F. H., editor, *Fracture Toughness and Fracture Energy of Concrete*. Elsevier, Amsterdam, pp. 381 – 390.

RILEM TC 162-TDF (2001). "Test and design methods for steel fiber reinforced. Recommendations for uni-axial tension test." *Materials and Strucutres,* Vol. 34, pp. 3-6.

RILEM TC 162-TDF (2002a) "Test and design methods for steel fiber reinforced concrete. Bending test – Final Recommendation." *Materials and Structures*, Vol. 35, pp. 579 – 582.

RILEM TC 162-TDF (2002b) "Design of steel fiber reinforced concrete using σ-w method: principles and applications." *Materials and Structures*. Vol. 35, pp 262-278.

Rocco, C., Guinea, G. V., Planas, J. and Elices, M. (1999). "Size effect and boundary conditions in the Brazilian test: Experimental verification." *Materials and Structures,* Vol. 32, No. 3, pp. 210-217.

Roelfstra, P. E., Wittmann, F. G. (1986) “Numerical method to link strain softening with failure of concrete.” *Fracture toughness and fracture energy of concrete*, F. H. Wittmann, ed., Elsevier, Amsterdam, pp. 163-175.

Scanlon, A., Murray, D. W. (1974). “Time dependant reinforced concrete slab deflections.” *Journal of the Structural Division,* Vol. 100, No. 9, pp. 1911-1924.

Slowik, V., Villmann, B., Bretschneider, N., Villmann, T. (2006), “Computational aspects of inverse analysis for determining softening curves of concrete” *Computational Methods in Applied Engineering*, Vol. 195, pp. 7223-7236.

Sousa, J. L. A. O., Gettu, R. (2006), “Determining the tensile stress-crack opening curve of concrete by inverse analysis.” *Journal of Engineering Mechanics*, Vol. 132, No. 2, pp. 141 – 148.

Stang, H. (2000). “Analysis of 3 point bending tests.” Technical Report EU Contract – BRPR – CT98 – 813, *Report from Test and Design Methods for Steel Fiber Reinforced Concrete*.

Stang, H., and Olesen, J. F. (1998). “On the interpretation of bending tests on FRC-materials.” *Fracture Mechanics of Concrete Structures*, Proceedings of FRAMCOS-3, AEDIFICATIO Publishers, D=79104, Freiburg, Germany, pp. 511 – 520.

Stang, H. and Olesen, J. F. (2000). “A fracture mechanics based design approach to FRC.” In Proceedings of *5th International Symposium on Fiber-Reinforced Concretes,* BEFIB 2000.

Tada, H., Paris, P. and Irwin, G. (1985), *The Stress Analysis of Cracks Handbook,* Paris Productions Incorporated, 226 Woodbourne Dr., St. Louis, Missouri, USA.

Timoshenko, S. and Goodier, J. N. (1970). Theory of Elasticity. New York, McGraw-Hill.

Tlemat, H., Pilakoutas, K. and Neocleous, K. (2006). "Stress-strain Characteristic of SFRC using recycled fibers." *Materials and Structures,* Vol. 39, pp. 365 – 377.

Ulfkjaer, J., Krenk, S., and Brincker, R. (1995). "An analytical model for fictitious crack propagation in concrete beams." *Journal of Engineering Mechanics*, Vol. 121, pp. 7-15.

Van Mier, J. G. M. and Vervuurt, A. (1995). "Micromechanical analysis and experimental verification of boundary rotation effects in uniaxial tension tests." In Baker, G. and Karihaloo, B. L., editors, *Fracture of Brittle Disordered Materials*: *Concrete, Rock and Ceramics,* E&FN Spon, London, pp. 406 – 420.

Appendix A – Experimental Data

Load – Deflection Curves.

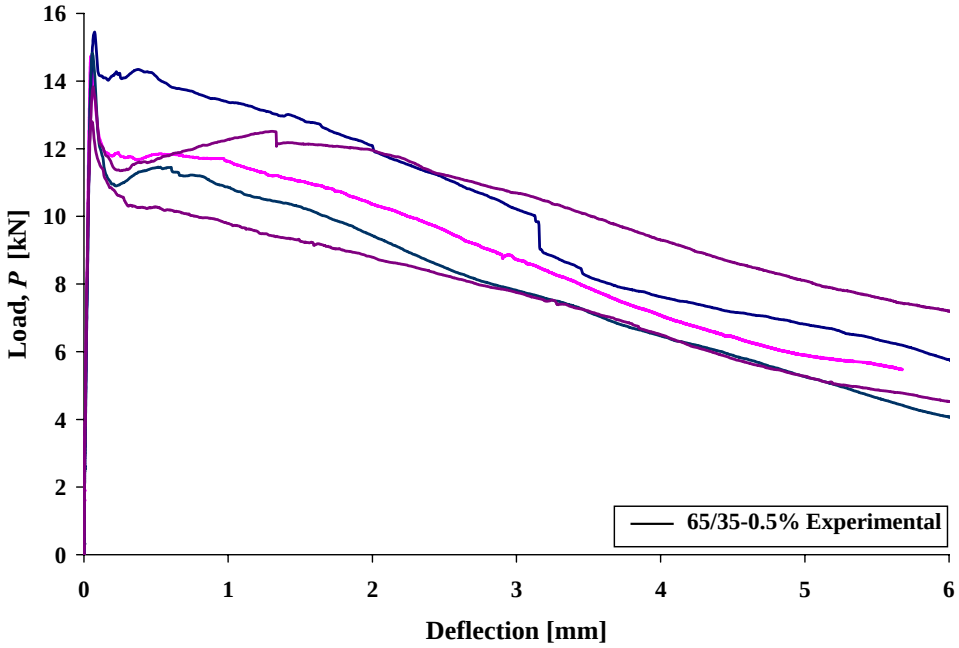

Figure A.1: Plot showing the *P*-δ curves for 65/35-0.5%.

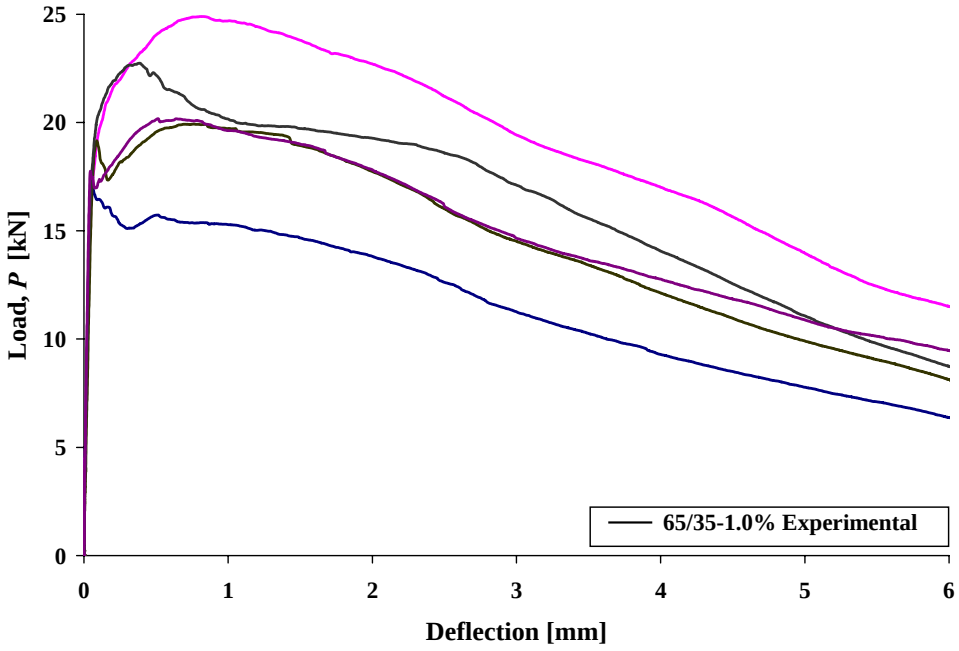

Figure A.2: Plot showing the *P*-δ curves for 65/35-1.0%.

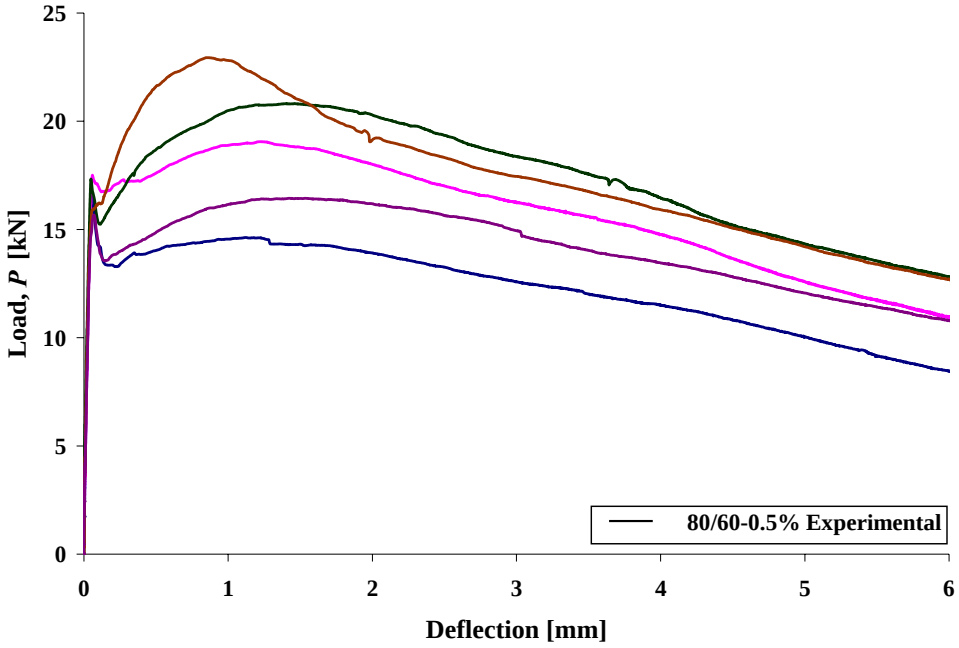

Figure A.3: Plot showing the *P*-δ curves for 80/60-0.5%.

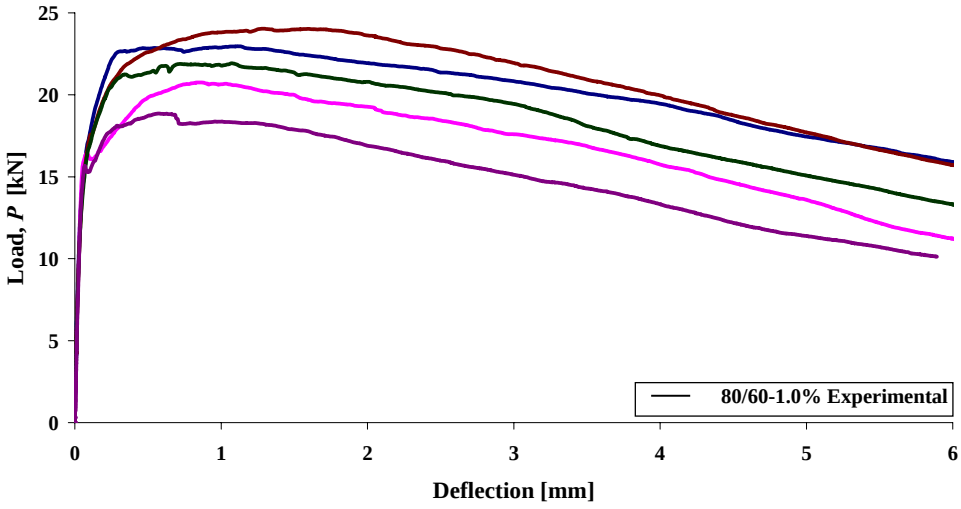

Figure A.4: Plot showing the *P*-δ curves for 80/60-1.0%

Load – CMOD Curves.

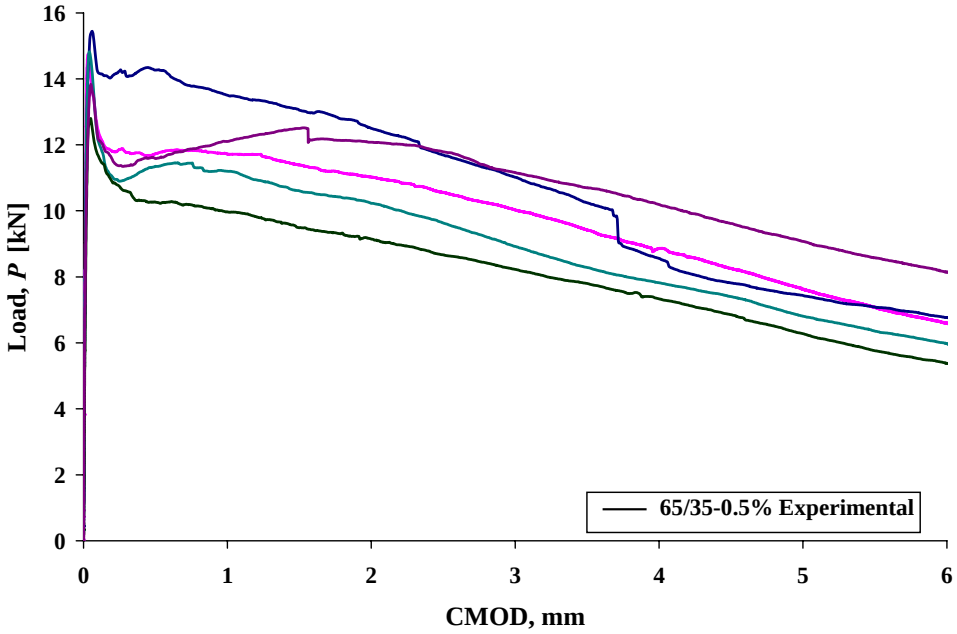

Figure A.5: Plot showing the *P*-CMOD curves for 65/35-0.5%.

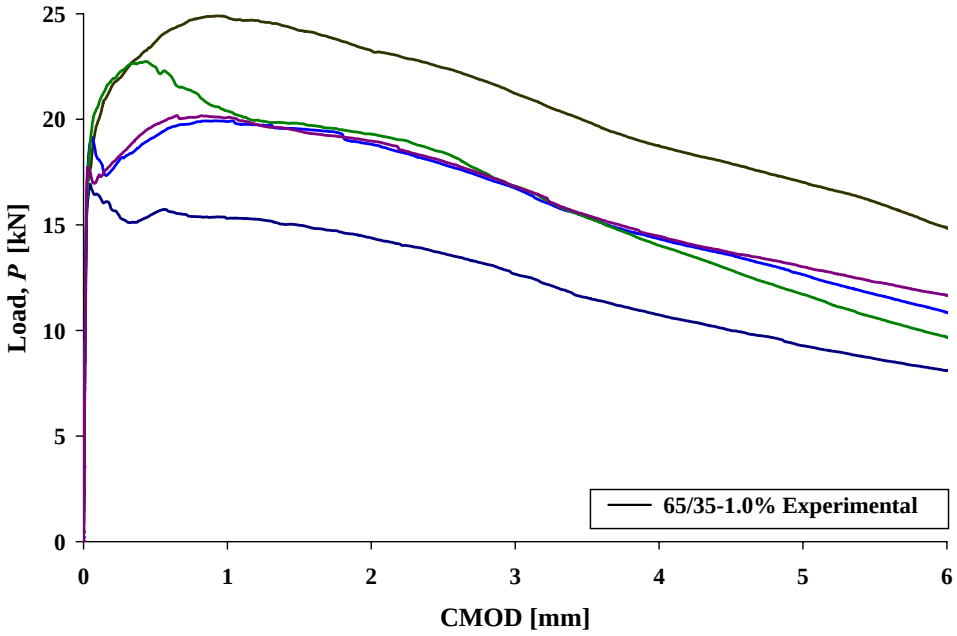

Figure A.6: Plot showing the *P*-CMOD curves for 65/35-1.0%.

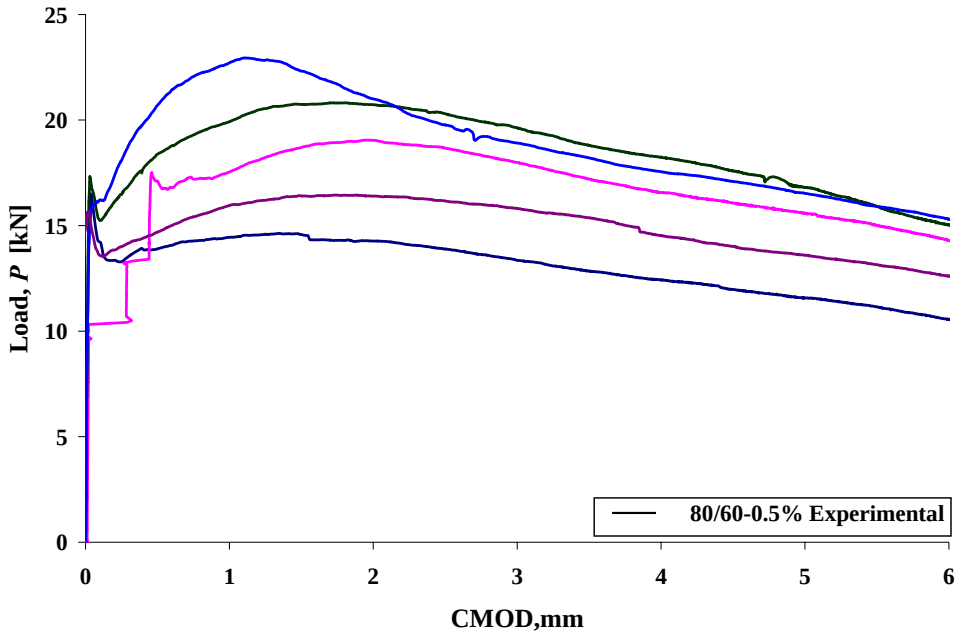

Figure A.7: Plot showing the *P*-CMOD curves for 80/60-0.5%.

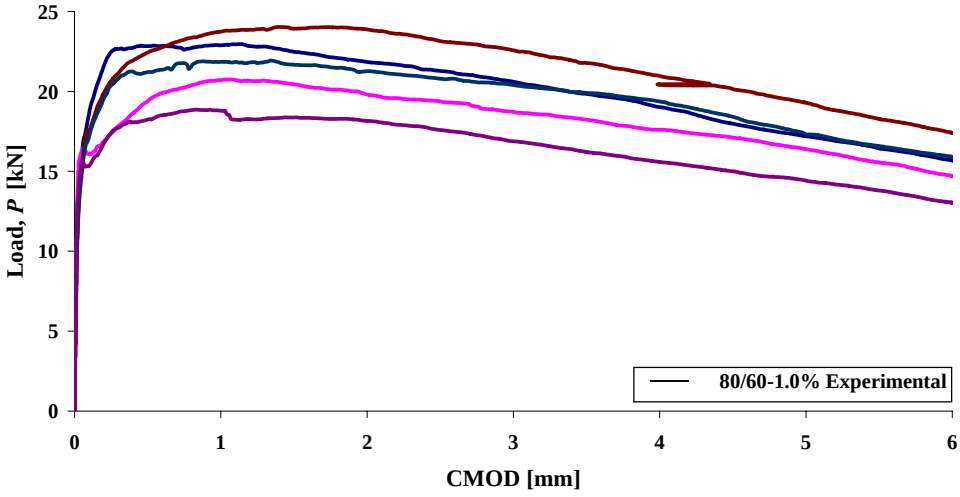

Figure A.8: Plot showing the *P*-CMOD curves for 80/60-1.0%.

CMOD - Deflection curves:

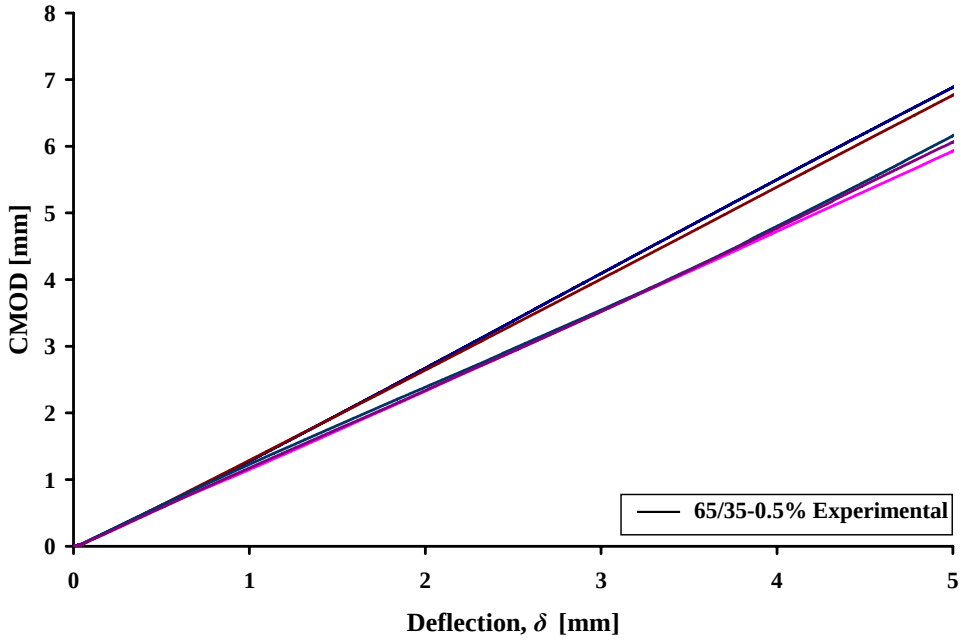

Figure A.9: Plot showing CMOD-δ curves for 65/35-0.5%

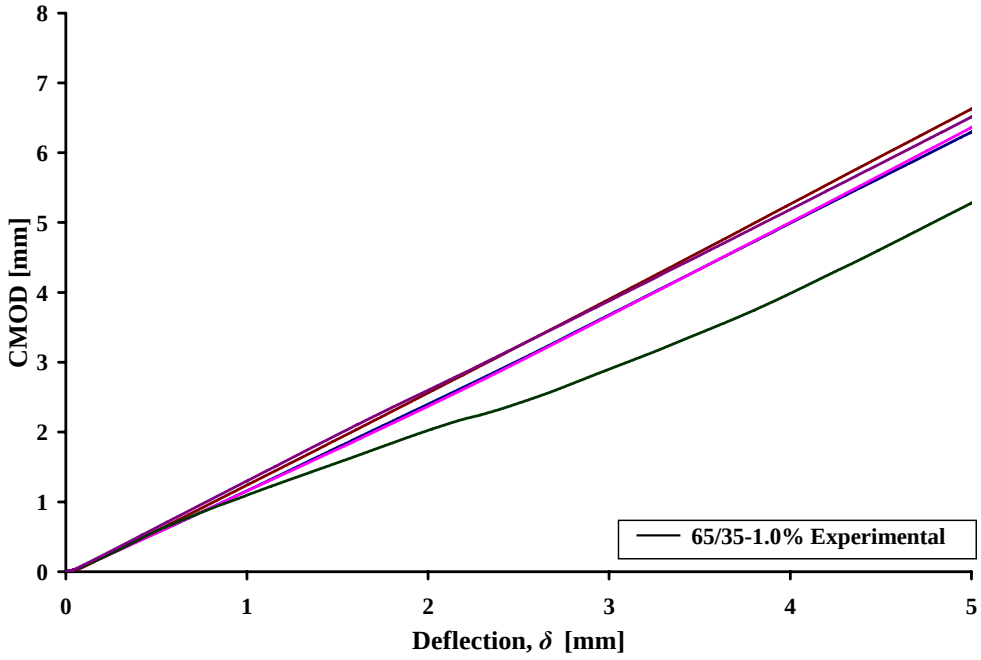

Figure A.10: Plot showing CMOD-δ curves for 65/35-1.0%

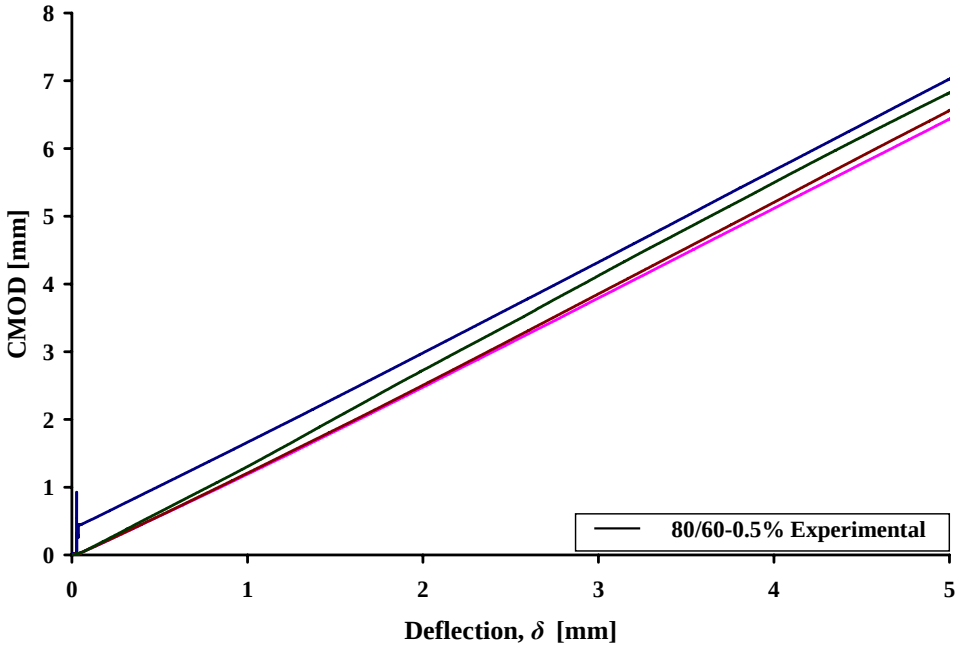

Figure A.11: Plot showing CMOD-δ curves for 80/60-0.5%

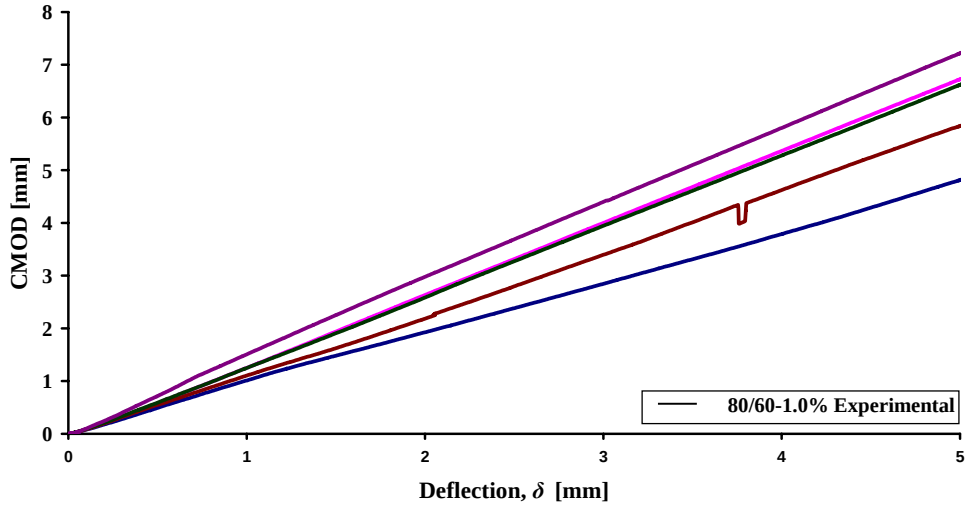

Figure A.12: Plot showing the CMOD-δ curves for 80/60-1.0%

Appendix B – Proposed Matlab Algorithm

Matlab Code for Three Point Bending Test Inverse Analysis.

The following subfunctions are listed:

modulus.m	=	Object Function, Phase 0
getmodulus.m	=	Estimation of Elastic Modulus, Phase 0
objtensile.m	=	Object Function, Phase I
contensile.m	=	Constraints Function, Phase I
gettensile.m	=	Estimation of f_t and a_1, Phase I
objtail.m	=	Object Function, Phase II
contail.m	=	Constraints Function, Phase II
gettail.m	=	Estimation of a_2 and b_2, Phase II

modulus.m

```
function P_anal=modulus(mod,A)
L=500; % Span of the Beam
t=152.4; %Thickness (c/s) of the beam
H=152.4; %Total Height of the beam
a0=25.4; %Notch depth of the beam
h=H-a0; %Unnothced depth or the Ligament depth of the beam
s=h/2;   %Hinge width
d=5;     %Depth of the clipon gage mounts
x=a0/H;
v1=0.76-(2.28*x)+(3.87*x^2)-(2.04*x^3)+(0.66/(1-x)^2); %correction for CMOD
refer Tada(1985)
v2=(5.58-19.57*x+36.82*x^2-34.94*x^3+12.77*x^4)*((x/(1-x))^2);% correction
for Deflection in notched beams refer Tada(1985)
ft=10; %Tensile Strength obtained from Split Cylinder test

for i=1:1000
   theta(i)=(1/999)*(i-1);
   alpha(i)=0;
   mu(i)=theta(i);
   M(i)=mu(i)*ft*h*h*t/6;
   P(i)=(2*ft*h*h*t*mu(i))/(3*L*1000);
   time(i)=i;
   w(i)=0;
   CMODe(i)=6*P(i)*1000*L*a0*v1/(mod*t*H^2);
   deltae(i)=P(i)*1000*(L/H)^2*(L/H+6*v2)/(4*mod*t);
   CMOD(i)=CMODe(i);
   delta(i)=deltae(i);
end
mov_end=1000;
A_avg=moving_average(A(1:mov_end,3),2);
A_new(1,:)=[A_avg;A(mov_end+1:end,3)];
A_new(2,:)=A(:,7);
```

```
Pmax=max(A(:,7));
P_lb=min(find(A(:,7)>2));
P_ub=min(find(A(:,7)>6));
CMOD_int=(A_new(1,P_lb):0.001:A_new(1,P_ub))';
k=fix(((A_new(1,P_ub)-A_new(1,P_lb))/0.001));

CMOD_anal=CMOD_int;
P_anal=zeros(k+1,1);
P_anal(:,1)=interp1q(CMOD',P',CMOD_anal(1:end));
```

getmodulus.m

```
clear
A=xlsread('11_23_1_1%.xls','Signal(raw)');
ft=10;
mov_end=200;
A_avg=moving_average(A(1:mov_end,3),2);
A_new(1,:)=[A_avg;A(mov_end+1:end,3)];
A_new(2,:)=A(:,7);
Pmax=max(A(:,7));
P_lb=min(find(A(:,7)>2));
P_ub=min(find(A(:,7)>6));
CMOD_int=(A_new(1,P_lb):0.001:A_new(1,P_ub))';
k=fix(((A_new(1,P_ub)-A_new(1,P_lb))/0.001));

P_int=zeros(k+1,1);
P_int(:,1)=interp1q((A_new(1,:))',(A_new(2,:))',CMOD_int(1:end));
%P_int(:,1)=P_int1(:,1)-P_int1(1,1);
mod0=25000;
[mod,resnorm]=lsqcurvefit(@modulus,mod0,A,P_int)
```

objtensile.m

```
function obj_tensile = objtensile(tens)
L=500; % Span of the Beam
t=152.4; %Thickness (c/s) of the beam
H=152.4; %Total Height of the beam
a0=25.4; %Notch depth of the beam
h=H-a0;  %Unnothced depth or the Ligament depth of the beam
s=h/2;   %Hinge width
d=5;     %Depth of the clipon gage mounts
x=a0/H;
v1=0.76-(2.28*x)+(3.87*x^2)-(2.04*x^3)+(0.66/(1-x)^2); %correction for CMOD
refer Tada(1985)
v2=(5.58-19.57*x+36.82*x^2-34.94*x^3+12.77*x^4)*((x/(1-x))^2);% correction
for Deflection in notched beams refer Tada(1985) %Tensile Strength obtained
from Split Cylinder test
E=20392; %Modulus of Elasticity obtained using compliance methods

a1=tens(1);ft=tens(2);
b1=1;
beta1=(ft*a1*s)/E;
zeta1=(ft*b1*s)/E;
theta01=1;

for i=1:2500
   if ((i>=1) && (i<=100))
      theta(i)=(1/99)*(i-1);
      alpha(i)=0;
      mu(i)=theta(i);
      M(i)=mu(i)*ft*h*h*t/6;
      P(i)=(2*ft*h*h*t*mu(i))/(3*L*1000);
      time(i)=i;
      w(i)=0;
```

```
        CMODe(i)=6*P(i)*1000*L*a0*v1/(E*t*H^2);
        deltae(i)=P(i)*1000*(L/H)^2*(L/H+6*v2)/(4*E*t);
        CMOD(i)=CMODe(i);
        delta(i)=deltae(i);

    elseif ((i>100) && (i<=2500))
        theta(i)=1+((10-1)/2400)*(i-101);
        alpha(i)=1-beta1-sqrt((1-beta1)*((1/theta(i))-beta1));
        mu(i)=(4*(1-(3*alpha(i))+(3*alpha(i)^2)-((alpha(i)^3)/(1-…
                ….beta1)))*theta(i))+((6*alpha(i))-3);
        w(i)= (s*ft/E)*((1-b1+(2*alpha(i)*theta(i)))/(1-beta1));
        M(i)=mu(i)*ft*h*h*t/6;
        P(i)=(2*ft*h*h*t*mu(i))/(3*L*1000);
        time(i)=i;
        delta(i)=(theta(i)+(((L/(3*s))*((h/H)^3)+(2*(h/s)*((H/h)^2)*v2)-..
                …..1)*mu(i)))*(L*s*ft/(2*h*E));
        CMODe(i)=6*P(i)*1000*L*a0*v1/(E*t*H^2);
        CMODg(i)=2*(a0+d)*s*ft*(theta(i)-1)/(h*E);
        CMODcod(i)=w(i);
        CMOD(i)=CMODe(i)+CMODg(i)+CMODcod(i);
    end
end

A=xlsread('12_05_l_1%.xls','Signal(raw)');
mov_end=1000;
A_avg=moving_average(A(1:mov_end,3),2);
A_new(1,:)=[A_avg;A(mov_end+1:end,3)];
A_new(2,:)=A(:,7);
A_newmax=max(A_new(1,:));
CMOD_exp1=(0:0.001:A_newmax)';
k=fix(A_newmax/0.001);
P_exp1=zeros(k+1,1);
P_exp1(:,1)=interp1q((A_new(1,:))',(A_new(2,:))',CMOD_exp1(1:end));
P1_exp=zeros(k+1,1);
```

```
P1_exp(1:k,1)=P_exp1(2:end,1);
P2_exp=floor(P_exp1-P1_exp);
P1_exp_maxindex=min(find(P2_exp==0));

CMOD_localmax=0.05;
k2=fix(CMOD_localmax/0.001);
CMOD_exp=(0:0.001:CMOD_localmax)';
P_exp=zeros(k2+1,1);
P_exp(:,1)=interp1q((A_new(1,:))',(A_new(2,:))',CMOD_exp(1:end));
CMOD_anal=(0:0.001:CMOD_localmax)';
k1=fix(CMOD_localmax/0.001);
P_anal=zeros(k1+1,1);
P_anal(:,1)=interp1q(CMOD',P',CMOD_anal(1:end));
P_error=P_exp-P_anal;
obj_tensile=norm(P_error);
```

contensile.m

```
function [c,ceq]=contensile(tens)
%Non linear inequality constraints
c=[(tens(1)*tens(2)*63.5/20848)-1]; % 20848 is the Elastic Modulus for a
%particular specimen. Replace it with the Elastic Modulus found in Phase 0
%Non linear equality constraints
ceq=[];
```

gettensile.m

```
clear
A=xlsread('12_05_1_1%.xls','Signal(raw)');
tens0=[10,3]; %starting guess
lb=[0.1,2.0];       %Set lower bounds
ub=[];          %No upper bounds
options=optimset('MaxFunEvals',1000);
tens=fmincon(@objtensile,tens0,[],[],[],[],lb,ub,@contensile,options)
```

objtail.m

```
function obj_tail = objtail(tail)
L=500; % Span of the Beam
t=152.4; %Thickness (c/s) of the beam
H=152.4; %Total Height of the beam
a0=25.4; %Notch depth of the beam
h=H-a0;  %Unnothced depth or the Ligament depth of the beam
s=h/2;   %Hinge width
d=5;     %Depth of the clipon gage mounts
x=a0/H;
v1=0.76-(2.28*x)+(3.87*x^2)-(2.04*x^3)+(0.66/(1-x)^2); %correction for CMOD
refer Tada(1985)
v2=(5.58-19.57*x+36.82*x^2-34.94*x^3+12.77*x^4)*((x/(1-x))^2);% correction
for Deflection in notched beams refer Tada(1985)
ft=2.6473; %Tensile Strength obtained from Split Cylinder test
E=20429; %Modulus of Elasticity obtained using compliance methods

a1=7.3923;a2=tail(1);b2=tail(2);
b1=1;

beta1=(ft*a1*s)/E;
beta2=(ft*a2*s)/E;
zeta1=(ft*b1*s)/E;
zeta2=(ft*b2*s)/E;
c=(1-b2)*(1-beta1)/(beta2-beta1);
theta01=1;
theta12=(round((0.5*(1-c+sqrt(((1-c)^2)+(c^2/(beta1-1)))))*10))/10;
theta23=round(0.5*((b2/beta2)+sqrt((((1-b2)^2)/(beta1-beta2))+(b2/beta2)^2)));

for i=1:1600

   if ((i>=1) && (i<=100))
      theta(i)=(1/99)*(i-1);
```

```
        alpha(i)=0;
        mu(i)=theta(i);
        M(i)=mu(i)*ft*h*h*t/6;
        P(i)=(2*ft*h*h*t*mu(i))/(3*L*1000);
        time(i)=i;
        w(i)=0;
        CMODe(i)=6*P(i)*1000*L*a0*v1/(E*t*H^2);
        deltae(i)=P(i)*1000*(L/H)^2*(L/H+6*v2)/(4*E*t);
        CMOD(i)=CMODe(i);
        delta(i)=deltae(i);

    elseif ((i>100) && (i<=600))
            theta(i)=1+((theta12-1)/600)*(i-101);
            alpha(i)=1-beta1-sqrt((1-beta1)*((1/theta(i))-beta1));
            mu(i)=(4*(1-(3*alpha(i))+(3*alpha(i)^2)-((alpha(i)^3)/(1-
beta1)))*theta(i))+((6*alpha(i))-3);
            w(i)= (s*ft/E)*((1-b1+(2*alpha(i)*theta(i)))/(1-beta1));
            M(i)=mu(i)*ft*h*h*t/6;
            P(i)=(2*ft*h*h*t*mu(i))/(3*L*1000);
            time(i)=i;
            delta(i)=(theta(i)+(((L/(3*s))*((h/H)^3)+(2*(h/s)*((H/h)^2)*v2)-
1)*mu(i)))*(L*s*ft/(2*h*E));
            CMODe(i)=6*P(i)*1000*L*a0*v1/(E*t*H^2);
            CMODg(i)=2*(a0+d)*s*ft*(theta(i)-1)/(h*E);
            CMODcod(i)=w(i);
            CMOD(i)=CMODe(i)+CMODg(i)+CMODcod(i);

    elseif ((i>600) && (i<=1600))

            theta(i)=((theta23-theta12)/(1600-600))*(i-600)+theta12;
            alpha(i)=1-beta2-((1-b2)/(2*theta(i)))-sqrt((1-beta2)*((((1-
b2)^2)/(4*(theta(i)^2)*(beta1-beta2)))-beta2+(b2/theta(i))));
```

```
        mu(i)=(4*(1-(3*alpha(i))+(3*(alpha(i)^2))-((alpha(i)^3)/(1-
beta2)))*theta(i))+((6*alpha(i))-3)-(((1-b2)*((3*(alpha(i)^2))-
((c/(2*theta(i)))^2)))/(1-beta2));
        w(i)= (s*ft/E)*((1-b2+(2*alpha(i)*theta(i)))/(1-beta2));
        M(i)=mu(i)*ft*h*h*t/6;
        P(i)=(2*ft*h*h*t*mu(i))/(3*L*1000);
        time(i)=i;
        delta(i)=(theta(i)+(((L/(3*s))*((h/H)^3)+(2*(h/s)*((H/h)^2)*v2)-
1)*mu(i)))*(L*s*ft/(2*h*E));
        CMODe(i)=6*P(i)*1000*L*a0*v1/(E*t*H^2);
        CMODg(i)=2*(a0+d)*s*ft*(theta(i)-1)/(h*E);
        CMODcod(i)=w(i);
        CMOD(i)=CMODe(i)+CMODg(i)+CMODcod(i);

  % elseif i>1600
   %
    %     theta(i)=;
     %    alpha(i)=1-((1+sqrt((((1-b2)^2)/(beta1-
beta2))+((b2^2)/beta2)))/(2*theta(i)));
      %    mu(i)=(4*(1-(3*alpha(i))+(3*(alpha(i)^2))-
(alpha(i)^3))*theta(i))+((6*alpha(i))-3)-(3*(alpha(i)^2))+(((1-(b2/beta2))*(1-
(b2/beta2)+c)*(1+(beta1*c/(1-beta1))))/(4*(theta(i)^2)))+((c/(2*theta(i)))^2);
       %   w(i)= (s*ft/E)*(1+(2*alpha(i)*theta(i)));
        %  M(i)=mu(i)*ft*h*h*t/6;
         %time(i)=i;
          %delta(i)=(theta(i)+(((L/(3*s))-1)*mu(i)))*(L*s*ft/(2*h*E));


   end
end
A=xlsread('12_05_1_1%.xls','Signal(raw)');
mov_end=200;
A_avg=moving_average(A(1:mov_end,3),2);
A_new(1,:)=[A_avg;A(mov_end+1:end,3)];
A_new(2,:)=A(:,7);
```

```
A_newmax=max(A_new(1,:));
CMOD_exp=(0:0.001:A_newmax)';
k=fix(A_newmax/0.001);
P_exp=zeros(k+1,1);
P_exp(:,1)=interp1q((A_new(1,:))',(A_new(2,:))',CMOD_exp(1:end));
CMOD_anal=(0:0.001:A_newmax)';
P_anal=zeros(k+1,1);
P_anal(:,1)=interp1q(CMOD',P',CMOD_anal(1:end));
P_error=(P_exp-P_anal)^2;
obj_tail=norm(P_error);
```

contail.m

```
function [t,teq]=contail(tail)
%Non linear inequality constraints
ft=2.6473;
a1=7.3923;
E=20429;
s=63.5;
a2=tail(1);
b2=tail(2);
beta1=ft*a1*s/E;
beta2=ft*a2*s/E;
c=(1-b2)*(1-beta1)/(beta2-beta1);
t=1+c-sqrt((1-c)^2+c^2/(beta1-1));
%Non linear equality constraints
teq=[];
```

gettail.m

```
A=xlsread('12_12_1_0.5%_2.xls','Signal(raw)');
tail0=[0.05,0.5]; %starting guess
lb=[0,0];       %Set lower bounds
ub=[];          %No upper bounds
options=optimset('MaxFunEvals',1000);
tail=fmincon(@objtail,tail0,[],[],[],[],lb,ub,@contail,options)
```